Ph.D. Dissertation

Estimation of freshwater discharge into the Northeast Pacific from the Alaskan mountains and its effects on the subtropical and equatorial ventilated thermocline

アラスカ山岳地帯から北東太平洋への淡水流出の推定

および亜熱帯と赤道の通気水温躍層への影響

XIN PENG

Diversion of Earth System Science

Graduate School of Environmental Science

Hokkaido University

February 2025

ABSTRACT

The freshwater discharge from catchments along the Gulf of Alaska, termed Alaska discharge, is characterized by significant quantity and variability. Owing to subarctic climate and mountainous topography, the Alaska discharge variations may deliver possible impacts beyond the local hydrology. While short-term and local discharge estimation has been frequently realized, a longer time span and a discussion on cascading impacts remain unexplored in this area. In the first part of this study, the Alaska discharge during 1982–2022 is estimated using the Soil and Water Assessment Tool (SWAT). The adequate balance between the model complexity and the functional efficiency of SWAT suits the objective well, and discharge simulation is successfully conducted after customization in melting calculations and careful calibrations. During 1982−2022, the Alaska discharge is estimated to be 14,396 ± 819 $m^3 \cdot s^{-1} \cdot yr^{-1}$, with meltwater contributing approximately 53%. Regarding variation in the Alaska discharge, the interannual change is found to be negatively correlated with sea surface salinity (SSS) anomalies in the Alaska Stream, while the decadal change positively correlates with the North Pacific Gyre Oscillation (NPGO), with reasonable time lags. These new findings provide insights into the relationship between local hydrology and regional climate in this area. More importantly, this study provides rare evidence that variation in freshwater discharge may affect properties beyond the local hydrology.

Such freshwater discharge from subpolar lands may influence the ocean circulation of the Pacific. It is known that warm western water from low latitudes is cooled by imposed sea surface temperature (SST) along the northern boundary of the subtropical gyre, and then subducts to the thermocline layers. This subducted water then flows toward the equator, where it upwells, impacting the thermal structure and heat flux in the equatorial region. As a result, these processes play a significant role in shaping biological cycles and atmospheric variability in the tropical Pacific. While wind forcing is the

primary driver for the ocean circulation of the Pacific, other factors, such as the thermohaline processes affected by above-mentioned river discharge as well as the evaporation minus precipitation over the ocean, may also provide crucial influences.

Therefore, in the second part of this study, I focus on investigating whether and how surface freshwater from high-latitudes, especially from the northeast Pacific Ocean, affects the equatorial thermocline. The Massachusetts Institute of Technology General Circulation model (MITgcm) is used to conduct numerical experiments without and with freshwater forcing under various freshwater scenarios. These experiments examine the changes in temperature, salinity, and density distributions, and their effects on the equatorial thermocline. The control experiment, without freshwater, indicates that warm water in the northern subtropical gyre is cooled by heat release from the ocean to the atmosphere and subducts into the subsurface, where it flows along isopycnal surfaces toward the equator and upwells in the eastern equatorial Pacific, contributing to the formation of the cold tongue and an east-west slope in the thermocline. In the freshwater experiments, freshwater fluxes driven by evaporation minus precipitation and boundary freshwater discharge enhance the variability in SSS, with significant freshening in the subpolar gyres. These variations in salinity also affect subsurface thermal structures in the subtropical gyre, and consequently results in warming at depths of 200–400 m in the equatorial Pacific. Especially, in extreme freshwater scenarios, driven by the collapse of the Cordilleran Ice Sheet (CIS) into the northeast Pacific, substantial changes of salinity and temperature are observed in both hemispheres. In the North Pacific, low-salinity water is advected from the subpolar gyre to the subtropical gyre, leading to the advection of cooled water along isopycnal surfaces. This primarily contributes to cooling in the upper layers of the western equatorial Pacific. In contrast, in the South Pacific, the deepening of the thermocline results in relatively higher temperatures and salinities, which contribute to warming in the equatorial thermocline layers. Furthermore, the study reveals that increased freshwater input weakens the east-west SST gradient and deepens the equatorial thermocline, causing an El Nino-like climate. Thus, these findings suggest that freshwater from the subpolar gyre has a potential to significantly affect the equatorial thermocline, which may influence both regional and global climate systems.

Overall, this study presents the reasonable estimation of freshwater discharge from the Alaska drainage basins using a hydrological model and explores the potential relationship between this discharge and atmospheric variability, and its effects on the SSS. Furthermore, with the help of an ocean circulation model, the findings highlight the effects of the freshwater from the subpolar lands on equatorial thermocline and the underlying mechanisms, especially in the case of an extremely large freshwater discharge due to an ice sheet collapse.

Contents

List of figures

List of tables

Chapter 1 General introduction

1.1 Freshwater and its impact on the ocean

Freshwater input into the ocean plays a crucial role in shaping oceanic conditions and influencing large-scale climate systems. This freshwater originates from two primary sources: atmospheric processes, including evaporation and precipitation, and terrestrial sources, primarily river discharge. Each of these contributes to variations in ocean salinity, stratification, and circulation, with significant implications for both regional and global ocean dynamics (Durack, 2015; Lehmann et al., 2022). Evaporation and precipitation are crucial components of the global freshwater cycle. Evaporation from the ocean surface leads to an increasing salinity in regions of excess evaporation, such as subtropical gyres. Conversely, precipitation, particularly in high-latitude and tropical regions, freshens the surface waters and reduces salinity.

In addition to atmospheric processes, river discharge is another major source of freshwater to the ocean, with a global average volume of $36{,}055\ \mathrm{km^3 \cdot yr^{-1}}$ (Syed et al., 2010). Especially in the boundary of subpolar gyre, large rivers and glacial meltwater contribute to substantial volumes of freshwater, which alters salinity and stratification locally and can propagate through ocean currents to affect broader regions (Fujisaki et al., 2014; Shi et al., 2021; Xin et al., 2024).

The atmospheric and terrestrial freshwater flux impacts the density structure of the ocean, influencing its stability and stratification, and consequently, the vertical and horizontal ocean circulation patterns (Fedorov et al., 2004; Seidov et al., 2005; Zhang et al., 2012). In this dissertation, I will discuss the terrestrial hydrological cycle in the Alaskan mountain regions first, which includes the hydrology in vast glacier areas, and detailed estimation of the riverine discharge from this region to the subarctic North Pacific (Chapter 2). I then discuss the impacts of the terrestrial riverine discharge on the ocean circulation of the Pacific Ocean, including extreme cases corresponding to ice sheet collapse events which caused vast freshwater flux from the North American continent to the subarctic North Pacific Ocean (Chapter 3). In the remainder of this chapter, background and motivation of the present research are described.

1.2 Hydrological cycle in the Alaska mountain regions

The hydrological cycle (Fig. 1.1) describes the continuous movement of water between the Earth's surface and the atmosphere. Water moves to the atmosphere as water vapor through evaporation from ocean and lands, as well as transpiration from plants. This vapor condenses and falls back to the Earth's surface as precipitation. Once on the surface, water either flows across land surfaces in basins and channels or infiltrates into underground aquifers. It then travels laterally underground, occasionally resurfacing as springs or flowing through streams at lower elevations. This cycle is driven by solar energy, which powers evaporation, and by gravity, which keeps water in motion throughout the system.

In the mountainous regions of Alaska, the hydrological cycle is further complicated by the interaction of climatic variations and the rugged topography. Significant freshwater discharge into the neighboring oceans is driven by rainfall, snow and ice melt, and minimal human activity in the Alaska region (Beamer et al., 2016; Hill et al., 2015; Wang et al., 2004; Xin et al., 2024).

The Alaska region has a large range of elevation, with an average height of around 1000 m, covered by a number of mountains with some peaks over 3000 m that contribute to the complex topography. The climate in this area is also diverse, due to the high latitude, complex topography, and proximity to the ocean (Bieniek et al., 2012). The higher-latitude region is dominated by cold climates that result in long, cold winters experiencing a polar climate (Beck et al., 2018; Kottek et al., 2006), while the lower-latitude region is characterized by boreal and warm temperate climates, thus leading to relatively mild winters and cool summers (Bieniek et al., 2012; Kottek et al., 2006; Wendler et al., 2016). Therefore, hydrological parameter values are diverse among basins, which should be considered to adequately evaluate the discharge from the Alaskan region. Temporal climate variations are also prominent in this region corresponding to variations of the Aleutian Low such as the Pacific Decadal Oscillation and the North Pacific Oscillation. Thus, a comprehensive estimation of Alaska discharge and its variations can enhance our understanding of the connections among the Alaska discharge, ocean processes in the Pacific, and large-scale atmospheric variations. I discuss this issue in Chapter 2.

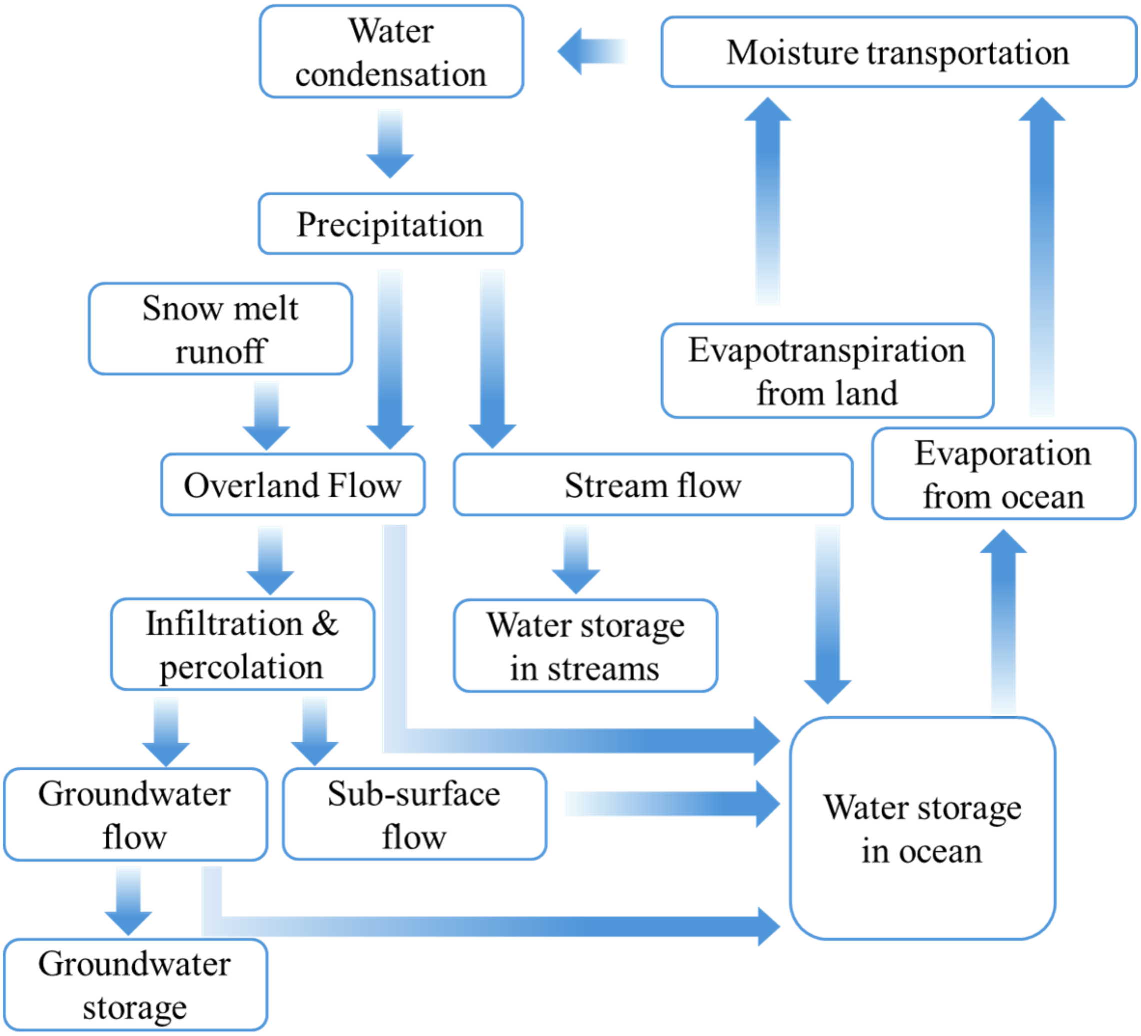

Fig. 1.1 Schematic of hydrology cycle.

1.3 Ocean circulation in the Pacific Ocean

Freshwater discharge from the land impacts salinity along the coastal ocean and potentially influences the ocean circulation. In the Chapter 3 of this dissertation, I will discuss potential impacts of the land water discharge on the ocean circulation further.

The Pacific Ocean is comprised of two primary large-scale gyres in the northern hemisphere that dominate its circulation, including the subtropical gyre and the subpolar gyre. These gyres play crucial roles in heat and freshwater redistribution, nutrient transport, and influencing both regional and global climate patterns (Rae et al., 2020; Ujiié et al., 2016; Zhang et al., 2021). Specifically, the subpolar gyre, situated poleward of 40° latitude, feature counterclockwise circulation in the Northern Hemisphere. Cyclonic winds drive surface divergence and upwelling, which causes western boundary currents to transport cooler, fresher waters equatorward such as the Oyashio Current and the Alaskan Stream. These currents are important in linking high-latitude processes to lower-latitude ocean circulation systems. The subtropical gyres, located between approximately 20° and 40° latitude in both hemispheres, exhibit clockwise circulation in the Northern Hemisphere and counterclockwise circulation in the Southern Hemisphere. These patterns are driven by trade winds along their southern boundaries and westerlies along their northern edges. The convergence of the Ekman transport in the subtropical gyre results in currents such as the Kuroshio and the North Pacific Current.

The subtropical gyre serves as a reservoir for warm and saline water, facilitating poleward heat transport, releasing heat along its poleward boundary. This cooled water then subducts into the thermocline and is advected equatorward; it finally surfaces in the eastern equatorial Pacific, driven by the equatorial trade wind, and gains heat there by forming a cold tongue (Fedorov et al., 2004; Huang and Pedlosky, 2000). This thermal circulation in the ocean forms a climate background that induces the El Niño-Southern Oscillation.

The subpolar gyre receives freshwater from precipitation over the ocean and river discharge from surrounding continents, which can alter the sea surface salinity (SSS) and stratification structures (Fujisaki et al., 2014; Shi et al., 2021; Xin et al., 2024). These causes buoyancy anomalies that can be transported downstream along the coastal boundaries as well as by western boundary currents such as Oyashio. The subpolar water then partially transported to the subtropical gyre via the Ekman transport. I hypothesize that this subpolar freshwater may affect the surface buoyancy of the northern limb of subtropical gyre and control heat release there. This further implies that freshwater from the subpolar gyre may finally impact heat gain on the equatorial cold tongue via the above-mentioned thermal circulation in the Pacific Ocean, through the shallow overturning cells that link the subpolar, subtropical and equatorial gyres (Lu et al., 1998).

In addition to discussing the effects of present riverine discharge on Pacific Ocean circulation, in Chapter 3 I also examine extreme cases of vast freshwater fluxes from the North American continent to the subarctic North Pacific, specifically those caused by the collapse of the Cordilleran Ice Sheet (CIS). The CIS has the largest coverage during the Last Glacial Maximum (approximately 20 thousands years ago), with an average thickness of around 2 km (Walczak et al., 2020). Toward the end of the last glacial period, nearly half of the CIS mass was lost within approximately 500 years, contributing around 3 meters to global sea-level rise (Menounos et al., 2017). Such massive freshwater discharge events are hypothesized to have significantly altered salinity, stratification, and vertical circulation in the subpolar gyre, with cascading impacts on the subtropical and equatorial regions of the Pacific Ocean.

1.4 Objectives of this study

The dynamics of freshwater flux from the mountainous regions of Alaska into the northeast Pacific Ocean are crucial for understanding the mechanisms that regulate ocean circulation and climate variability. Previous studies have provided plausible historical discharge estimates (700–900 km^3 during 1961–2014), however, existing studies estimating this freshwater discharge using hydrological models often overlook the spatial variability of model parameters arising from the complex topography, diverse land cover, soil types, and climatic conditions. A comprehensive exploration of more recent estimations is required to better understand the long-term variations in Alaska discharge and its potential impacts. Therefore, in Chapter 2 of this dissertation, I focus on the estimation of the freshwater discharge from Alaska mountainous catchment at basin scale by using a hydrological model. This approach accounts for spatial variability in model parameters, such as land cover and topography, to improve the accuracy of the discharge estimation. I also investigate the relationship between Alaska discharge and large-scale atmospheric variability, such as the North Pacific Oscillation (NPO). Furthermore, I analyze the impact of Alaska discharge on sea surface salinity (SSS) in the Alaskan Stream, the northern boundary current of the subpolar gyre, to explore its downstream influence on regional ocean dynamics.

Additionally, a connection was found between the subpolar gyre, subtropical gyre and the equatorial region (Lu et al., 1998), however, the effects of freshwater discharge in the subpolar gyre on the equatorial and the related dynamics remain insufficiently explored. Therefore, in Chapter 3, I explore the effects of the freshwater discharge from the Alaska into the northeast Pacific on the equatorial thermocline, especially in the case of an extremely large freshwater discharge due to an ice sheet collapse, with the help of an ocean circulation model.

Chapter 2 Estimation of freshwater discharge into the Northeast Pacific from the Alaskan mountains

2.1 Introduction

River discharge from continents to oceans accounts for a global average of 36,055 $km^3 \cdot yr^{-1}$ (Syed et al., 2010). It plays a non-negligible role in the Earth's hydrological and biogeochemical cycles by delivering freshwater, essential sediments, and nutrients to the ocean (Cloern et al., 1983; Masotti et al., 2018; Wetz et al., 2011). The quantity of and variation in freshwater discharge are the most crucial parameters among many others (Dai et al., 2002; Trenberth et al., 2007). Specifically, freshwater discharge can freshen the seawater and deliver impacts on large-scale ocean processes such as thermohaline circulation (Rahmstorf, 2003). For example, a thermohaline circulation existing in the North Pacific Ocean has been shown to significantly influence the local and global climate and marine ecosystems via the redistribution of heat and the transportation of organic carbon and nutrients (Itoh et al., 2003; Nakatsuka et al., 2004; Nishioka et al., 2013; Whitney et al., 2013). The strength of this circulation process is primarily controlled by the SSS. According to Uehara et al. (2014), anomalies in the SSS may have impacts on the overturning in the northwestern Sea of Okhotsk. These anomalies can propagate along the current pathway from the Alaskan Stream, central Bering Sea, western subarctic gyre, East Kamchatka Current region, and eastern Okhotsk Sea (Fig. A2.1). Following on from this finding, a significant negative correlation was revealed between the interannual variation in SSS in the northwestern Sea of Okhotsk and the variation in annual river discharge from the Kamchatka Peninsula, which is located upstream of the overturning along the current pathways (Shi et al., 2021). Similarly, the role of freshwater discharge from the catchments along the Gulf of Alaska (GOA; hereafter referred to as the Alaska discharge) was hinted at but has not yet been adequately explored. Therefore, the present study aims to investigate the correlation between the Alaska discharge and SSS anomalies in the Alaskan Stream, which is an upstream component of the salt pathway. The significant Alaska discharge into the neighboring oceans is a result of rainfall, snow and ice melting, and little human activity in the Alaskan region. Furthermore, variations in the Alaska discharge exhibit sensitivity to atmospheric phenomena over the North Pacific Ocean and to global climate change (Kunkel et al., 2013; Royer et al., 2001; Wang et al., 2004). However, the long-term variations in the Alaska discharge and their connection with corresponding atmospheric variability remain little known. One potential factor influencing the hydrological processes in the catchments along the GOA is the North Pacific Oscillation (NPO), a large-scale atmospheric variability observed over the North Pacific Ocean. The NPO is characterized by a seesaw north–south dipole of sea level pressure anomalies between the Aleutian Low and North Pacific High (Linkin et al., 2008; Rogers, 1981). Therefore, a comprehensive estimation of the Alaska discharge and its variation can contribute to a better understanding of the connections between regional discharge, large-scale atmospheric variations, and ocean processes in the North Pacific sector.

Various methods can be used to estimate discharge, including the rating curve method, the velocity-area method, hydrological modeling, and remote sensing techniques. Among these options, hydrological models, which include empirical, conceptual, and process-based models, offer an adaptable approach to simulate the processes of water movement under various land cover and soil conditions (Ahmed et al., 2023; Anees et al., 2016; Maxwell et al., 2014). Several studies on the Alaska discharge have primarily focused on estimating the total volume, analyzing the contributions of hydrological components, and examining seasonal variations by using various hydrological models. For instance, Wang et al. (2004) simulated the Alaska discharge and its seasonal and interannual variations by developing a digital elevation model (DEM) that simplifies the main physical processes within the catchment, including rainfall-runoff, snow and ice storage, and melting processes. Neal et al. (2010) estimated the annual Alaska discharge and its contribution from glaciers and icefields using a combination of measured discharge and enhanced precipitation models. Similarly, Hill et al. (2015) developed regression equations to estimate the monthly Alaska discharge at high resolution based on various physical characteristics of the basin, including the area, mean elevation, and land cover, as well as meteorological characteristics such as temperature and precipitation. Moreover, Beamer et al. (2016) estimated the Alaska discharge and examined its source components with good accuracy by using a suite of distributed, process-based models, with consideration of important hydrological processes such as rainfall-runoff, evapotranspiration (ET), infiltration, baseflow runoff, and snow and ice melting.

While these studies confirm that process-based hydrological models provide a comprehensive and efficient representation of real hydrological processes, there are still unresolved questions, particularly regarding the spatial variability of the model parameters. These parameters, which account for different catchment characteristics and climate forcing, are often underrepresented at the basin scale. Additionally, although these studies provide plausible historical discharge estimates (700–900 km^3 during 1961–2014), an extensive exploration of recent estimations is necessary to better understand the long-term variations in the Alaska discharge, given the climatic variation. Furthermore, the influence of the Alaska discharge variations on coastal oceanic systems, such as SSS in the surrounding ocean sector, remains underexplored.

Hence, the present study builds on previous work by focusing on the following: (i) estimating the Alaska discharge during 1982–2022, using a process-based hydrological model, namely, the Soil and Water Assessment Tool (SWAT; Arnold et al., 1998; Neitsch et al., 2011) with modified melting processes, (ii) investigating spatiotemporal variations in the Alaksa discharge, (iii) exploring the correlations between variations in the Alaska discharge and atmospheric phenomena, as well as SSS, to provide a more comprehensive understanding of the atmosphere–land–ocean interactions. Chapter 2 is organized as follows. First, the details of the study area, the SWAT application and its inputs, and the SWAT calibration and validation, as well as the statistical approach for analyzing the discharge, are introduced in Section 2.2. The model calibration, validation, and simulation results are then presented in Section 2.3, along with the connection between the Alaska discharge and atmospheric variability. The relationship between the Alaska discharge and the North Pacific Ocean is discussed in Section 2.4. Finally, the key conclusions are summarized in Section 2.5.

2.2 Data and methods

2.2.1 Study area

The catchments along the GOA (hereafter referred to as the *Alaska catchment*) span the southern region of Alaska and a portion of Canadian territory (54–64° N, 125–157° W), bordering the GOA in the northeast Pacific Ocean (Fig. 2.1a). The present study focuses on the Alaska catchment which covers an area of approximately 320,000 km^2, including five major basins, namely the following: the Susitna (44,391 km^2), Copper (60,451 km^2), Alsek (28,298 km^2), Taku (11,013 km^2), and Stikine (47,734 km^2) basins, in addition to numerous ungauged basins (127,902 km^2). The Alaska catchment has a large range of elevation, with an average height of around 1000 m and some peaks over 3000 m (Fig. 2.1b). The region is covered by a number of mountains that contribute to the complex topography. The major mountain ranges that define the basins include the Coast Mountains in the southeast, the Wrangell-St. Elias Mountains in the east, the Chugach Mountains along the central coast, the Alaska Range stretching from east to west in the northern area, and the Kenai Mountains on the Kenai Peninsula. Particularly, the Wrangell-St. Elias Mountains, above 5000 m, are covered by extensive glaciers. Meanwhile, the Chugach Mountains along the central coast block moist Pacific air, leading to high precipitation on the coastal side and drier conditions inland. The Alaska Range, a long (~1000 km) west–east mountain range, includes the highest peak in North America and is characterized by a tough climate and significant glaciation. Due to the rugged topography, the following 5 slope classes were established across all subbasins in the Alaska catchment: 0–3%, 3–15%, 15–30%, 30–60%, and >60%, based on DEM (NASA/METI/AIST/Japan Spacesystems And U.S./Japan ASTER Science Team) using ArcGIS 10.7.1 software. Most areas (78%) fall within the 3–60% slope range. Additionally, according to North America Land Cover 2015 (Commission for Environmental Cooperation, 2020), the study area consists of various land cover types (Table A2.1), dominated by forest (32.3%), particularly subpolar taiga, polar or subpolar shrubland–lichen–moss (25.5%), barren land (34.1%), glaciers (17.8%), and wetlands (3.48%). The proportions of the main land cover types in the five gauged basins are provided in Table A2.2.

The climate in the study area is diverse, due to the high latitude, complex topography, and proximity to the ocean (Bieniek et al., 2012). The higher-latitude region is dominated by cold climates that result in long, cold winters and brief, cool summers, with the Alaska Range experiencing a polar climate (Beck et al., 2018; Kottek et al., 2006). Meanwhile, the lower-latitude region is characterized by boreal and warm temperate climates, thus leading to humid conditions associated with relatively mild winters and cool summers (Bieniek et al., 2012; Kottek et al., 2006; Wendler et al., 2016). Lader et al. (2016) used reanalysis data from 1979 to 2009 to analyze the near-surface air temperature and precipitation for the Alaska region. Their findings indicated that the average monthly temperature during winter is approximately −12 °C, with an average precipitation of around 6 cm, while the temperatures in the Alaska Range drop below −15 °C and the precipitation exceeds 15 cm. Except for parts of the Alaska Range, summer temperatures in the higher-latitude regions are approximately 10 °C, with precipitation ranging between

10–20 cm. Moreover, the southeastern region is the warmest part of the study area during winter, with average temperatures close to freezing, and a monthly average precipitation of above 20 cm. Although no uniform trend in the annual precipitation is observed across the Alaska catchment, a significant increase in the annual temperature is observed between 1957 and 2021, with a rate of roughly 0.4 °C · $decade^{-1}$ (Ballinger et al., 2023). These variable climate conditions potentially influence hydrological processes across the Alaska catchment.

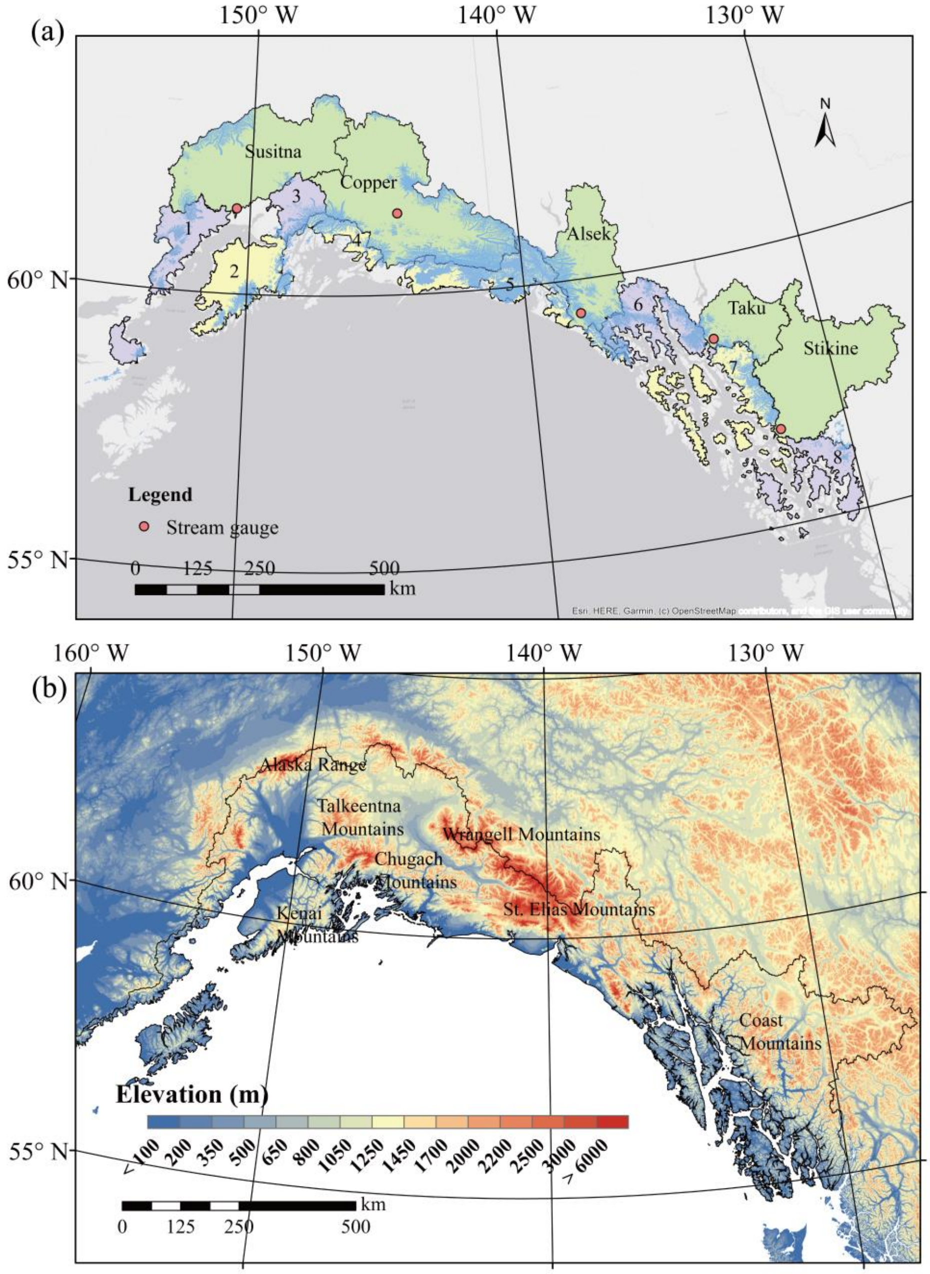

Fig. 2.1 Location and elevation of the Alaska catchment.

(a) The Alaska catchment showing the five basins (green) and ungauged basins (purple and yellow), with glacial coverage (blue), along with the streamflow gauging stations (red points). (b) The topography of the Alaska catchment, as obtained from the ASTER Global DEM Version 3.

These important characteristics such as topography and climate directly influence the Alaska discharge quantity and variability. The discharge is predominantly generated in the mountainous areas that receive substantial snow and rain, with the highest discharge rates observed in low-elevation regions covered by large coastal glaciers (Beamer et al., 2016). Additionally, the phase of precipitation input depends on the air temperature variability, leading to a strong seasonal cycle. The diverse climate of the Alaska catchment, varying from polar in the Alaska Range to temperate in the lower-latitude coastal regions, primarily controls the timing and magnitude of meltwater.

2.2.2 Model setup and configuration

Herein, the SWAT model is used to estimate the discharge during the study period of 1982–2022, as well as the warm-up period during 1979–1981 (methodological flowchart in Fig. 2.2). The SWAT model is a semi-distributed process-based hydrological model that is capable of simulating the water transport in river basins. Specifically, the ArcSWAT 2012 extension (hereafter referred to as *SWAT*) of the ArcGIS 10.7.1-based graphical interface is used in this study to process the discharge simulation. The SWAT model delineates a basin and divides it into a series of subbasins depending on topography. These subbasins are further divided into the smallest unit, namely the hydrological response unit (HRU), based on the homogeneous type of land cover, soil, and slope. The SWAT model then calculates the water balance at the HRU level, aggregates it at the subbasin level, and finally routes it towards the channels and outlet of the basin (Grusson et al., 2015). The water balance is calculated using Equation (Neitsch et al., 2011):

$$SW_t = SW_0 + \sum_{i=1}^{t}\left(R_{day} - Q_{surf} - E_a - W_{seep} - Q_{gw}\right),$$

where SW_t is the final soil water content (mm), SW_0 is the initial soil water content (mm) on day 0, t is time (days), R_{day} is the amount of precipitation (mm) on day i, Q_{surf} is the amount of surface runoff (mm) on day i, E_a is the amount of evapotranspiration (mm) in day i, W_{seep} is the amount of water (mm) entering the vadose zone from the soil profile on day i, and Q_{gw} is the amount of groundwater discharge (mm) on day i.

The main hydrological processes performed in SWAT can be divided into two major phases. The first of these is the land phase of the hydrological cycle, in which the amount of water flowing into the main channel is estimated for each subbasin. The runoff, evapotranspiration, melting processes, and soil–water processes are simulated in this phase. The second division is the channel phase of the hydrological cycle which can be defined as the movement of water through the channel network to the basin outlet (Neitsch et al., 2011). Various methods are used to simulate these processes numerically and to estimate the key components of the catchment water balance. The soil conservation service curve number is an essential method, and is widely used for empirically estimating surface rainfall-runoff (Soil Conservation Service, 1972). This estimation is primarily based on the land cover and soil type of catchment. The SWAT model is capable of estimating the runoff from frozen soil if the temperature in the first soil layer is less than 0 °C (Neitsch et al., 2011). The constant land cover and soil types were used in the present study due to their minimal variation over time (see Section 2.3 for more details). Meanwhile, the Penman–Monteith method (Allen et al., 1989; Monteith, 1965) is satisfactory for estimating potential evapotranspiration by considering various climate parameters such as temperature, humidity, wind speed, and solar radiation. The kinematic storage method (Sloan et al., 1983) is used to estimate lateral flow in soil layers, accounting for the variations in conductivity, slope, and soil water content of the catchment. Additionally, the variable storage routing method (Jimmy R. Williams, 1969) is used to estimate the movement of water through the channel network by considering channel characteristics such as width, length, and slope within the catchment. Therefore, the selection of SWAT as the foundational model is underpinned by its notable attributes:

its complicated preprocessing is made relatively accessible through ArcGIS 10.7.1 software add-ins and its computation is relatively efficient owing to the semi-distributed structure with fewer repetitive routines. Moreover, the existing literature has verified that SWAT performs well in reproducing the hydrological processes in mountainous and glacierized basins (Grusson et al., 2015; Omani et al., 2017a).

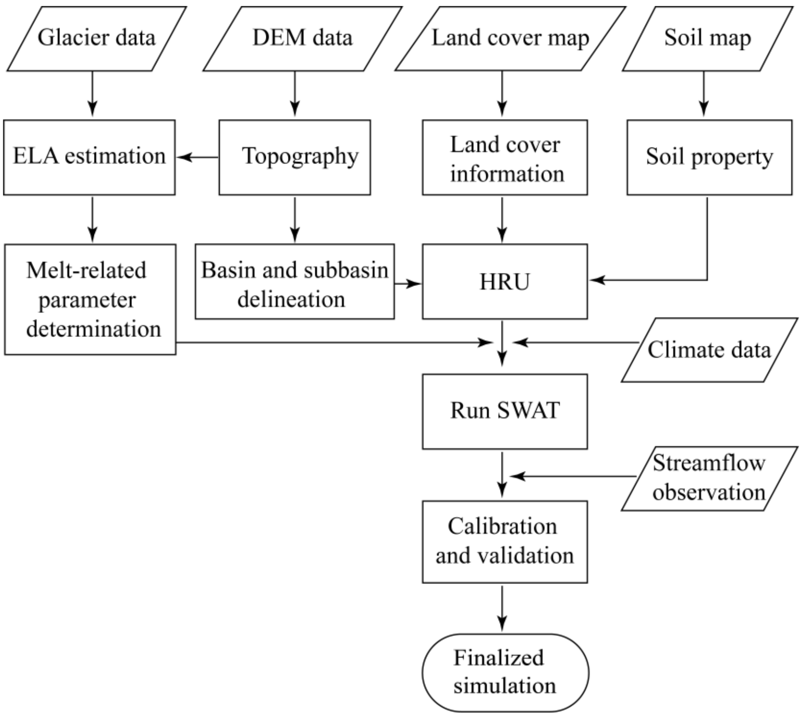

Fig. 2.2 Methodological flowchart for SWAT.

The snowfall and melting processes are important components of the hydrological cycle in the present study, since the Alaska catchment is partially covered by snow and ice. The SWAT model distinguishes between rainfall and snowfall based on a comparison of the near-surface air temperature and the threshold snowfall temperature (SFTMP). Snowfall occurs when the mean daily air temperature is lower than the SFTMP, and snow can accumulate until melting occurs. Melting begins when the air temperature is higher than the threshold snowmelt temperature (SMTMP). The SWAT model allows for spatial variations in precipitation and temperature by accounting for changes in elevation at the subbasin level. A maximum of ten elevation bands can be defined in SWAT. In each elevation band, the precipitation and temperature are modified based on two lapse rates, namely the temperature lapse (TLAPS) and precipitation lapse (PLAPS). Given that the elevation of glacierized areas in the Alaska catchment is mostly above 2000 m, ten elevation bands were established in the present study.

In the default setting of SWAT, melting calculations are based on a simplistic temperature-index method that does not account for ice melting. This is potentially problematic, given the considerable contribution of meltwater from glacierized areas. Therefore, the melting process in glacierized areas is additionally modified by separate calculations based on the equilibrium-line altitude (ELA). The ELA is a theoretical line where the annual mass balance is zero and represents the boundary between the accumulation and ablation zones of a glacier. In this study, the ELA was initially estimated by using the accumulation area ratio (AAR), which is the ratio between a glacier's accumulation zone and its total area (Cogley et al., 2011). More specifically, based on the available AAR observational data (Mernild et al., 2013) for glaciers in the Alaska catchment, the average AAR value was estimated to be 0.62. The glaciers in each basin were treated as a group, rather than as individual glaciers. Next, the elevation data for the glaciers were used, along with their outlines from the Randolph Glacier Inventory (RGI) 6.0 dataset, to conduct the ELA calculations of the glaciers within the five basins. As the glacial volume loss makes a relatively low contribution (6–10%) to the discharge (Beamer et al., 2016; Hill et al., 2015; Neal et al., 2010), the glacierized areas are treated as constant during the estimation. The ELAs were therefore estimated as 1378, 1602, 1287, 1331, and 1542 m for glaciers in the Susitna, Copper, Alsek, Taku, and Stikine basins, respectively. The average ELA for the five basins was 1428 m, which is consistent with the available observed mean ELA for Alaska glaciers (1363 ± 103 m) during 1982–2020 (Ohmura et al., 2022). Finally, the estimated ELA in each basin was applied to divide the elevation bands into accumulation and ablation zones within the glacierized subbasins. The lowest elevation band of the ablation zone corresponds to the location where 90% of the glaciers' coverage is reached.

Separate melt factors were established for the ablation and accumulation zones to determine the spatially distinct melting processes, based on the methods described by Omani et al. (2017a). The parameters used to estimate the snowfall, snow accumulation, and melting processes at the subbasin level were given fixed values and were well constrained by previous research and physical interpretations (Andrianaki et al., 2019; Omani et al., 2017a, 2017b). Thus, for the non-glacier zone, the SFTMP and SMTMP were each set as 0 °C, the maximum snowmelt factor (SMFMX) on 21 June was set as 5 $mm \cdot H_2O \cdot °C^{-1} \cdot day^{-1}$, the minimum snowmelt factor (SMFMN) on December 21 was set as 3 $mm \cdot H_2O \cdot °C^{-1} \cdot day^{-1}$, and the snowpack temperature lag factor (TIMP) was set as 1. For the ablation zone, the SFTMP, SMTMP, SMFMX, SMFMN, and TIMP were 1 °C, 0.5 °C, 6 $mm \cdot H_2O \cdot °C^{-1} \cdot day^{-1}$, 3 $mm \cdot H_2O \cdot °C^{-1} \cdot day^{-1}$, and 0.05, respectively. For the accumulation zone, the corresponding values were 2 °C, 2 °C, 7 $mm \cdot H_2O \cdot °C^{-1} \cdot day^{-1}$, 4 $mm \cdot H_2O \cdot °C^{-1} \cdot day^{-1}$, and 0.01, respectively. Seasonal snow melt and summer ice melt mainly occur in the ablation zone, while permanent snow and ice undergo accumulation and melting in the accumulation zone. The initial glacier depth was set at 15,300 mm by averaging the thickness of the observed glaciers (RGI 6.0) within the Alaska catchment. Overall, while this approach does not fully capture the complexities of melting processes, such as the glacial dynamics and behavior of individual glaciers, it effectively accounts for the major accumulation and melting processes driven by temperature, considering spatial variability and using reasonable melting-related parameters based on the existing literature (Grusson et al., 2015; Omani et al., 2017a, 2017b). Despite its simplicity, the

SWAT model in combination with the temperature-index approach is suitable for melting calculations.

2.2.3 Model inputs

The model input data are listed in Table 2.1. The 30 m resolution DEM data, obtained from ASTER Global Digital Elevation Model version 3, were used in SWAT to delineate basins and subbasins, and to compute the flow directions of the river system. Land cover data with a resolution of 30 m were obtained from the North America Land Cover 2015. The Alaska catchment area was divided into 9 land cover types. The Food and Agriculture Organization Digital Soil Map of the World (FAO-UNESCO Soil Map of the World 1:5000000, 1974), with a scale of 1:5,000,000, was used to classify the 18 soil types that could be directly used in the SWAT soil database.

The land cover and soil inputs for SWAT were regarded as constant throughout the simulation, which could lead to uncertainties. However, no evidence that significantly contradicts the consideration of constant land cover and soil inputs was found in previous studies. More specifically, regarding the land cover distribution, most forested areas and other land cover types such as pasture, rangeland, built-up land, and cropland, did not undergo significant changes in northwestern North America, including in the Alaska catchment, during 1960–2020 (Biswas et al., 2012; Potapov et al., 2022; Winkler et al., 2021). Regarding the change in soil distribution, the process is more commonly long-term, while extreme and significant change can be brought about by short-term processes primarily associated with human activities. However, such short-term changes were found to be less evident in the Alaska catchment (Montanarella et al., 2015).

The meteorological data including daily precipitation (mm), maximum and minimum temperature (°C), solar radiation ($MJ \cdot m^{-2}$), relative humidity (%), and wind speed ($m \cdot s^{-1}$), were used to force the hydrological processes in the SWAT simulation. Notably, the meteorological data were obtained from two separate datasets, namely the climate forecast system reanalysis (CFSR, 1979–2013; Saha et al., 2010) and the climate forecast system version 2 operational data (CFSv2, 2011–2022; Saha et al., 2014). Nevertheless, the CFSv2 can be considered as an extension of the CFSR, which has been successfully applied to simulate the hydrological processes in North America (Beamer et al., 2016; Saha et al., 2014, 2010). Therefore, the dual datasets were used to force the discharge simulation in this study.

Table 2.1. The input data used in the SWAT model.

Data	Description	Spatiotemporal Resolution
DEM	ASTER Global Digital Elevation Model version 3	30 m grid
LC	North America Land Cover 2015	30 m grid
Soil	FAO Digital Soil Map of the World	1:5 000 000
Climate	Climate Forecast System Reanalysis (CFSR, 1979–2013); Climate Forecast System version 2 operational data (CFSv2, 2011–2022)	0.31° × 0.31° grid/daily; 0.5° × 0.5° grid/daily

2.2.4 Model calibration and validation

In this study, the SWAT Calibration and Uncertainty Program (SWAT-CUP) was used to calibrate the model parameters (Abbaspour et al., 2007). SWAT-CUP is an interface that applies the Sequential Uncertainty Fitting (SUFI-2) algorithm to determine the parameter values and their uncertainties via sequential and fitting processes (Abbaspour et al., 2007). Although many parameters influence the discharge estimation in SWAT, the availability of adequate parameter values based on observation is limited. To avoid excessive tuning, fewer parameters should be considered, with more attention being paid to the features that they represent (Shi et al., 2023). Therefore, the present study mainly focuses on the most influential parameters based on previous studies that used SWAT to estimate the discharge in snow and glacierized basins (Fontaine et al., 2002; Grusson et al., 2015; Neupane et al., 2017; Omani et al., 2017a). These parameters account for the primary hydrological processes within the study area, including the surface runoff, evapotranspiration, and groundwater flow processes, thereby ensuring the efficiency and accuracy of the model calibration. The calibrated parameters included the curve number (CN2), which is a key parameter for estimating surface runoff, as it directly influences the quantity of precipitation that becomes runoff. The available water capacity of the soil layer (SOL_AWC, $mm \cdot H_2O \cdot mm\ soil^{-1}$) and the soil evaporation compensation (ESCO) are crucial to soil moisture and evaporation processes. The minimum snow water content that corresponds to 100% snow cover (SNOCOVMX, $mm \cdot H_2O$) influences the areal depletion of snowpack coverage, which is essential for representing snowmelt timing and runoff volume. The threshold depth of water in the shallow aquifer required for return flow to occur (GWQMN, $mm \cdot H_2O$), the groundwater delay time (GW_DELAY, days), and the baseflow alpha factor (ALPHA_BF) play an important role in routing meltwater through the subsurface, affecting the hydrological response of the watershed. The TLAPS ($°C \cdot km^{-1}$,) and the PLAPS ($mm \cdot H_2O \cdot km^{-1}$) control the spatiotemporal distribution of precipitation, determining whether it falls as rain or snow. The model performance was evaluated by statistical metrics such as the Nash–Sutcliffe efficiency (NSE), the coefficient of determination (r^2), and the percentage bias (PBIAS). The model result was considered acceptable when the critical threshold for each index was satisfied, i.e., $NSE >$ 0.50, $r^2 > 0.70$, and $|PBIAS| < 25\%$ (Moriasi et al., 2007). Positive values of *PBIAS* indicate an underestimation bias in the model, while negative values indicate an overestimation bias. More detailed information on SWAT can be found in the official document (Arnold et al., 2012).

In the present study, the model calibration and validation were performed using limited monthly observed streamflow data from the outlets of the five basins. The observed data were obtained from the Global Runoff Data Centre (https://www.bafg.de/GRDC/). The streamflow gauging positions are shown in Fig. 2.1a, and the specific details are presented in Table A2.3. For the Susitna basin, the streamflow observations for 1982–1988 were used for calibration, and those for 1989–1992 were used for validation. For the Copper basin, the calibration period was 1982–1985 and the validation period was 1986–1990.9. For the Alsek basin, the calibration period was 1991.7–1997 and the validation period was 1998–2012.11. For the Taku basin, the calibration period was 1987.8–1997 and the validation period was 1998–2008. For the Stikine basin, the calibration period was 1982–1997 and the validation period was 1998–2005. The model configurations including the setup of elevation bands and the calibrated parameters in each of the five basins were subsequently projected to their adjacent ungauged basins for further discharge estimation, according to the principle of spatial proximity and hydrological similarity (Bárdossy, 2007; Mengistu et al., 2019). Specifically, the setup of the elevation bands and the calibrated parameters in the Susitna basin were projected to its neighboring basins, namely, ungauged basins No. 1, 2, and 3 (Fig. 2.1a). Similarly, the setup from the Copper basin was applied to ungauged basin No. 4, those from the Alsek basin to ungauged basins No. 5 and 6, and those from the Stikine basin to ungauged basins No. 7 and 8.

The results of model calibration and validation are presented in Section 2.3.1. The estimated Alaska discharge is then discussed as a whole in Section 2.3.2, and for each of the five basins and the ungauged basins in Section 2.3.3. Here, the discharge characteristics for each of the five individual basins are discussed to provide a better understanding of regional heterogeneity. Additionally, the integrated discharge from the ungauged basins is discussed and compared with that from the five gauged basins.

2.2.5 Statistical analysis

Herein, the trend in the Alaska discharge was assessed by using the non-parametric Mann–Kendall Test and Sen's slope estimator. The Mann–Kendall Test is widely used to detect significant trends in time series datasets (Kendall, 1948; Mann, 1945). The Z-score (Zs), also known as the standard score, measures how many standard deviations a data point is from the mean of a dataset. A trend exists when the statistical values satisfy $p < 0.05$ and $|Zs| > 1.96$. A positive Zs value indicates an increasing trend, while a negative Zs indicates a decreasing trend. The Sen's slope estimator determines the slope of the trend, thereby indicating the rate of change (Sen, 1968). Furthermore, the relationship between the long-term variations (5-year running means) in the Alaska discharge and the North Pacific Gyre Oscillation (NPGO) index (Di Lorenzo et al., 2008; i.e., the time series of the NPGO) is determined. The NPGO is suggested to be driven by sea surface wind variability associated with the NPO, which is an atmospheric variability characterized by a seesaw north–south dipole between the Aleutian Low and the North Pacific High. Therefore, the NPGO index is referred to as the oceanic expression of the NPO (Di Lorenzo et al., 2008), and is used to reveal the connection between variations in the Alaska discharge and the NPO. Moreover, the annual Alaska discharge is compared with the SSS anomalies for 1984–2008 in the Alaskan Stream, as reported by Uehara et al. (2014), to investigate the effects of the Alaska discharge on the oceanic characteristics in the North Pacific sector.

2.3 Results

2.3.1 Model calibration and validation

The default values for the selected parameters, the methods of adjustment used, and the final calibrated values over each basin are presented in Table 2.2. The parameters CN2 and SOL_AWC were adjusted by relative tests wherein the parameter value was multiplied by 1 + the given value in the table, as indicated by r in the parameter designation. The other parameters were modified by replacement tests wherein the parameter value was replaced by the given value, as indicated by v in the parameter designation. The calibrated parameters are within reasonable ranges. Among the calibrated parameters, ALPHA_BF is the most sensitive across the five basins (Fig. A2.2). The model's performance varies significantly when ALPHA_BF, baseflow alpha factor, is adjusted within the range of −0.1–0.03, whereas the model tends to stabilize and deliver satisfactory performance when its value exceeds 0.03 (Fig. A2.3). The calibration and validation performance indices for each basin are given in Table 2.3, which indicates that *NSE* values are greater than 0.5, r^2 values are greater than 0.7, and *PBIAS* values are within ± 25%. These results statistically demonstrate an acceptable model performance. Indeed, the simulated discharge hydrograph in Fig. 3a and b agrees well with observations during both the calibration and validation periods, especially in the Alsek, Taku, and Stikine basins, which have relatively longer observational datasets than the Susitna and Copper basins. However, the results indicate that the SWAT model underestimates the discharge from the Susitna, Copper, Alsek, and Taku basins, while it overestimates the Stikine basin, especially in summer (Fig. 2.3 and Table 2.3). This can be primarily attributed to uncertainties in the meltwater estimation related to the catchment characteristics, particularly the topography. Compared to the other basins, the elevation bands of the Stikine basin are predominantly distributed at higher altitudes. Although the use of elevation bands in SWAT is acceptable for estimating snow-related processes and improving hydrological performance, it tends to slightly overestimate the snow accumulation and subsequent snowmelt in high-elevation regions and underestimate them in low-elevation regions, due to uncertainties arising from the linear variation in the temperature and precipitation lapse rates (Grusson et al., 2015). Moreover, the Susitna and Copper basins largely encompass areas with slopes of less than 15% (56% and 52%

of the basin area, respectively). This relatively gentle slope may introduce uncertainties in the hydrological processes by reducing the surface runoff and increasing the soil water storage and evaporation during the simulated summer season. Despite several discrepancies in the hydrograph, the calibrated model is satisfactory for representing the discharge processes, and is therefore considered to be capable of estimating the discharge from the five basins.

Table 2.2. The SWAT parameters and their values used for calibration.

Parameter [a]	**Range**	**Default Value**	**Calibrated Value**				
			Susitna	**Copper**	**Alsek**	**Taku**	**Stikine**
r_CN2	35–98	36–92 [b]	–0.19	–0.22	–0.29	–0.24	–0.18
r_SOL_AWC	0–1	0–0.175 [b]	–0.56	–0.53	–0.46	–0.46	–0.07
v_ESCO	0.01–1	0.95	0.06	0.48	0.77	0.69	0.37
v_SNOCOVMX	0–500	1	125.64	424.85	354.08	437.4	299.7
v_GWQMN	0–5000	1000	255.90	1450.01	1310.40	969.01	1257
v_GW_DELAY	0–500	31	26.60	34.87	49.23	34.94	25.86
v_ALPHA_BF	0–1	0.048	0.03	0.048	0.097	0.08	0.04
v_TLAPS	–10–10	–6.5	–4.73	–7.34	–5.82	–6.02	–7.64
v_PLAPS	–1000–1000	200	500	105.09	500	215.52	392.5

[a] Here: r represents a relative test where the parameter value is multiplied by 1+ the given value and v represents a replacement test where the parameter value is replaced by the given value. [b] Values determined by soil and land cover types in each HRU.

Table 2.3. The statistical results of the model performance.

Basin	**Calibration**			**Validation**		
	NSE	r^2	***PBIAS*** **(%)**	***NSE***	r^2	***PBIAS*** **(%)**
Susitna	0.855	0.905	17.13	0.846	0.901	16.80
Copper	0.812	0.816	7.20	0.805	0.808	5.60
Alsek	0.787	0.841	21.40	0.845	0.877	16.10
Taku	0.827	0.869	13.46	0.872	0.879	5.45
Stikine	0.825	0.866	−10.76	0.848	0.927	−14.69

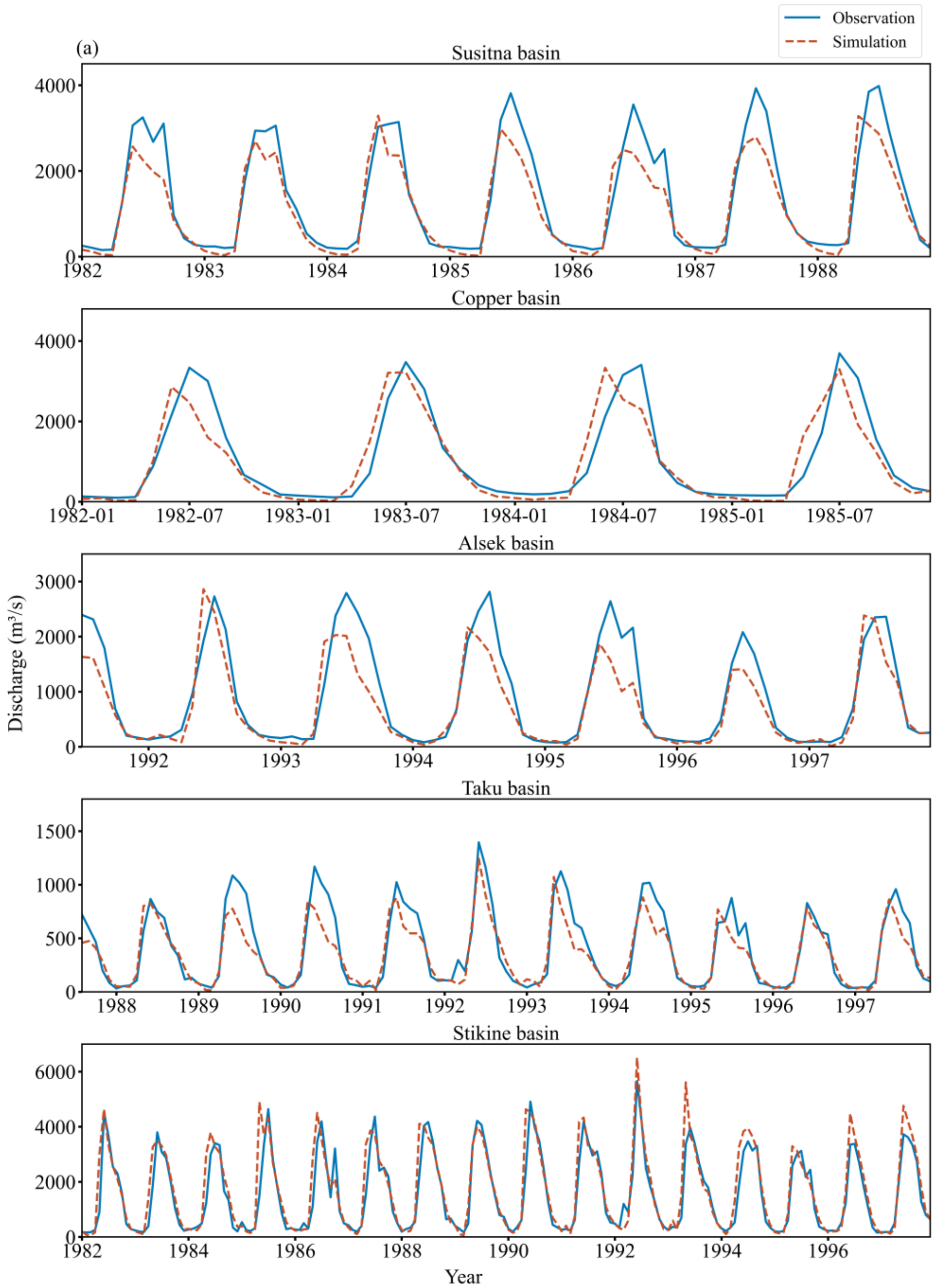

Observation
Simulation
(a)
Susitna basin
Copper basin
Alsek basin
Taku basin
Stikine basin
Discharge (m³/s)
Year

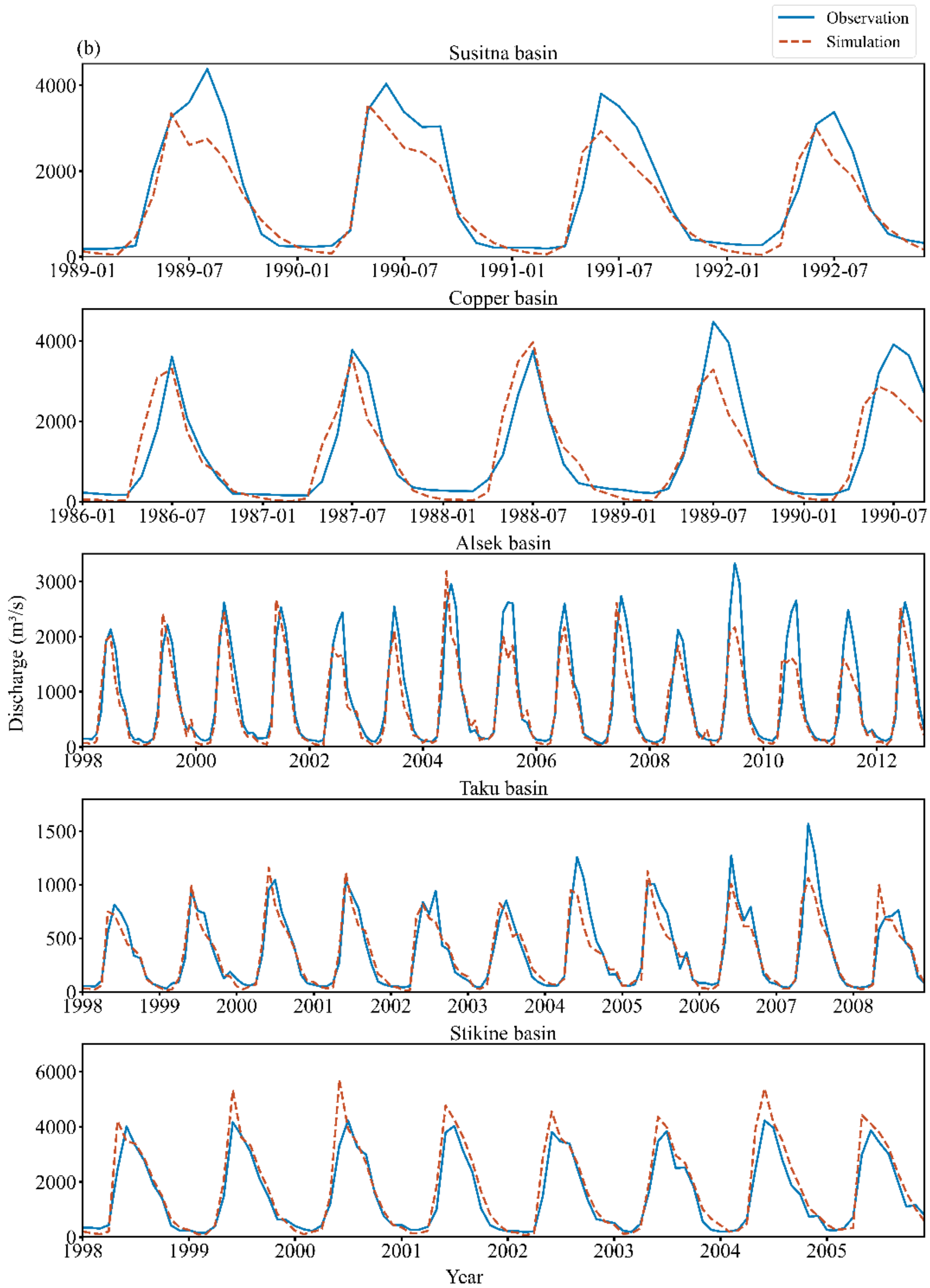

Fig. 2.3 Hydrograph results of calibration and validation.

Comparisons between simulated (red dashed lines) and observed (solid blue lines) monthly discharge values ($m^3 \cdot s^{-1}$) for the five basins: calibration (a) and validation (b).

2.3.2 Alaska discharge

The present subsection examines the combined Alaska discharge across the five basins plus the ungauged basins. The results in Fig. 2.4 indicate that the annual Alaska discharge is approximately 14,396 ± 819 $m^3 \cdot s^{-1}$ during the period of 1982–2022, with a substantial contribution from meltwater (53%; Fig. 2.5). In particular, the finding that melt runoff makes a significantly larger contribution to the total discharge than other contributors, such as direct rainfall, is consistent with the results of Neal et al. (2010) and Beamer et al. (2016). However, the estimated annual discharge is slightly less than the 19,000–26,920 $m^3 \cdot s^{-1}$ reported in existing studies (Beamer et al., 2016; Hill et al., 2015; Neal et al., 2010; Wang et al., 2004). This is because the present study uses a smaller area to avoid uncertainties in the discharge estimation from flat areas near coastlines. SWAT is considered to be difficult to accurately delineate streams and catchments in such areas due to the presence of large but shallow depressions and subtle variations (Moges et al., 2023). Additionally, the present study accounts for complicated hydrological processes in both the land phase and the channel phase, which may lead to a relatively high evapotranspiration and transmission loss.

The monthly discharge exhibits a strong seasonal cycle in response to temperature variations (Fig. 2.4). Specifically, the monthly discharge experiences a relatively constant average baseflow of 4252 ± 906 $m^3 \cdot s^{-1}$ from January to March compared to higher and more variable values in other seasons. This is primarily due to the low temperatures during January to March, which result in low meltwater (Fig. 2.5). The Alaska discharge starts to increase rapidly in April as the temperature rises above 0 °C. This increase is closely related to the change in meltwater, which reaches its peak in May, thus leading to a peak discharge of approximately 30,000 $m^3 \cdot s^{-1}$ in June (Fig. 2.4). Thereafter, the monthly discharge declines as the amount of meltwater decreases. This decline continues in the autumn, in contrast to the relatively high rainfall in late summer to early autumn, thereby indicating a less dominant impact of rainfall on the seasonal variability of discharge compared to the effect of temperature. During the melting season (i.e., from April to August), meltwater accounts for a significant proportion (77%) of the discharge (Fig. 2.5). Additionally, during this period, the meltwater experiences an increasing contribution (from 40% in April to 60% in August) from glacierized areas. Notably, this growing contribution against the overall decrease in meltwater from June to August suggests a possible increase in the amount of ice melt in glacierized areas, in agreement with the results of Beamer et al. (2016). The decrease in discharge continues at a drastic rate (4135 $m^3 \cdot s^{-1} \cdot month^{-1}$) from September to November, with meltwater contributing only 5% to the discharge in November. Finally, the monthly discharge in December returns to its baseflow level as the temperature drops below 0 °C.

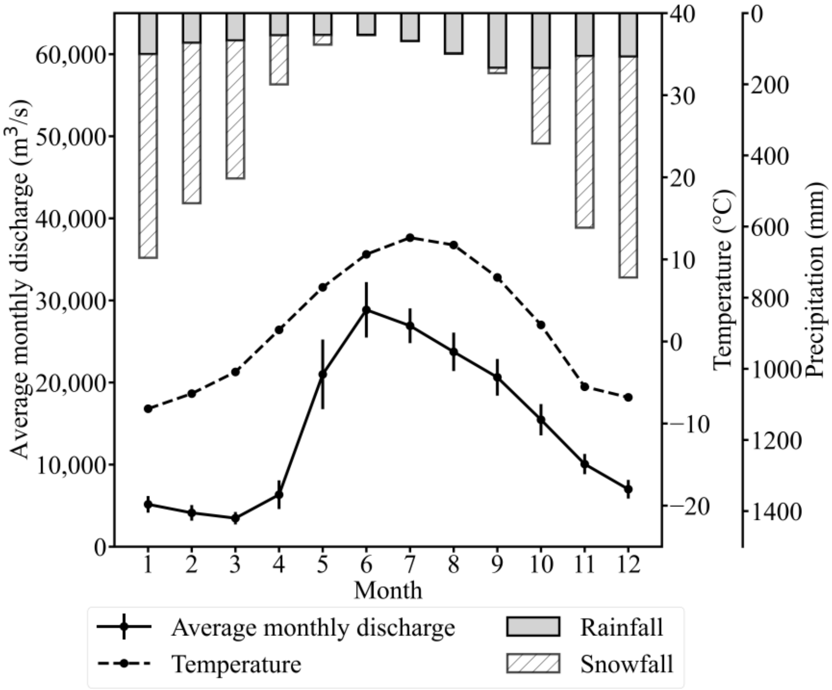

Fig. 2.4 The average monthly Alaska discharge.

The average monthly discharge (solid line), temperature (dashed line), rainfall (light gray bars), and snowfall (crosshatched bars) in the Alaska catchment.

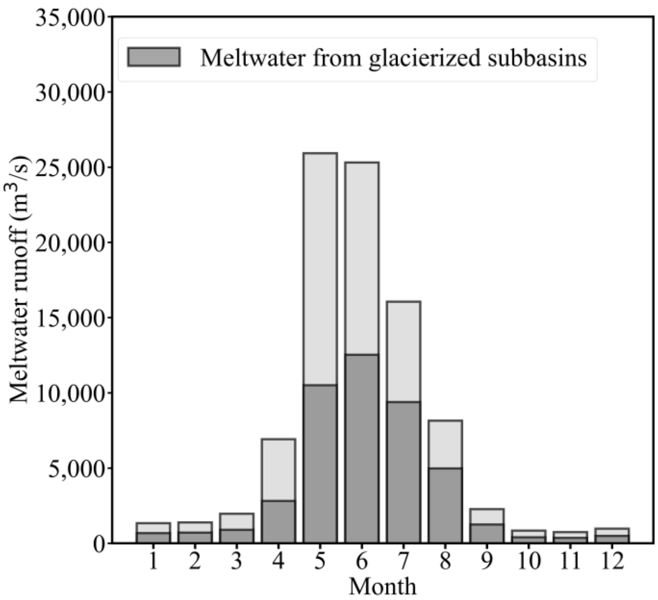

Fig. 2.5 The contribution of meltwater runoff from glacierized areas in the Alaska catchment.

Stacked plots of meltwater from the Alaska catchment (combined light and dark gray bars) and the meltwater from the glacierized areas (dark gray bars).

While no statistically significant trend is observed in the annual discharge during 1982–2022, the results in Fig. 2.6a indicate a decadal pattern. Moreover, a statistically significant correlation is found between the five-year running mean of the NPGO index and the Alaska discharge when a two-year time lag between them is considered ($p < 0.05$, $r^2 = 0.202$; Fig. 2.6b). This implies that the decadal variation in the Alaska discharge is influenced by long-term variations in the NPO. As noted above, the surface wind variability associated with the NPO is a crucial driving force for the NPGO, thereby suggesting that the NPGO is regarded as the oceanic expression of the NPO (Di Lorenzo et al., 2008). The NPO consists of two typical phases, namely the Aleutian below phase and the Aleutian above phase (Linkin et al., 2008; Rogers, 1981), and can therefore be represented by the NPGO index. Specifically, positive phases of the NPGO index correspond to the Aleutian below phase of the NPO, and are characterized by an enhanced Aleutian low pressure over a relatively wide region, including coastal and interior North America, along with an enhanced North Pacific High across the subtropical North Pacific that develops and shifts poleward. This atmospheric variability leads to intensified westerlies that subsequently blow over the central Pacific, thereby resulting in increased storminess along with higher precipitation and milder winter temperatures along the west coast of North America (Di Lorenzo et al., 2008; Linkin et al., 2008). Therefore, the hydrological processes may be subsequently influenced. Furthermore, the present study indicates that the NPO impacts the Alaska discharge with a lag of approximately two years. This time lag is deemed reasonable, as sea level pressure anomalies in the winter season primarily dominate precipitation in the form of snow, which may then influence melt runoff in the following seasons.

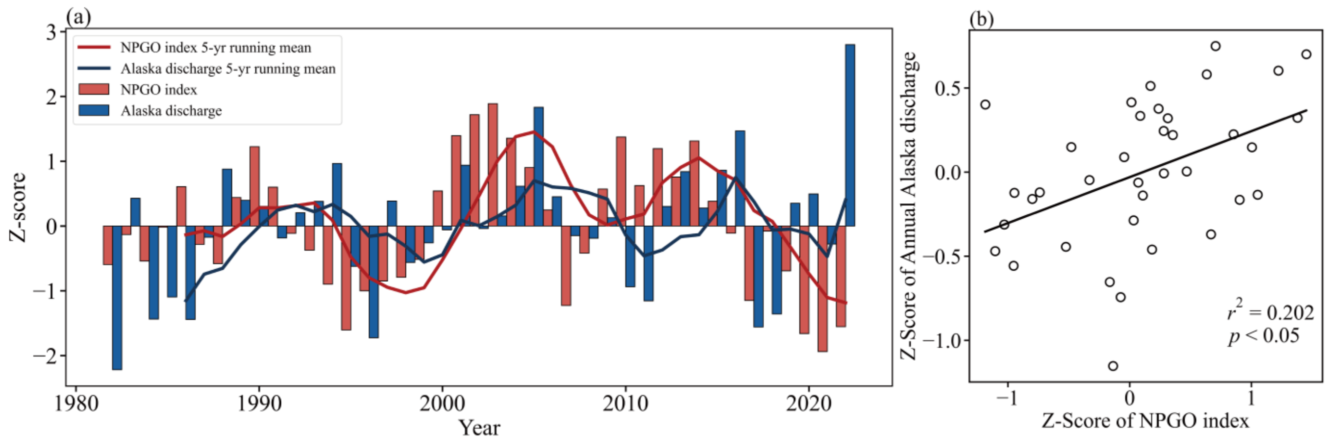

Fig. 2.6 The relationship between the interannual variation in the Alaska discharge from 1982 to 2022 and the NPGO index with a 2-year prior.

(a) The bar chart shows the Z-scores of the annual Alaska discharge (blue) and the NPGO index (red), along with line profiles representing the 5-year running mean of the annual discharge (black), and the NPGO index (red); (b) the scatter plot of the Z-score of the 5-year running mean NPGO index versus the annual Alaska discharge.

In addition, the monthly Alaska discharge exhibits significant interannual variations and significant increases of 65.52 and 63.71 $m^3 \cdot s^{-1} \cdot yr^{-1}$ in summer (June–August) and autumn (September–November), respectively, during 1982–2022 ($p < 0.05$; Fig. 2.7). These results can be attributed to the increases in winter snowfall and summer temperatures across the Alaska catchment. Specifically, it has been reported that the winter precipitation increased by roughly 4.9% $\cdot$ decade^{-1}, and the summer temperature increased by around 0.42 °C $\cdot$ decade^{-1}, during 1957–2021 (Ballinger et al., 2023).

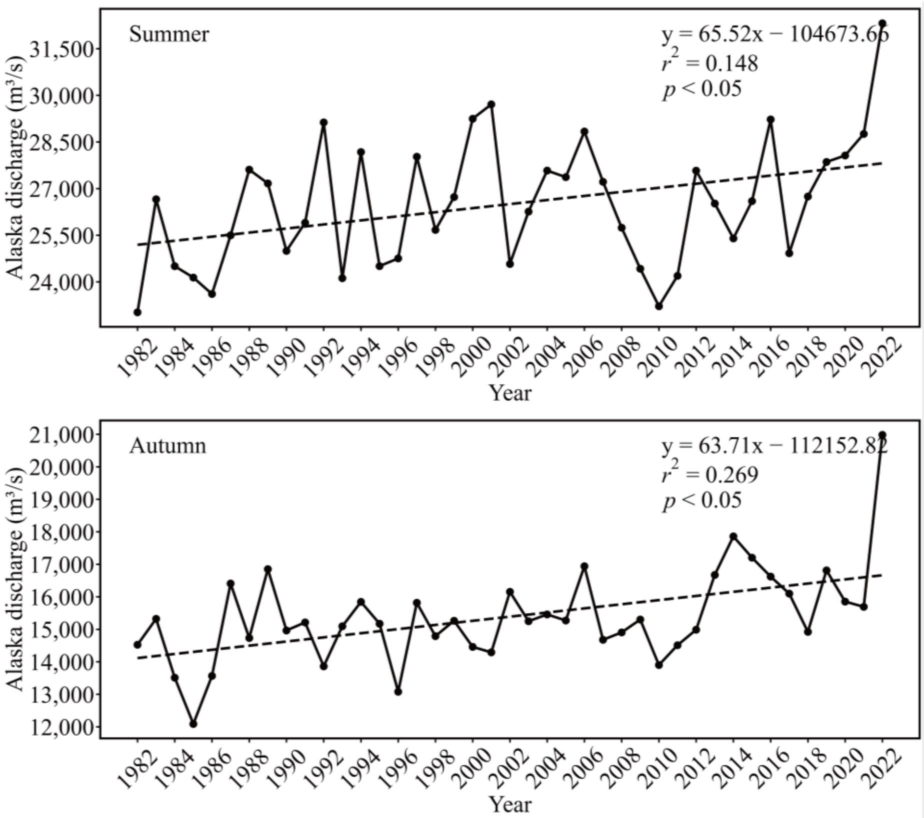

Fig. 2.7 The interannual variations (solid line) and trend (dashed line) of the Alaska discharge in summer and autumn during 1982–2022.

2.3.3 The discharge of the five basins and the ungauged basins

Fig. 2.8a, b show the total discharge from the five basins and the specific meltwater contribution, respectively, while the corresponding results for the ungauged basins are shown in Fig. 2.8c, d. Thus, during 1982–2022, the total annual discharge from the five basins was approximately 5848 ± 533 $m^3 \cdot s^{-1}$ (0.03 $m^3 \cdot s^{-1} \cdot km^{-2}$), including a substantial contribution from meltwater (58%). Specifically, the freezing temperatures from January to March resulted in minimal meltwater (138 $m^3 \cdot s^{-1}$ on average) and low rainfall (34 mm on average), thus leading to an average baseflow of 701 $m^3 \cdot s^{-1}$. The discharge experienced a drastic increase from 1495 $m^3 \cdot s^{-1}$ in April to 9216 $m^3 \cdot s^{-1}$ in May, and reached a peak discharge of approximately 15,000 $m^3 \cdot s^{-1}$ in June. From June to August, although the rainfall increased, the discharge of the five basins declined by approximately 1749 $m^3 \cdot s^{-1} \cdot month^{-1}$ in response to a rapid decline in meltwater. During the melting season (from April to August), the monthly discharge was approximately 9970 $m^3 \cdot s^{-1}$, with a considerable contribution of approximately 78% from meltwater, 36% of which came from glacierized areas. From September to December, the discharge decreased to a baseflow level at a rate of 2309 $m^3 \cdot s^{-1} \cdot month^{-1}$ as the temperature declined to below 0 °C. While no statistically significant trend is detected in the total annual discharge from the five basins between 1982 and 2022, the total monthly discharge in January, August, September, and November experienced a significant increase (Table A2.4).

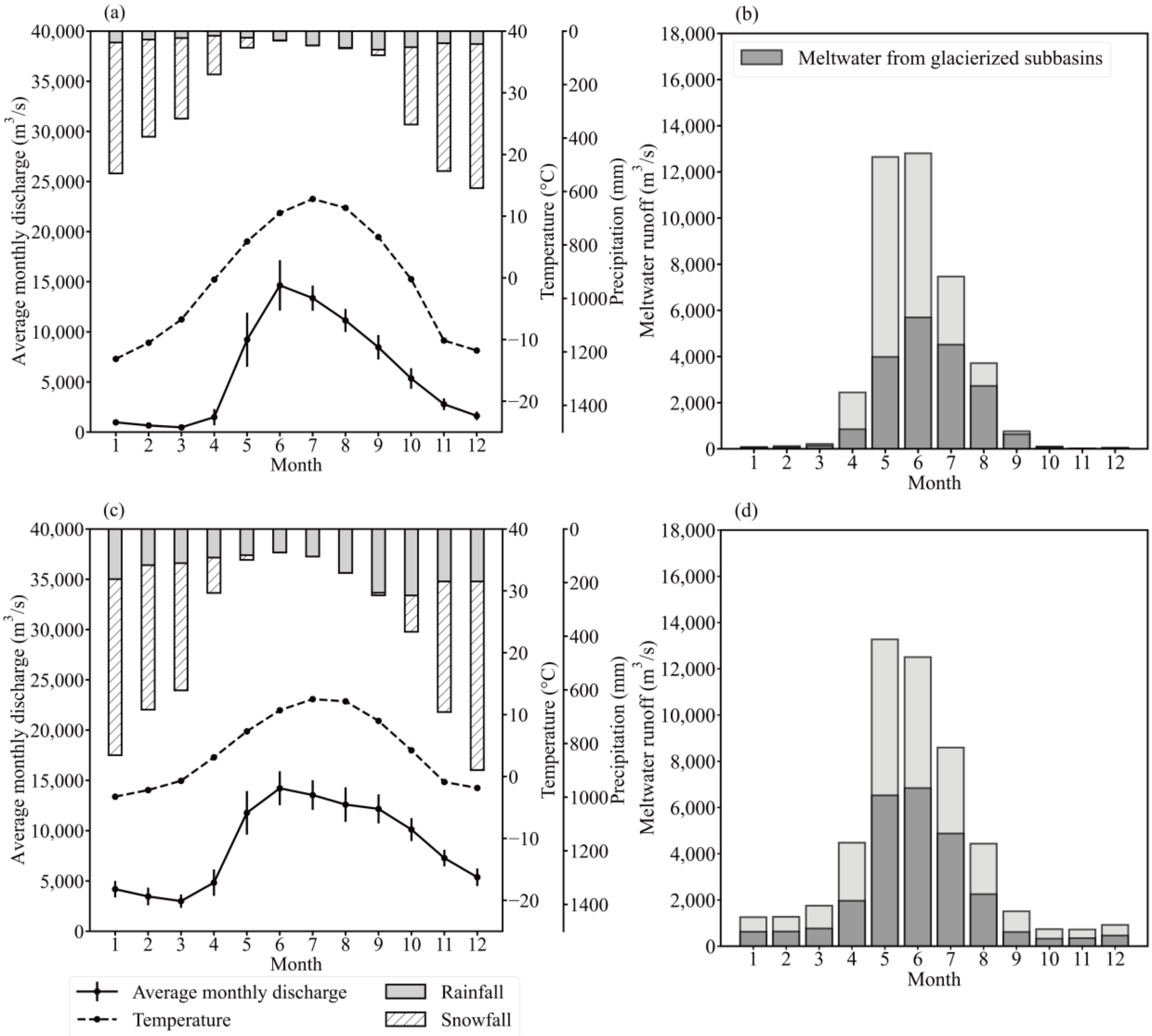

Fig. 2.8 The monthly discharge and melting results for five basins and ungauged basins.

(a) The total average monthly discharge from the five basins (solid line), along with the average monthly temperature (dashed line), rainfall (light gray bars), and snowfall (crosshatched bars). (b) Stacked plots of the total meltwater from the five basins (aggregate light and dark gray bars) and the meltwater from the glacierized areas (dark gray bars). (c,d) Same as (a,b) but for the ungauged basins.

Moreover, the ungauged basins (Fig. 2.8c, d) deliver a larger contribution of 59% to the Alaska discharge, compared to 41% from the five basins (Fig. 2.8a, b), despite having a smaller catchment area. This finding is in agreement with the results reported by Wang et al. (2004). The annual discharge of the ungauged basins is approximately 8548 ± 481 $m^3 \cdot s^{-1}$ (0.07 $m^3 \cdot s^{-1} \cdot km^{-2}$) during 1982–2022, with meltwater contributing approximately 50%. Specifically, the discharge in the ungauged basins from January to March is five times that of the five major basins. This is primarily because the temperature in the ungauged basins fluctuates more closely around 0 °C compared to that in the five basins, thereby resulting in more meltwater (1426 $m^3 \cdot s^{-1}$ on average) and rainfall (150 mm on average). Similarly to that from the five basins, the discharge from the ungauged basins begins to increase substantially in April as the temperature rises above 0 °C. However, the rate of increase from April to May is slower than that observed in the five basins, primarily due to the less drastic increase in temperature in the ungauged basins, which results in a smaller variation in meltwater. The discharge of the ungauged basins also reaches its peak in June, but at a lower rate than that in the five basins, due to a slight decrease in snowmelt during this period. From June to August, despite a slightly larger rainfall, the decrease in discharge continues at a rate of 810 $m^3 \cdot s^{-1} \cdot month^{-1}$. During the melting season (from April to August), the monthly discharge of the ungauged basins is approximately 11,396 $m^3 \cdot s^{-1}$, and again includes a larger contribution (76%) from meltwater than that received by the five basins. Of this contribution, 39% comes from glacierized areas. From August to October, the monthly discharge of the ungauged basins is approximately 11,627 $m^3 \cdot s^{-1}$, which is higher than that of the five basins due to the correspondingly higher rainfall and meltwater. The temperature drops below 0 °C from October to December, but remains higher than that in the five basins, thereby leading to relatively higher amounts of meltwater and, hence, higher baseflow. In addition, during this period, the higher rainfall contributes significantly to the higher baseflow in the ungauged basins relative to the five basins. While no statistically significant trend is detected in the annual discharge from 1982 to 2022, the monthly discharge from the ungauged basins exhibits a significant decreasing trend in May, and an increasing trend in August (Table A2.4).

Finally, the discharges from each of the five individual basins between 1982 and 2022 are shown in Fig. 2.9, where differences in the quantity and variation are observed. The annual specific discharges from the Stikine, Taku, Susitna, Alsek, and Copper basins are 0.036, 0.031, 0.03, 0.029, and 0.027 $m^3 \cdot s^{-1} \cdot km^{-2}$, respectively. Thus, the specific discharge in the southern portion (Stikine and Taku basins) of the Alaska catchment is generally higher than that in the northern part (Susitna, Alsek, and Copper basins). This is predominantly due to a higher annual precipitation in the southern part. Additionally, the Stikine and Taku basins receive a higher contribution from groundwater (approximately 600 $mm \cdot yr^{-1}$) compared to the northern part. The lowest specific discharge is observed in the Copper basin, which may be due to the limited precipitation (approximately 1800 $mm \cdot yr^{-1}$) and low average temperature (below −2 °C).

In terms of the trends, only the Susitna basin exhibits an increase in the annual discharge during the period of 1982 to 2022. Further, the Copper, Alsek, and Taku basins each exhibit a decrease in the monthly discharge in April, while all basins except the Stikine basin exhibit an increasing trend during August (Table A2.5).

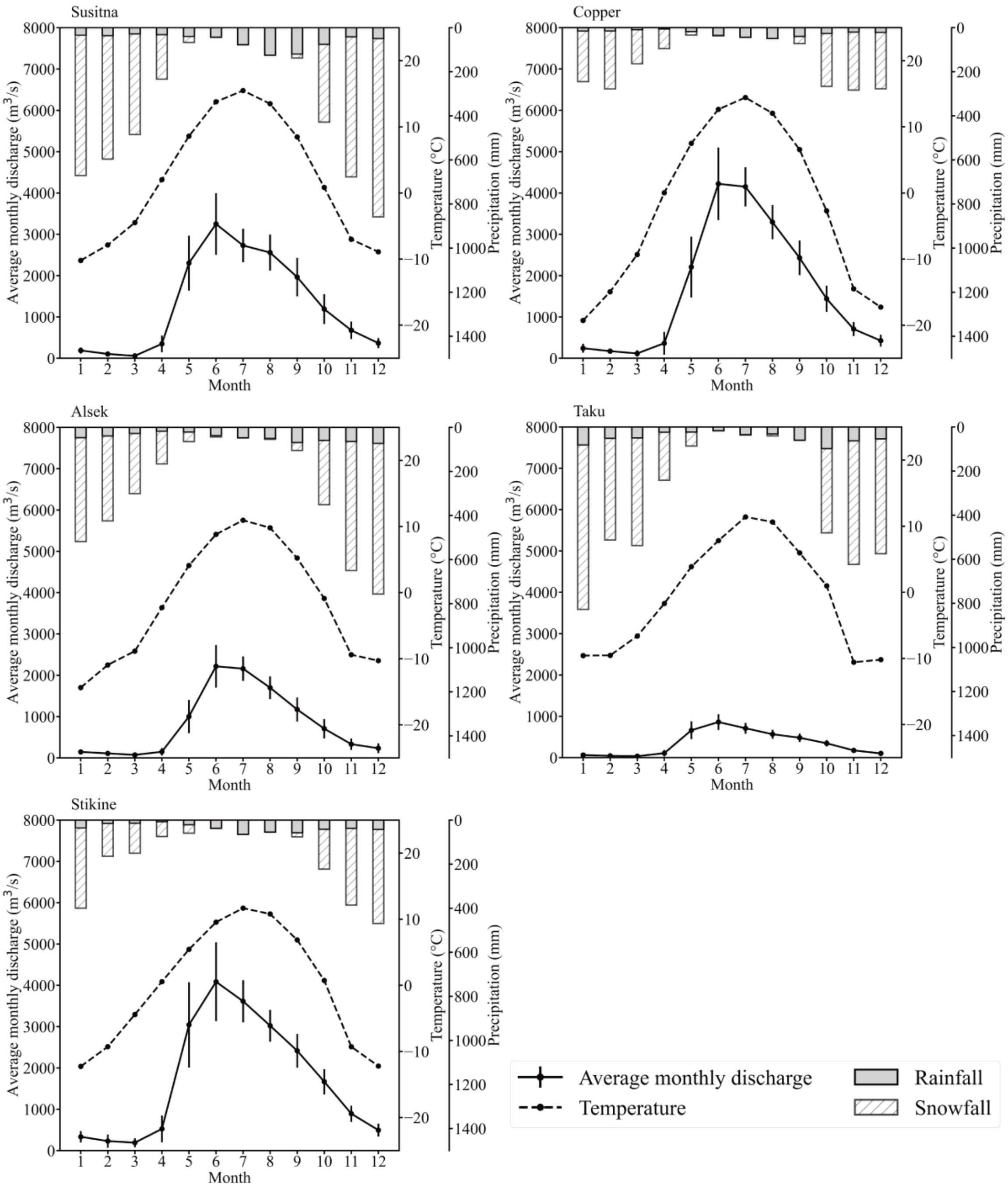

Fig. 2.9 The average monthly discharge for each of five basin.

The average monthly discharge (solid lines) and monthly temperature (dashed lines) for each of the five major basins, along with the rainfall (gray area) and snowfall (crosshatched area). The vertical error bars on the solid line indicate the range of one standard deviation.

2.4 Discussion

The freshwater discharge from the Alaska catchment may deliver cascading impacts on the neighboring ocean sector. After entering the GOA, the Alaska discharge primarily joins the Alaska Coastal Current (ACC). The ACC begins in the vicinity of the Washington–British Columbia border and travels at a speed of about 0.1 $m \cdot s^{-1}$ along the coast, carrying precipitation over the ocean and continental discharge into the Bering Sea (Royer et al., 2020; Weingartner et al., 2005). The ACC flows westward and southward along the Alaska coast and partially enters the Alaskan Stream before entering the Bering Sea through Unimak Pass . As shown in Fig. 2.10, the interannual variation of SSS in the Alaskan Stream during the period of 1984–2008 exhibits a statistical correlation with the variation in the annual Alaska discharge when considering a time lag, thereby suggesting that the Alaska discharge may impact the Alaskan Stream with a delay of two or three months ($p < 0.05$, $r^2 = 0.2$). Although these time lags are derived from statistical results, they are reasonable considering that the average distance covered by the ACC in going from the coastal regions of the GOA to the location of the Alaskan Stream is more than 500 km. Further, as Fig. 2.11 shows, the amplitude of SSS variation at Alaskan Stream, which is around 0.1 (Uehara et al., 2014), can be estimated by using the variations of the Alaska discharge $\Delta S = (FWD \times S_{ref})/V_{AS}$ (where ΔS is salinity variation; FWD is the Alaska discharge; S_{ref} is reference salinity; V_{AS} is the transport of the Alaskan Stream in the surface layer, which is assumed to be 1 Sv). In addition to the freshening effect of the continental discharge, other factors such as direct precipitation on the ocean, upwelling and current advection may also affect the seawater salinity of the Alaskan Stream (Di Lorenzo et al., 2009), thereby rendering the correlation less prominent. This significant correlation indicates that the Alaska discharge may influence the current circulation of the North Pacific Ocean through its impacts on the characteristics of the surrounding ocean.

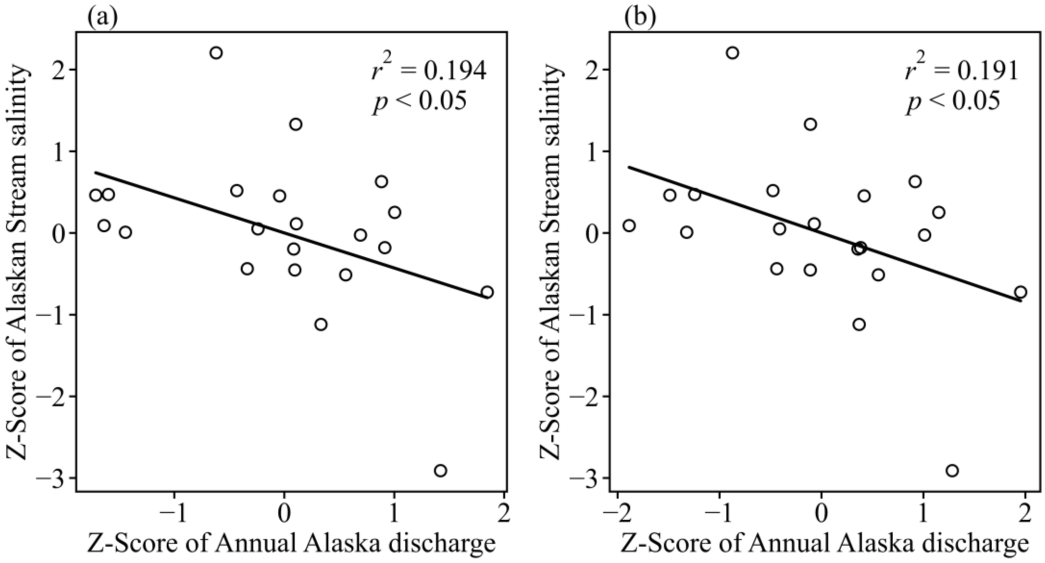

Fig. 2.10 Relationship between the Alaska discharge and the Alaskan Stream salinity.

Scatter charts show the correlation between the annual Alaska discharge and SSS anomalies in the Alaskan Stream with time lags of two months (a) and three months (b).

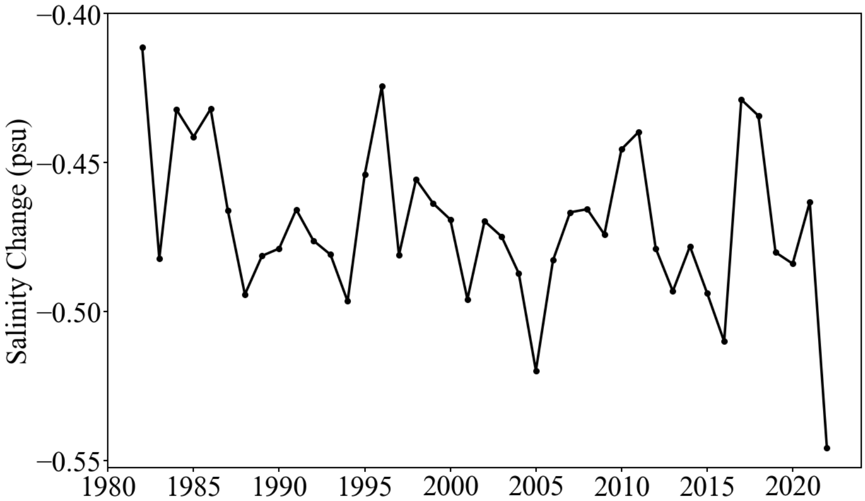

Fig. 2.11 An amplitude estimate of salinity anomalies caused by the interannual variations in the Alaska discharge.

The estimate is given by $\Delta S = (FWD \times S_{ref})/V_{AS}$, where ΔS is salinity variation; FWD is the Alaska discharge; S_{ref} is reference salinity; V_{AS} is the transport of the Alaskan Stream in the surface layer, which is assumed to be 1 Sv.

2.5 Conclusions

The Alaska discharge is characterized by large quantity and considerable variability, due to the complex interplay between climatic variations and mountainous topography, delivering cascading impacts on the coastal circulation beyond the regional scale. The present study estimated the quantity and variability of the continental discharge from the Alaska catchments under the continual fluctuations in temperature and precipitation in recent decades. The Alaska discharge was effectively estimated by using a process-based hydrological model known as the Soil and Water Assessment Tool (SWAT) with modified melting processes. During the estimation, SWAT was able to account for the complex spatial variability of land cover and soil features at the basin scale. The primary advances of this study are as follows: i) an update on the estimated discharge during recent years, ii) an analysis of the temporospatial variabilities in discharge, and iii) a first discussion on the relationship between continental discharge and large-scale oceanic circulation in this region.

The results indicate an annual Alaska discharge of 14,396 ± 819 $m^3 \cdot s^{-1}$, with a strong seasonal variability. In detail, the discharge maintains a baseflow level from January to March, when the temperature is well below freezing, and begins to increase drastically in April in response to rising temperatures. A peak flow of approximately 30,000 $m^3 \cdot s^{-1}$ occurs in June, after which the discharge decreases swiftly despite the relatively high rainfall during late summer to early autumn, and resumes its baseflow level in December. Meltwater plays an important role in the discharge accumulation process, contributing approximately 53% to the annual discharge and exerting a more dominant control than rainfall on the seasonal discharge variation. Notably, the ungauged basins provide a larger contribution of roughly 59% to the Alaska discharge, despite having a smaller catchment area, whereas the five basins provide the remaining 41%. The interannual variation in the Alaska discharge experiences an increasing trend for the summer and autumn, while the annual discharge exhibits no significant trend. The interannual variation in the Alaska discharge from 1982 to 2022 exhibits a decadal trend. Additionally, a significant correlation is found between the 5-year running mean of the Alaska discharge and the NPGO index, thereby suggesting that the NPO, a large-scale sea level pressure anomaly variation over the North Pacific, may affect the decadal variations in the Alaska discharge.

This study revealed an unprecedented significant correlation between the interannual variation in the Alaska discharge and SSS in the Alaskan Stream. The salinity anomalies potentially impact the overturning circulation through the current pathway, since it is situated in the upper branch of the pathway. The correlation becomes significant when a time lag of two or three months is assumed, which is reasonable considering the distance between the Alaska coastal outlets and the Alaskan Stream, along with the traveling speed of sea currents. Therefore, it is concluded that the regional discharge from the Alaska catchment could impact the variations in seawater anomalies in the North Pacific sector. Overall, the present study investigated the connection between large-scale climatic variations, Alaska discharge variations, and oceanic processes, which is expected to provide a broader understanding of the atmosphere–land–ocean relationship, especially in recent years.

Nevertheless, the present study has two major limitations. Firstly, while the temperature-index approach used to calculate meltwater is efficient, it is fairly simple. This method can be regarded as adequate for the monthly simulation presented herein, but a more complex method with high spatial resolution should be applied for the glacierized area. Secondly, parameterization might be improved based on more observation records in the calibration process for further improvement.

2.6 Appendix

Fig. A2.1 displays a schematic diagram of a possible salt pathway in the subarctic North Pacific comprising the North Pacific intermediate overturning (corresponding to Fig. 9 in Uehara et al. (2014). The orange arrows represent a surface salt pathway comprising an upper limb of the overturning from the subarctic gyre to the northern shelves in the Sea of Okhotsk, where the ventilation of the dense shelf water (DSW) occurs. The blue arrow denotes a lower limb of the overturning associated with the DSW outflow, which connects to the North Pacific Intermediate Water (NPIW).

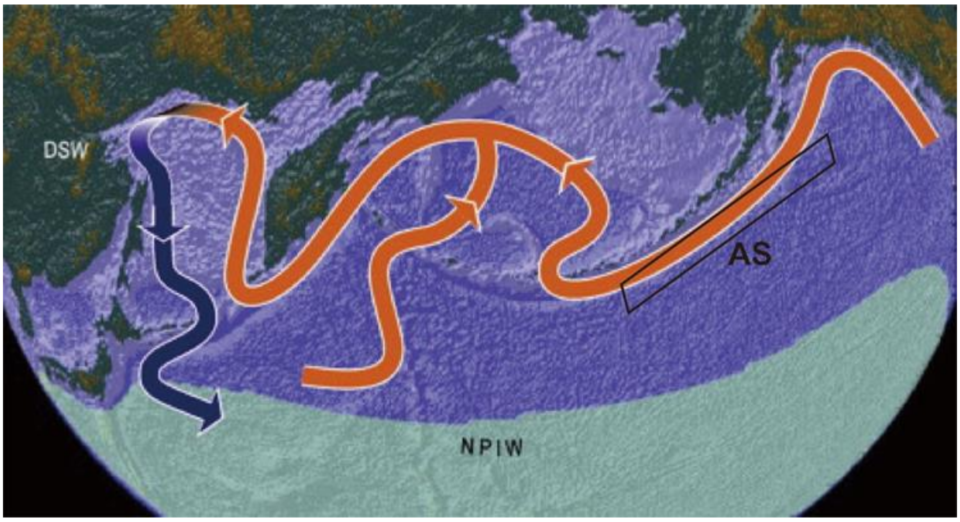

Fig. A2.1. A schematic diagram of a hypothesized salt pathway in association with an overturning from the surface flow in the subarctic gyre (orange arrows) to the intermediate layer (blue arrow) in the North Pacific Ocean. The box off the Alaska Peninsula denotes the area of analysis of observed data by Uehara et al. (2014) in the Alaskan Stream.

Fig. A2.2 displays the results of sensitivity analysis by SWAT-CUP in the Alsek basin for one example. The global sensitivity uses the p-value and t-stats for prioritization. The p-value determines the significance of the sensitivity, and values close to zero indicate the most significant parameters. The t-test was used to identify the relative significance of each parameter, and the higher the value (in absolute terms) the parameter has, the more sensitive it will be.

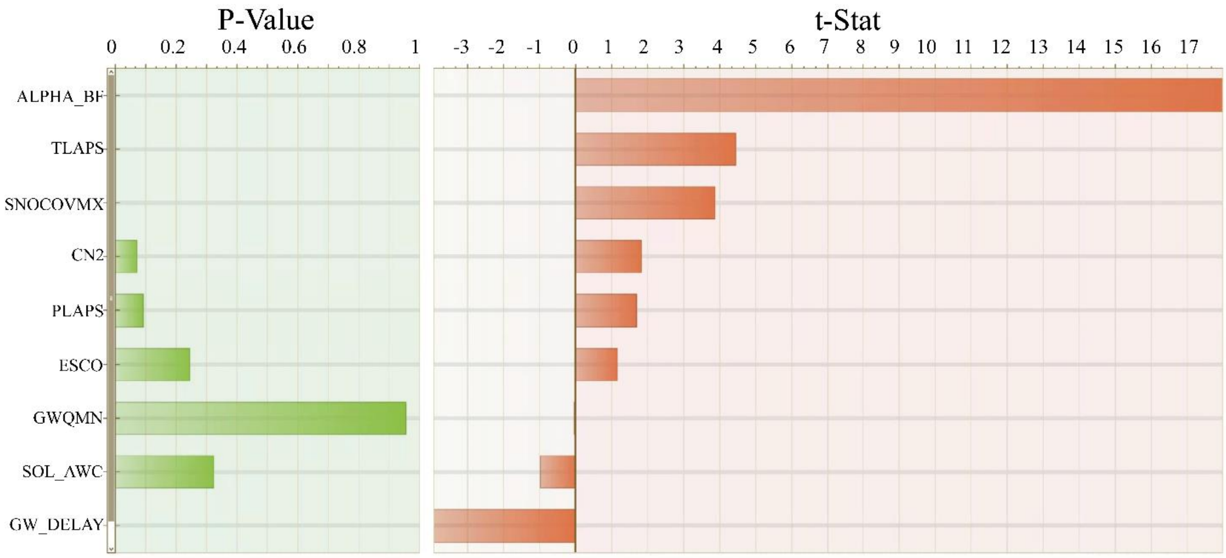

Fig. A2.2. Results of sensitivity analysis by SWAT-CUP in the Alsek basin.

Fig. A2.3 displays the dotty plot of the parameter ALPHA_BF in the Alsek basin, which indicates the parameter value versus objective function (NSE).

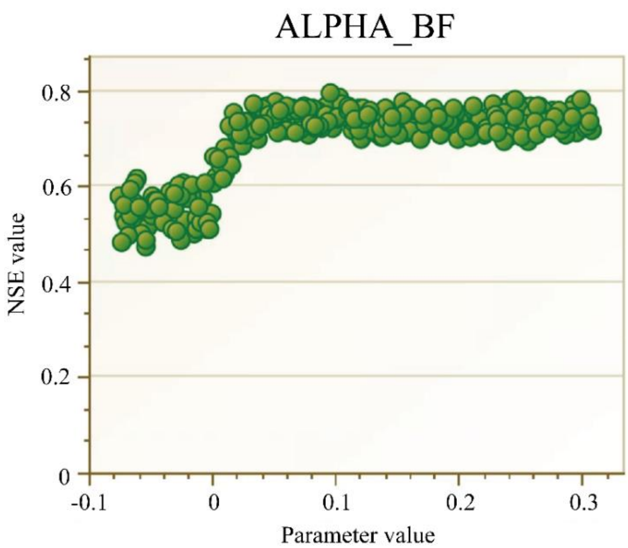

Fig. A2.3. Dotty plot of the parameter ALPHA_BF in the Alsek basin.

Table A2.1. Details of land cover classifications.

Land cover category	Land cover category in SWAT	
	Definition	Symbol
Temperate or sub-polar needleleaf forest; Sub-polar taiga needleleaf forest; Mixed forest	Forest-Mixed	FRST
Tropical or sub-tropical broadleaf evergreen forest	Forest-Evergreen	FRSE
Tropical or sub-tropical broadleaf deciduous forest; Temperate or sub-polar broadleaf deciduous forest	Forest-Deciduous	FRSD
Tropical or sub-tropical shrubland; Temperate or sub-polar shrubland; Sub-polar or polar shrubland-lichen-moss	Range-Brush, Shrubland	RNGB
Tropical or sub-tropical grassland; Temperate or sub-polar grassland; Sub-polar or polar grassland-lichen-moss	Range-Grasses, Herbaceous	RNGE
Sub-polar or polar barren-lichen-moss; Barren lands; Snow and Ice	Southwestern US Range, Bare Rock	SWRN
Wetland	Wetlands-Mixed	WETL
Cropland	Agricultural Land-Generic	AGRL
Urban	Urban Medium Density	URML
Water	Water	WATR

Table A2.2. Main land cover proportion in five gauged basins (% of each basin area).

Land cover category	Basin				
	Susitna	Copper	Alsek	Taku	Stikine
FRST	14.77	44.00	24.47	44.57	45.33
FRSD	7.39	6.08	2.10	1.48	1.63
RNGB	38.70	37.67	13.03	13.00	16.00
RNGE	0.18	0.78	7.63	4.63	4.91
SWRN	28.82	0	49.15	34.42	30.27
WETL	8.25	6.98	0.06	0.03	0.01
AGRL	0.02	0.01	0	0	0
URML	0.12	0.20	0.07	0	0.03
WATR	1.76	4.28	3.50	1.87	1.82

Table A2.3. The observational streamflow data used for model calibration and validation.

Basin	Gauging station	Location			Period
		Longitude	Latitude	Altitude (amsl*)	
Susitna	SUSITNA STATION AK	–150.51	61.54	12.19	1982–1992
Copper	NEAR CHITINA, ALAS	–144.46	61.47	121.92	1982–1990.9
Alsek	NEAR YAKUTAT	–138.10	59.39	76.20	1991.7–2012.11
Taku	NEAR JUNEAU, AK	–133.70	58.54	15.24	1987.8–2008
Stikine	NEAR WRANGELL	–132.13	56.71	7.62	1982–2005

*Above mean sea level

Table A2.4. A summary of the Mann-Kendall test (MK Zs) and the Sen's slope (SS) estimator results for the monthly discharge in the five basins and the ungauged basins. The values presented in bold indicate significant trends (p < 0.05, |Zs| >1.96).

Test	Jan	Feb	Mar	Apr	May	Jun	Jul	Aug	Sep	Oct	Nov	Dec
Five basins												
MK Zs	**2.75**	1.20	0.95	–1.13	–1.11	0.12	0.51	**3.13**	**2.64**	1.43	**2.89**	1.54
SS (m3/s)	9.58	3.46	2.45	–12.29	–45.31	5.77	9.84	48.92	43.31	14.72	21.75	9.31
Ungauged basins												
MK Zs	1.00	0.35	–0.10	–1.22	**–2.17**	0.95	1.90	**2.37**	1.83	1.74	1.40	0.10
SS (m3/s)	10.87	3.56	–0.80	–27.33	–72.80	23.28	45.10	59.58	37.35	20.38	15.12	1.18

Table A2.5. A summary of the Mann-Kendall test (MK Zs) and the Sen's slope (SS) estimator results for the average monthly discharge in the five individual basins. The values presented in bold indicate significant trends ($p < 0.05$, $|Zs| > 1.96$).

Test	Jan	Feb	Mar	Apr	May	Jun	Jul	Aug	Sep	Oct	Nov	Dec
Susitna basin												
MK Zs	**4.03**	**3.36**	**3.09**	0.91	0.58	**2.12**	**3.92**	**4.26**	**4.05**	**4.30**	**4.46**	**3.94**
SS (m3/s)	2.78	1.25	0.67	2.62	5.32	22.82	17.77	23.97	22.30	15.68	11.84	5.82
Copper basin												
MK Zs	0.15	–1.27	–1.38	**–2.39**	–1.48	–0.69	–1.07	**1.97**	1.45	0.28	1.68	–0.26
SS (m3/s)	0.16	–1.05	–0.79	–5.93	–12.47	–9.26	–7.39	10.97	8.96	1.88	3.33	–0.44
Alsek basin												
MK Zs	–0.24	–1.22	**–2.24**	**–2.68**	0.19	0.75	0.35	**2.33**	0.78	0.15	0.45	–0.73
SS (m3/s)	–0.13	–0.64	–0.77	–2.74	1.61	5.10	1.72	9.19	3.68	0.26	0.72	–0.83
Taku basin												
MK Zs	–0.69	–1.12	**–2.19**	**–3.31**	–1.34	–0.09	**2.08**	**3.49**	**2.48**	–0.30	–0.40	–0.43
SS (m3/s)	–0.24	–0.35	–0.46	–2.33	–3.94	–0.28	2.73	4.21	2.91	–0.39	–0.23	–0.13
Stikine basin												
MK Zs	**3.20**	1.92	1.94	0.08	**–2.57**	–1.72	–0.91	0.42	1.72	0.84	**1.99**	1.79
SS (m3/s)	5.46	2.77	2.42	0.27	–34.80	–23.60	–7.52	2.78	9.39	3.56	5.97	3.47

Chapter 3 Effect of freshwater discharge at the Northeast Pacific on the subtropical and equatorial ventilated thermocline

3.1 Introduction

The thermocline is an oceanic layer characterized by the strongest stratification, where temperature changes sharply with depth compared to the surrounding layers (Fiedler, 2010; Vallis, 2003). Its strength affects buoyancy, circulation, heat budgets and exchange of properties. Particularly, fluctuations in the equatorial thermocline play a pivotal role in climate variability, such as El Niño events which corresponds to a temporary warming of the surface waters of the eastern equatorial Pacific Ocean (Fedorov et al., 2004; Xu et al., 2017).

The thermal structure of the tropics and subtropics is influenced by wind-driven circulation in the upper ocean (Nonaka et al., 2006). In the subtropics, which is referred to as a "subduction" regions, wind forces surface water downward whereafter it moves along isopycnal surfaces toward the equator and upwells to gain heat. While wind forcing is the primary driver for the thermocline dynamics, other factors, such as the thermohaline processes due to temperature and salinity variations, may also provide crucial influence. Huang et al. (2000) identifies that surface cooling in the extratropics can induce warming of the equatorial thermocline. Furthermore, Fedorov et al. (2004) found that freshening of surface waters at high latitudes within subtropical gyres can inhibit the sinking of cold water, causing the cold tongue in the eastern equatorial Pacific to shrink and gain less heat. Notably, the equatorial thermocline tends to deepen as low-salinity water increases in higher latitude in the subtropical gyre. Under sufficiently strong low-salinity water forcing, the cold tongue disappears, preventing heat absorption and resulting in warm conditions across the tropics, such as the El Niño-like climate. These findings highlight the significant role of temperature and salinity variations in the subtropical gyres in shaping the equatorial thermocline. In addition to subtropical influences, subpolar region is suggested to connects the subtropical and equatorial regions via the wind-driven vertical circulation (Lu et al., 1998). Under global warming conditions, high-latitude freshening in subpolar regions has been shown to shoal the mixed layer depth, weaken vertical mixing, and trap CO_2-induced warming near the surface ocean (Zhang et al., 2012). Despite these insights, previous studies have primarily focused on the dynamical connections between subtropical gyres and the equatorial thermocline. The potential effects of freshwater fluxes (especially the freshwater discharge from surrounding continents) of the subpolar gyre on the equatorial thermocline remain largely unexplored. The investigation of how subpolar freshwater dynamics influence downstream ocean processes, including thermocline structure, is crucial for the understanding of the tropical climate variability.

The subpolar gyre in the northern hemisphere, located north of approximately 40°N, is characterized by cyclonic sea-surface circulation. In addition, coastal currents along the continental boundaries play a critical role in transporting freshwater discharge (FWD) from surrounding continents. Freshwater inputs from the Amur River, Kamchatka Peninsula, and the coastal regions of the Gulf of Alaska have been shown to significantly influence sea surface salinity (SSS) along the continental boundaries in the subpolar gyre. For example, a significant negative correlation is found between the salinity in the northwestern Sea of Okhotsk and the interannual variation of river discharge from the Kamchatka Peninsula (Shi et al., 2021). This indicates that continental FWD can be transported along with the coastal boundary currents, and influence SSS downstream. Additionally, the interannual variations of discharge from the Alaska mountainous catchment was found to have a negative correlation with the SSS anomalies of the Alaskan Stream with the former leading the later by 2 or 3 months (see Chapter 2; also

Xin et al., 2024). These studies highlight a critical role of subpolar boundary currents in redistributing freshwater and the effects of freshwater on modifying SSS.

In addition to contemporary FWD from rivers and drainage basins such as above, historical large-scale events such as ice sheet collapses have introduced massive amounts of freshwater into the ocean. One notable example is the collapse of the Cordilleran Ice Sheet (CIS) into the northeast Pacific. The CIS has the largest coverage during the Last Glacial Maximum (approximately 20 thousands years ago), with an average thickness of about 2 km (Walczak et al., 2020). During the end of the last glacial period, nearly half of the CIS mass is estimated to have collapsed within 500 years, as shown by Menounos et al. (2017). This event contributed approximately 3 meters to global sea-level rise. Such a massive FWD may influence salinity, stratification, and vertical circulation in the subpolar gyre, with downstream impacts on the subtropical and equatorial regions.

Therefore, the study in this chapter aims to investigate the effects of freshwater from different sources, especially those from the continental boundaries surrounding of the subpolar gyre, on the subtropical and equatorial thermocline and the related dynamics. Specifically, (i) freshwater input driven by evaporation minus precipitation across the Pacific Ocean, (ii) the present-day FWD from the continental boundaries surrounding of the subpolar gyre, (iii) the massive FWD caused by the CIS collapse into the northeastern subpolar gyre. Chapter 3 is organized as follows. Section 3.2 briefly describes the used data and experimental setup. Section 3.3 presents the results, focusing on the important characteristics of temperature, salinity, and density in various experiments. In section 3.4, the possible dynamics of how freshwater from the subpolar gyre influences the equatorial thermocline are discussed. Finally, the conclusions are given in section 3.5.

3.2 Data and methods

Experiments in this study are primarily separated into two parts; one is the control experiment with thermal forcing only, and the other is the freshwater discharge (FWD) experiment. These experiments are completed by using the MIT general circulation model (MITgcm), which is designed for studies of ocean circulation (Marshall et al., 1997). An idealized model is configured to capture the features of wind-driven circulation that is sensitive to SSS variations. The model domain represents a rectangular ocean basin that approximates the Pacific Ocean, spanning latitude from 60°S to 60°N and longitude from 120°E to 280°E; henceforth, this rectangular basin is called “the Pacific Ocean”. The horizontal resolution is set at 0.5°, with 49 vertical layers in the vertical direction to a depth of 4000 m. The wind curl stress across the ocean basin is average zonal wind (Fig. 3.1). Negative values indicate trade winds, while positive values mean westerlies. The initial temperature is set to 3°C for all grids. Then, the sea surface temperature (SST) is forced by the temperature that follows a latitudinal distribution as shown in Fig. 3.2, with a high temperature of 27.5°C in low latitudes and a low temperature of 5°C in the boundaries of high latitudes, adapting a relaxion period of 30 days. Similarly, the initial salinity is set to 34 PSU throughout the domain. Then, the SSS is forced by freshwater fluxes by the evaporation minus precipitation (E−P), as well as riverine discharges, as described in the next paragraph. In order to achieve a steady-state upper ocean circulation, the model is integrated over a 200-year period. These configurations are consistent across all experiments.

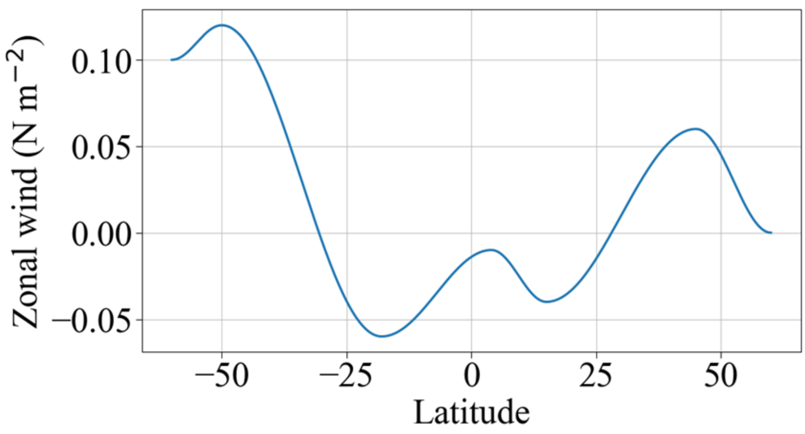

Fig. 3.1 Zonal wind across the ocean domain.

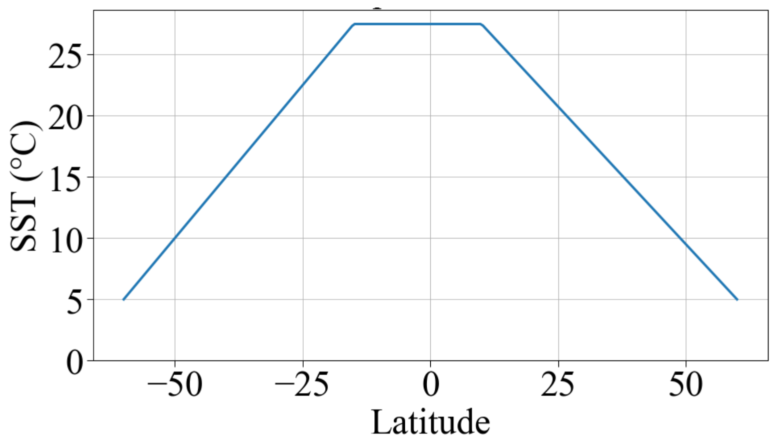

Fig. 3.2 Imposed SST.

Experiments were conducted with various freshwater fluxes. Firstly, the control experiment is conducted without freshwater input, so that the SSS remains constant. Secondly, regarding freshwater experiments, several conditions are considered in this study. Experiment I is designed by using the freshwater input represented by E−P (Fig. 3.3), which is obtained from the ERA-Interim reanalysis dataset (https://www.ecmwf.int/en/forecasts/dataset/ecmwf-reanalysis-interim/). The zonally averaged E−P within the rectangular ocean domain was calculated and is presented in Fig. 3.4. In low latitudes except for the region of intertropical convergence zone (ITCZ), evaporation exceeds precipitation, whereas precipitation dominates in high latitudes. Experiment II builds upon the experiment I by adding a boundary freshwater discharge along the northern boundary of the subpolar gyre (Fig. 3.5), from the latitude of 45°N to 60°N and longitude of 120°E to 280°E. The boundary freshwater discharge is mimicked by precipitation along the coast. The width of the boundary freshwater input is 1°. The boundary area which could be covered by the freshwater is estimated to be approximately 10^6 km^2. The boundary freshwater discharge from the northern surrounding continents including discharge from the Amur river (370 km^2/yr; Fujisaki et al., 2014), discharge from the Kamchatka Peninsula (278 km^2/yr; Shi et al., 2021), and the discharge form Alaskan mountainous catchment (480 km^2/yr; Xin et al., 2024). Thus, the estimated freshwater input along the northern boundary in this study is −2 m/yr as the discharge volume is translated into precipitation.

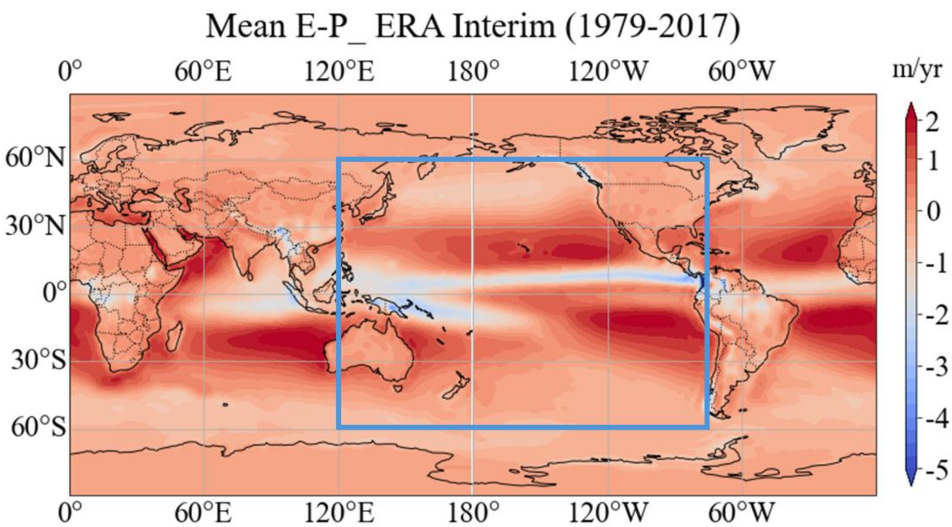

Fig. 3.3 Zonally averaged E−P form ERA-Interim dataset.

The color shade shows the value of zonally averaged E−P. The blue box shows the rectangular ocean domain.

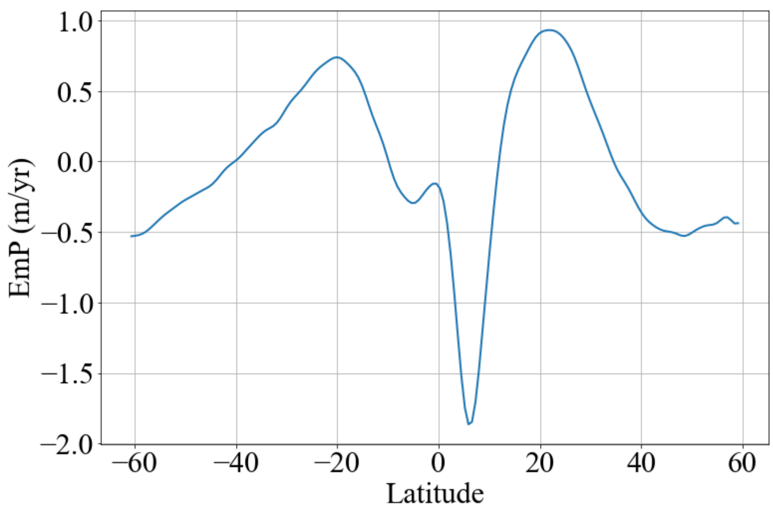

Fig. 3.4 Latitudinal distribution of E−P across the rectangular ocean domain.

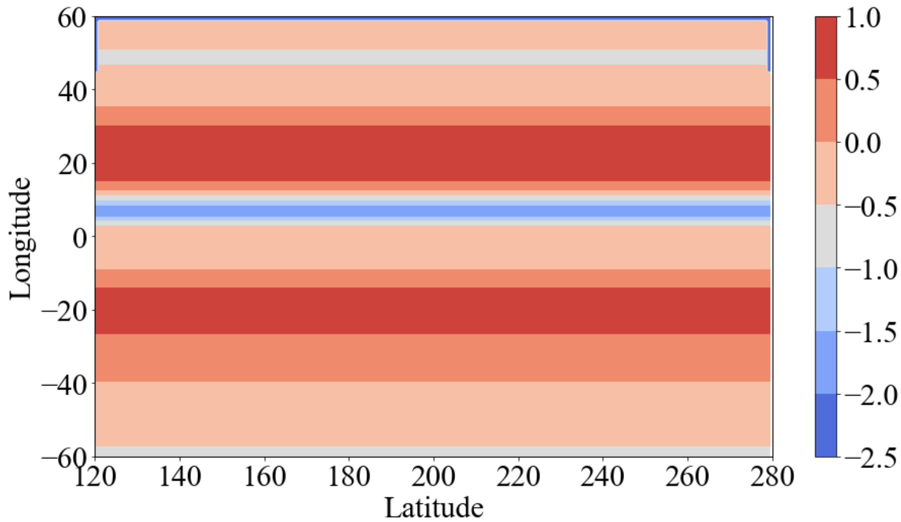

Fig. 3.5 Freshwater forcing in experiment II.

The color shade shows the latitudinal distribution of freshwater forcing, calculated as E−P combined with the FWD across the northern boundary of the rectangular ocean domain (−2 m/yr).

Additionally, extreme freshwater experiments, referred to as experiment III, are conducted based on experiment II by introducing a large amount of FWD from the ice sheet collapse (for example, Fig. 3.6 with a total of −60 m/yr at the northeastern boundary of the Pacific). As mentioned in the introduction section, this significant FWD can be provided by the collapse of the Cordilleran Ice Sheet (CIS) during the Last Glacial Period. The CIS reached its maximum extent during the Last Glacial Maximum, covering approximately 2.5 million km^2 with an average elevation of around 2 km (Walczak et al., 2020). Nearly half of the CIS mass is estimated to lose to the northeast Pacific within 500 years (Menounos et al., 2017). In this study, the freshwater discharge resulting from the CIS collapse is assumed to cover the northeastern corner of the basin (45°N to 60°N, 210°E to 280°E), with an area approximately 43,400 km^2. Finally, given the potential volume of the CIS and its estimated discharge area at the northeast Pacific, the freshwater discharge is calculated under several scenarios of collapse duration: 100, 120, 200, 500, and 2880 years. Correspondingly, the estimated freshwater discharge rates are approximately 60, 50, 30, 10, and 4 m/yr, respectively.

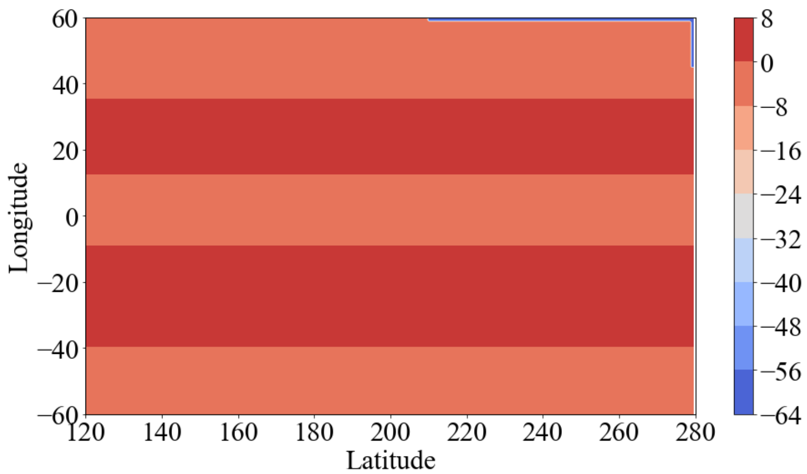

Fig. 3.6 Freshwater forcing in experiment III.

The color shade shows the latitudinal distribution of freshwater forcing, calculated as E−P combined with FWD from the northern subpolar boundary and CIS collapse, with a total of −60 m/yr at the northeastern corner.

3.3 Results

3.3.1 Control experiment

The SST from the control experiment without freshwater input is shown in Fig. 3.7. It can be observed that the SST exhibits a clear latitudinal distribution, with lower temperatures in the high-latitude regions of the subpolar gyre, and higher temperatures in the low-latitude regions. Especially, it can be noticed that SST is high in the western subtropical gyre, because of the presence of a northward flow of warm water from the equator to the northern subtropical gyre. This warm current is cooled as it moves eastward along the northern boundary of subtropical gyre by surface cooling due to the imposed SST, as well as mixing with surface cold and fresh water transported from the subpolar gyre through the Ekman transport. As the warm water cools, it subducts into the subsurface in the subtropical gyre (Fig. 3.8), contributing to the thermocline circulation. The cooled subducted water then travels equatorward and upwells in the equatorial region, especially leading to a region of low SST extending from the eastern equatorial Pacific Ocean, referred to as the "cold tongue". This cold tongue plays a critical role in the heat budget, as it is a region of significant heat gain. Additionally, at depths of 100–300 m, the temperature of the subsurface water displays a sharp vertical gradient (Fig. 3.8 and 3.9), indicating the presence of the ventilated thermocline. The equatorial thermocline exhibits a west-to-east slope, which is deeper in the western equatorial Pacific and gradually becoming shallower toward the eastern region (Fig. 3.9). This shallowing is associated with the upwelling of cold subsurface water to the surface in the eastern equatorial Pacific, leading to the formation of the cold tongue. The slope of the thermocline therefore has a significant influence on ocean-atmosphere interactions and climate variability both on regional and global scales.

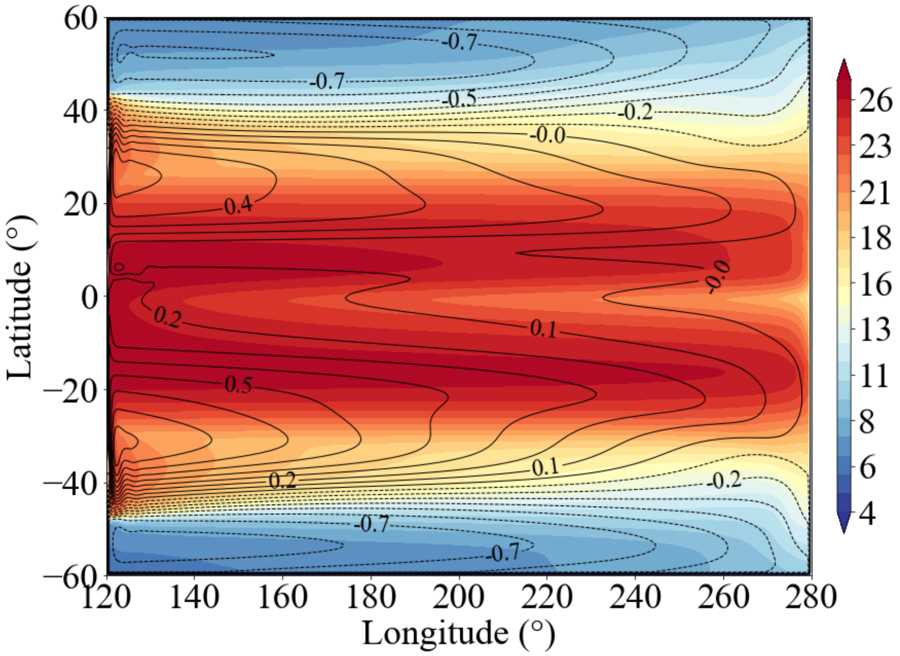

Fig. 3.7 SST and sea surface height for control experiment.

The color shade shows the SST and the contour lines represent the sea surface height.

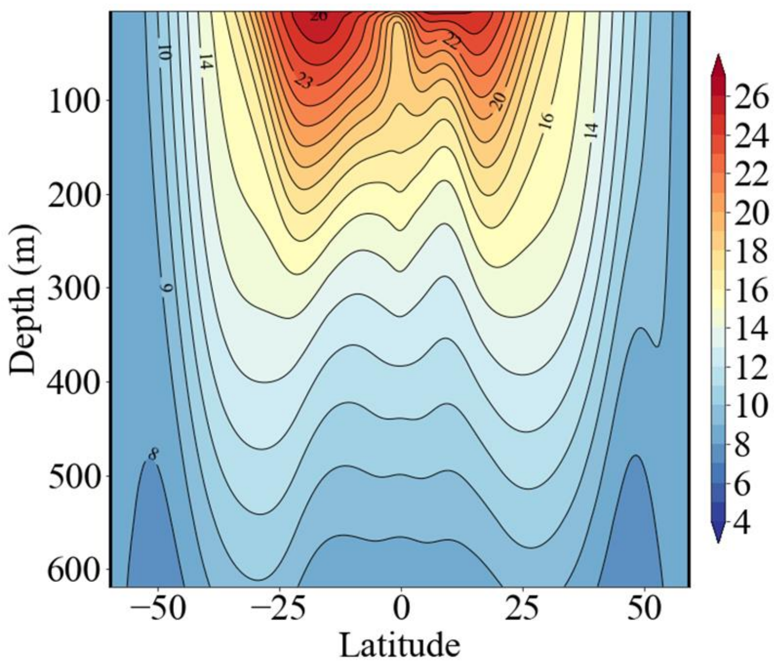

Fig. 3.8 Thermal structure along the 240°E meridional section for control experiment.

The color shade and contour lines show the potential temperature.

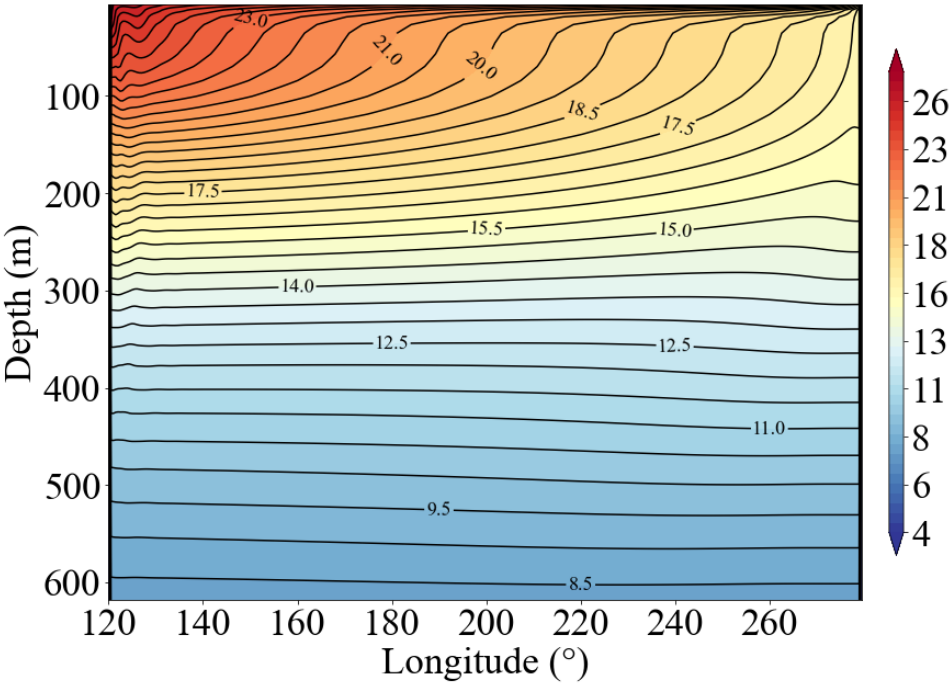

Fig. 3.9 Thermal structure along the equatorial plane for control experiment. The color shade and contour lines show the potential temperature.

The sea surface density is determined by SST, since the salinity is uniform across the study domain in the control experiment without freshwater input. Higher density is observed in the high-latitude regions of the subpolar gyre, while densities decrease toward the equator as latitude decreases (Fig. 3.10). Notably, the density in the western subtropical gyre is lower than that of other regions of the subtropical gyre, corresponding to the northward warm water advection. In contrast, the northern limb of the subtropical gyre features a sharp sea surface density gradient, indicating a front between the warm subtropical water and the cold surface water originating from the subpolar gyre. In addition, it is also observed that the density in equatorial region is higher than that of surrounding waters, due to the upwelling of cold water in the cold tongue region.

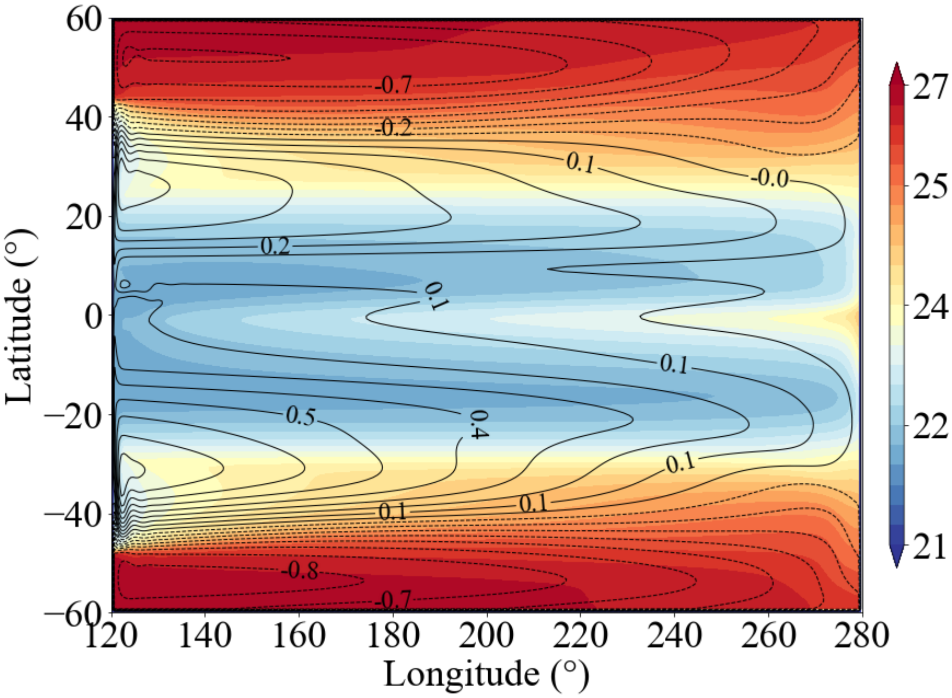

Fig. 3.10 Sea surface density and sea surface height for control experiment.

The color shade shows the sea surface density and the contour lines represent the sea surface height.

Since seawater moves along isopycnal surfaces, it is essential to examine the flow on these surfaces to understand the three-dimensional structure of ocean circulation. Therefore, the depth distribution and flow field on the isopycnal surface with a density of 24.5 kg/m^3, with which seawater upwells at the equator, were examined (Fig. 3.11). It is found that surface seawater, sinking from subtropical gyre outcrops (areas where the isopycnal surfaces intersect the sea surface), is transported along the isopycnal surface by geostrophic flow. Subsequently, this seawater is carried to the subsurface in the western equatorial region, it is then transported eastward by the equatorial undercurrent and eventually upwells to the surface. These findings reproduce the circulation along isopycnal surfaces that connect the subtropical gyre to the equator in the Pacific Ocean under the control experiment.

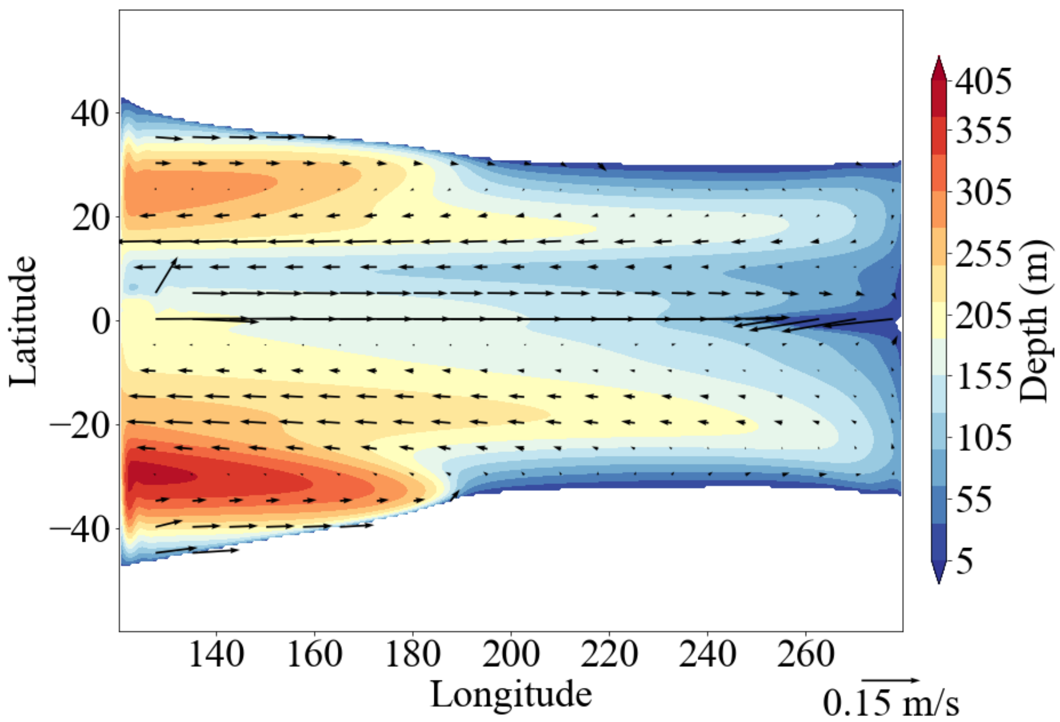

Fig. 3.11 Velocity field and depth distribution along the isopycnal surface (σ_θ = 24.5). The color shade represents the depth along the isopycnal surface. White part in high-latitude regions indicates isopycnal surface outcrops at the ocean surface. The arrows show the velocity field on this isopycnal surface.

3.3.2 Freshwater experiments

To investigate the effects of freshwater on the subtropical and equatorial ventilated thermocline, the model is run with various freshwater input scenarios. The findings are detailed in the following sections. Specifically, the results of experiment I, which applies the E−P forcing obtained from the ERA-Interim dataset, are shown in section 3.3.2.1. Section 3.3.2.2 presents the findings from experiment II, which builds upon experiment I by including boundary FWD in the northern subpolar gyre. Additionally, the results related to the experiment III, which is built upon experiment II and FWD from the CIS collapse, are shown in section 3.3.2.3. Finally, variations in the SST gradient and the equatorial thermocline depth are presented in section 3.3.3.

3.3.2.1 Experiment I forced by ERA-Interim E−P data

The SSS across the model domain exhibits significant spatial variations, showing a latitudinal distribution due to the impact of E−P dataset obtained from ERA-Interim. As shown in Fig. 3.12, SSS is lower in the subpolar gyre and the regions of the ITCZ due to significant precipitation, while higher in the subtropical gyre of both hemispheres because of evaporation. Additionally, compared to the control experiment, SSS increases in the subtropical gyre of southern hemisphere, primarily driven by a high E−P value, while the subtropical gyre in the northern hemisphere experiences a decrease in SSS. Notably, in the northern hemisphere, high-SSS water in the subtropical gyre flows northward along the western boundary, then turns eastward in the northern edge of the subtropical gyre. Whereas low-SSS water flows along the western and southern boundary of the subpolar gyre and freshens the surface water of the northern subtropical gyre by Ekman transport. These findings indicate that low-SSS water caused by high precipitation in the subpolar gyre can significantly influence the SSS in the subtropical gyre. Additionally, low-SSS water from the ITCZ regions appears to affect the western boundary of the subtropical gyre in the North Pacific (Fig. 3.12 and Fig. 3.13).

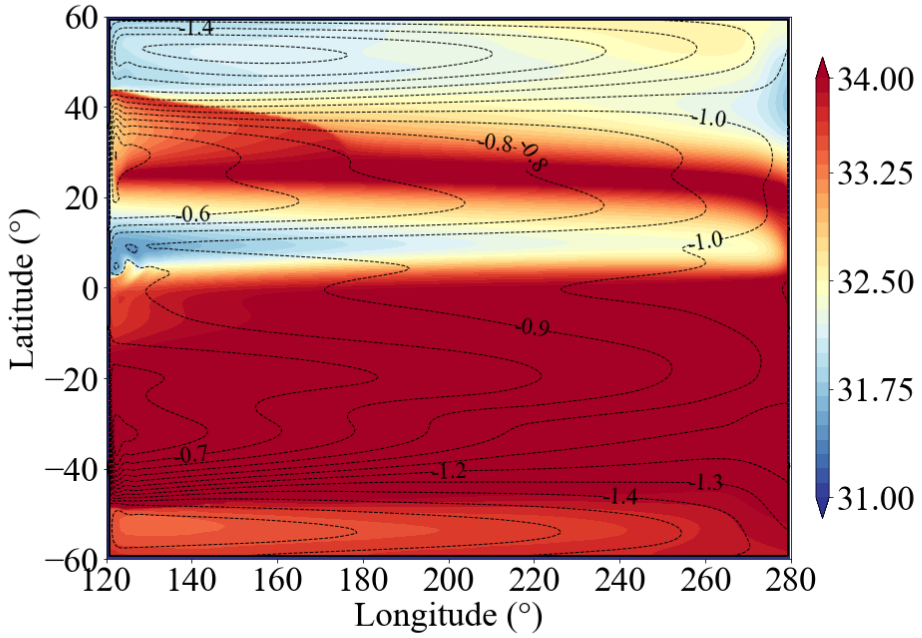

Fig. 3.12 SSS and sea surface height for experiment I.

The color shade shows the SSS and the contour lines represent the sea surface height.

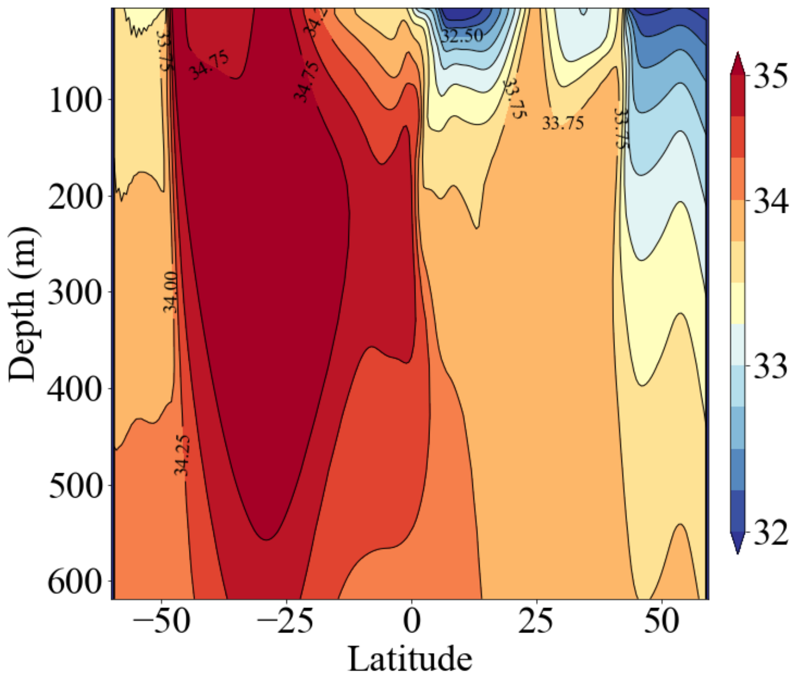

Fig. 3.13 Salinity structure along the 125°E meridional section for experiment I.

The color shade and contour lines show the salinity.

Sea surface density changes are closely associated with variations in SSS. Compared to the control experiment, experiment I shows a significant reduction in density within the subpolar gyres and ITCZ regions, where substantial precipitation decreases SSS (Fig. 3.14). High-density surface water dominates the subpolar gyres in both hemispheres, while lower latitudes are characterized by low-density surface water. Notably, the internal regions of the subtropical gyres exhibit increasing density due to high evaporation, forming sharp gradients around 25°N in both hemispheres. However, the eastern subtropical gyre exhibits a reduced density, corresponding to the lower SSS in this region. In the eastern equatorial region, consistent with the control experiment, the upwelling of cold water results in higher sea surface density compared to the surrounding waters.

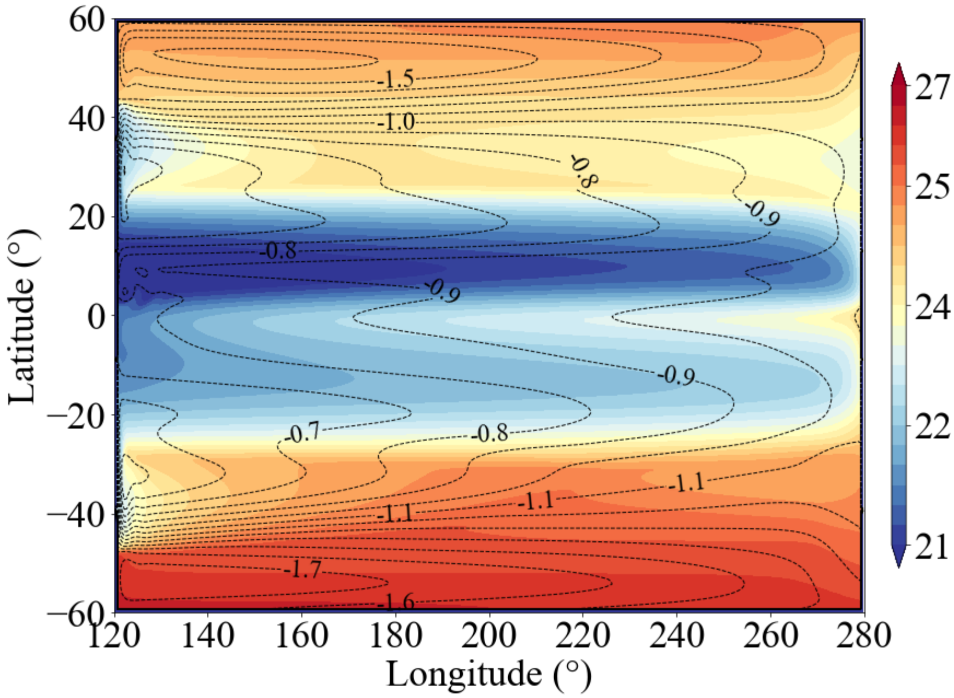

Fig. 3.14 Sea surface density and sea surface height for experiment I.

The color shade shows the sea surface density and the contour lines represent the sea surface height.

Thermal structure anomaly along the equatorial plane (Fig. 3.15) shows the differences between experiment I and the control experiment. Under the influence of E−P forcing in experiment I, the equatorial water temperature, particularly at depths of 200–400 m, increases significantly. Temperature anomalies of approximately 2°C are observed in the western equatorial region, while anomalies of around 1°C occur in the eastern part. These findings suggest that the redistribution of SSS, driven by significant precipitation in the subpolar gyres and the tropics as well as intensified evaporation in the subtropical gyres, impacts the equatorial thermocline structure.

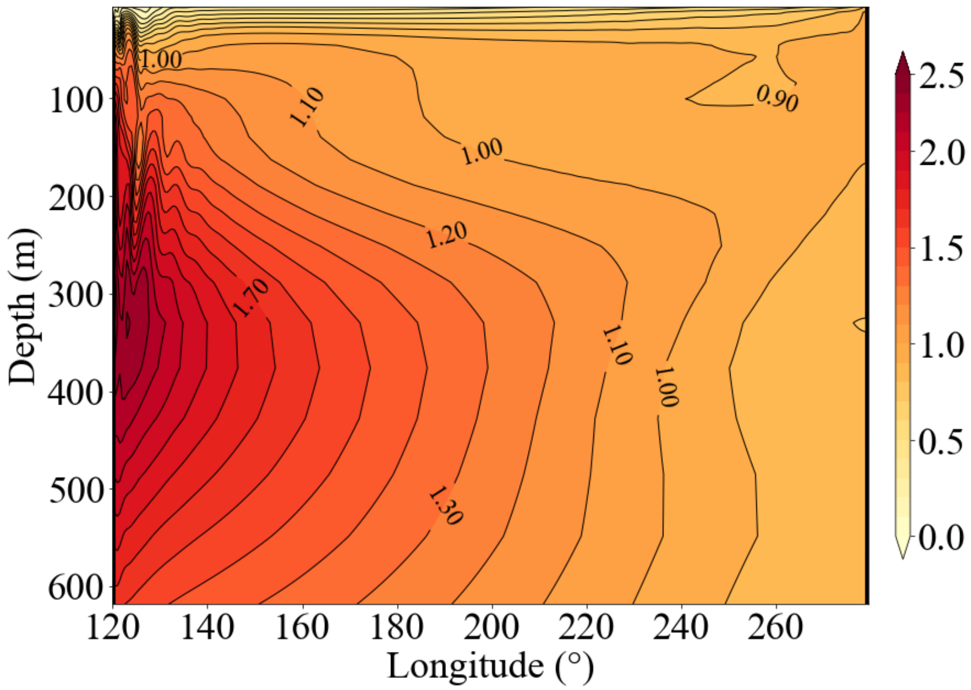

Fig. 3.15 Thermal structure anomaly along the equatorial plane between the experiment I and control experiment.

The color shade and contour lines show the difference of the potential temperature between experiment I and control experiment.

3.3.2.2 Experiment II forced by ERA plus the boundary FWD

To investigate the effects of FWD from the continents surrounding the subpolar gyre on the ocean characteristics in the Pacific, I diagnosed variations in SSS, sea surface density, and thermal structure for experiment II. As shown in Fig. 3.16, the SSS in the subpolar gyre is significantly reduced compared to experiment I. The extent of low-SSS water in the eastern subtropical gyre increases in experiment II. Notably, low-SSS surface water is found to be tightly trapped along the continental boundaries of the subpolar gyre, flowing southward along the western boundary and turning eastward along the southern boundary of the subpolar gyre. This boundary current with much lower salinity than in experiment I, leads to reduced SSS in the northern boundary of subtropical gyre through Ekman transport. These findings indicate that FWD from the subpolar gyre boundaries significantly influences the SSS distribution in the subtropical gyre of the North Pacific.

In experiment II, high-density surface water continues to dominate the subpolar gyre, while lower-density water is observed at lower latitudes, except for the cold tongue in the eastern equatorial Pacific (Fig. 3.17). Notably, in the North Pacific, the continental boundary of the subpolar gyre exhibits lower density compared to experiment I, which corresponds to the presence of trapped low-salinity boundary currents along the continental boundaries. Furthermore, although the sharp density gradient around 25°N persists, the overall density in the subtropical gyre is reduced.

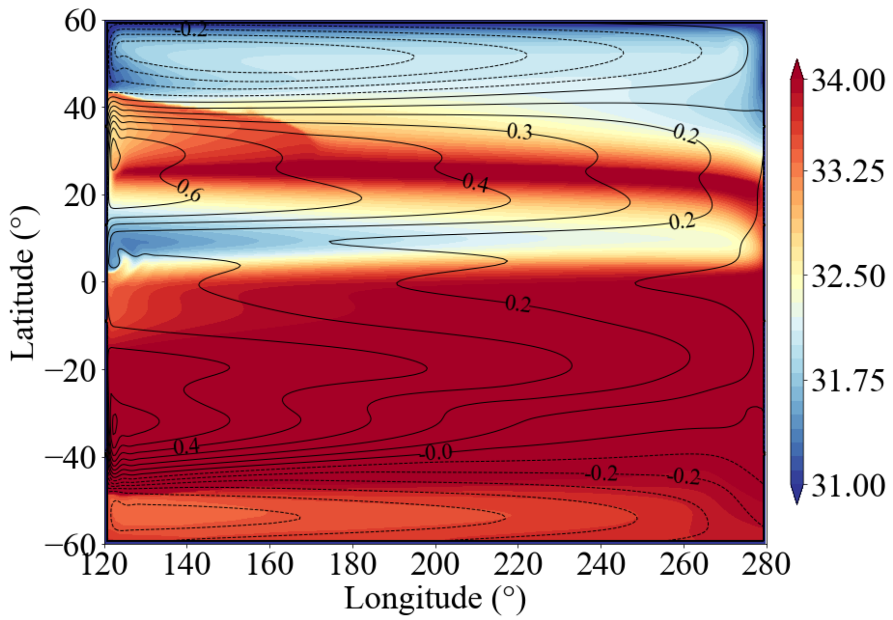

Fig. 3.16 SSS and sea surface height for experiment II.

The color shade shows the SSS and the contour lines represent the sea surface height.

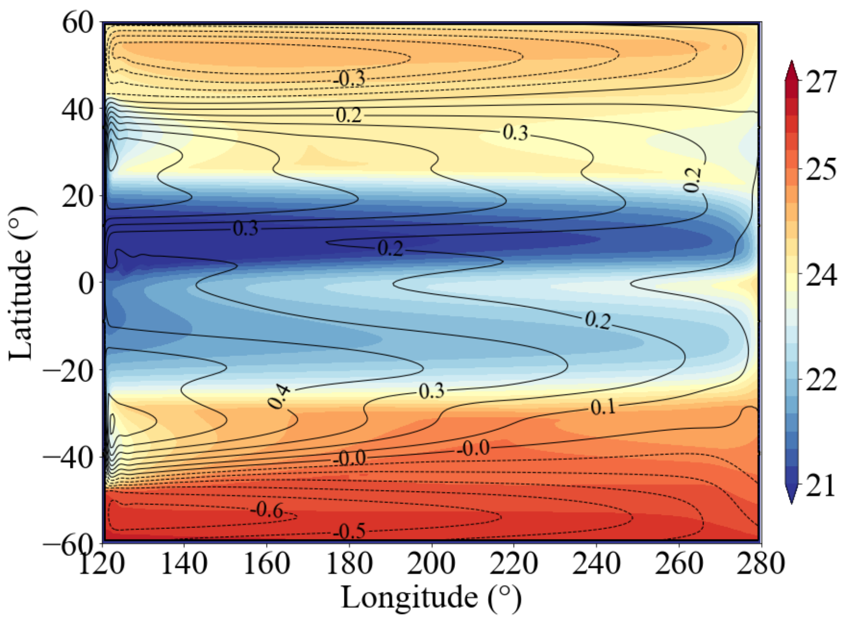

Fig. 3.17 Sea surface density and sea surface height for experiment II.

The color shade shows the sea surface density and the contour lines represent the sea surface height.

The thermal structure anomaly along the equatorial plane highlights the differences between experiment II and experiment I (Fig. 3.18). A slight cooling is observed in the upper ocean (approximately 120 m) of the western equatorial Pacific, while the temperature of subsurface water in the western equatorial region, particularly at depths of 200–600 m, increases by approximately 0.1°C. This warmed subsurface water contributes to temperature increases in the eastern equatorial region through the equatorial undercurrent and upwelling processes. These findings suggest that FWD at the northern boundary of the subpolar gyre influences the thermal structure along the equatorial plane, with distinct effects on upper and subsurface water layers.

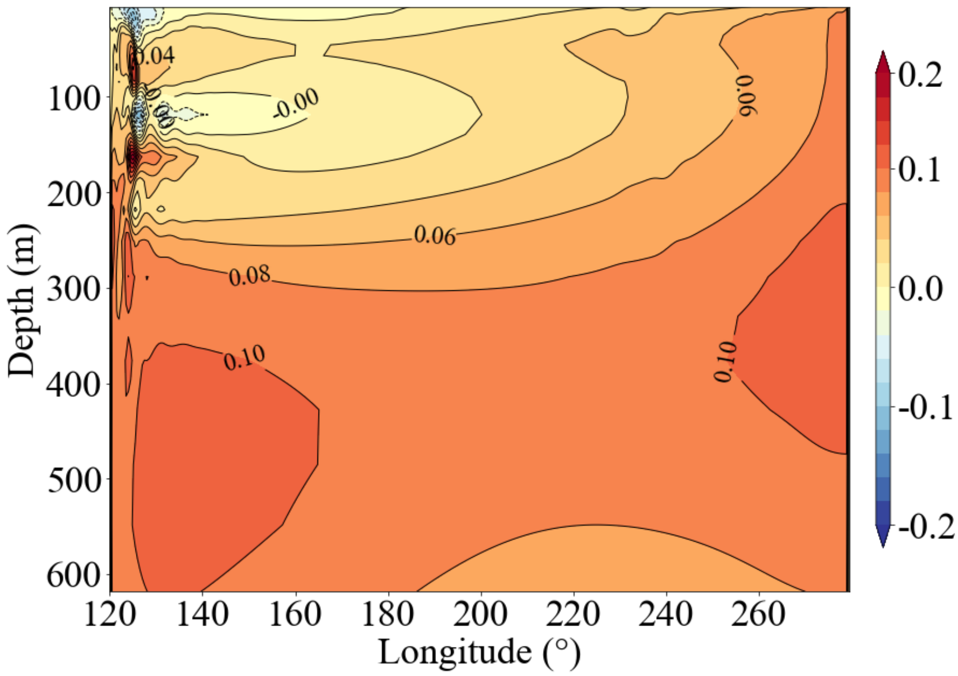

Fig. 3.18 Thermal structure anomaly along the equatorial plane between the experiment II and experiment I.

The color shade and contour lines show the difference of the potential temperature between experiment II and experiment I.

3.3.2.3 Experiment III with extreme FWD

By applying various scenarios of FWD from the CIS collapse, including 4, 10, 30, 50, and 60 m/yr, I explored the effects of the significant FWD from the northeast Pacific on the equatorial ventilated thermocline. To clearly present the findings, results from the experiment III, which is forced by the highest FWD of 60 m/yr, are highlighted among these scenarios.

Under the extreme FWD condition, SSS is significantly reduced in both the northern and southern hemispheres (Fig. 3.19). Notably, SSS decreases not only along the boundaries of the subpolar gyre but also within its open ocean areas. The northern part of the subtropical gyre experiences significant freshening due to the transport of low-salinity water from the subpolar gyre via Ekman transport. A crucial difference compared to experiments III and I is observed in the northwestern subtropical gyre (approximately 40°N, 120−180°E), where the Kuroshio Extension-like current is located. This region becomes dominated by freshwater transported from the subpolar gyre. In contrast, relatively high-salinity water remains confined to regions near 25°N. Therefore, the substantial FWD from the CIS collapse into the northeast Pacific leads to a significant redistribution of SSS in the North Pacific.

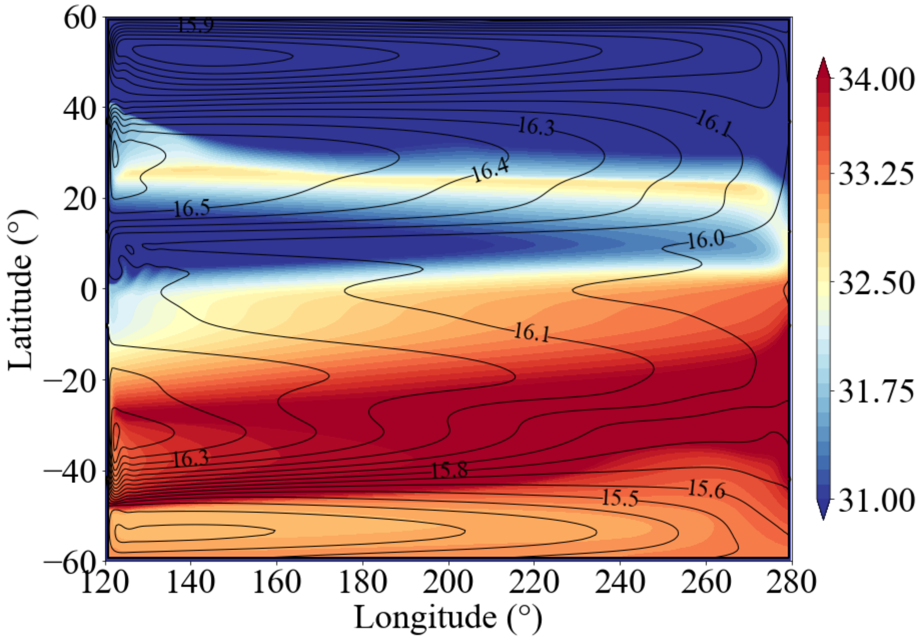

Fig. 3.19 SSS and sea surface height for experiment III.

The color shade shows the SSS and the contour lines represent the sea surface height.

In experiment III, sea surface density is significantly reduced across both the North and South Pacific (Fig. 3.20). Particularly, in the North Pacific, low-density surface water is prominently trapped within the boundary currents of the subpolar gyre, which corresponds to the distribution of SSS. It is important to highlight that the western regions of the boundary between the subpolar and subtropical gyres (approximately 35−50°N, 120−180°E) exhibit significantly lower density compared to their surroundings. Additionally, a larger portion of the eastern subtropical gyre, compared to experiment II and I, is dominated by low-density water. Furthermore, the SST gradient between western and eastern Pacific is reduced (can be seen later in Fig. 3.24), suggesting that such extreme FWD condition potentially impacts the equatorial thermal structure. Regarding the meridional section of density along the 240°E, low-density water is found not only in the northern subpolar gyre but also extends into the subtropical gyre in the northern hemisphere (Fig. 3.21). The thick layer of high-density surface water in the northern subtropical gyre subducts at the regions of approximately 25°N and is transported along the isopycnal surface toward the equator, resulting in a sharp density gradient at the equator.

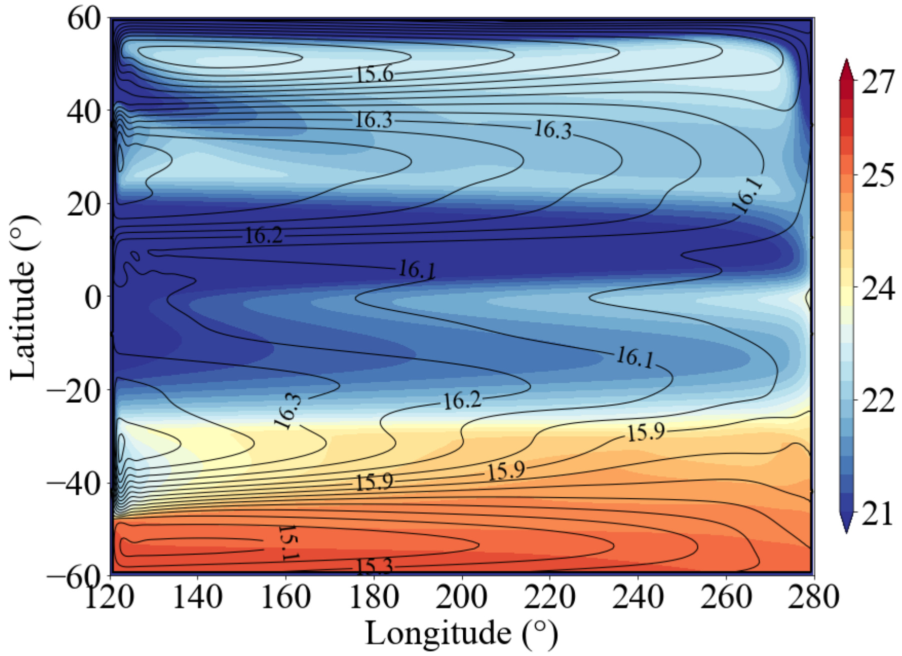

Fig. 3.20 Sea surface density and sea surface height for experiment III.

The color shade shows the sea surface density and the contour lines represent the sea surface height.

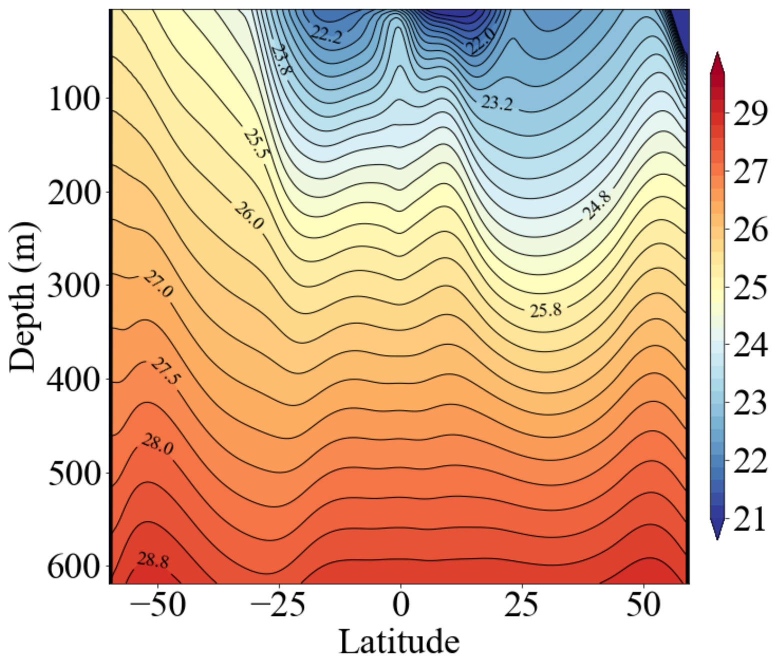

Fig. 3.21 Density along the 240°E meridional section for experiment III.

The color shade and contour lines show the potential density.

The thermal structure anomaly along the equatorial plane (Fig. 3.22) highlights more pronounced differences between experiment III and experiment I compared to those between experiment II and I. A decrease in temperature is observed in the upper layers (a depth of 150 m and above) of the western equatorial Pacific, and it extends eastward. However, the temperature of subsurface water in the western equatorial region, particularly at the depth of 200−600 m, shows an increase of more than 0.5°C, which is greater than that in the comparison between the experiment II and I. This subsurface warming extends eastward and upwells in the eastern equatorial region, contributing to the warming of both the upper and subsurface layers of the eastern equatorial Pacific. As a result, the cold tongue is significantly influenced. These findings suggest that substantial FWD caused by the CIS collapse in the northeastern subpolar gyre can provide complex effects on the thermal structure at the equator.

The thermal structure anomaly along the meridional section at 240°E was also analyzed by comparing the Experiment III with Experiment I, as shown in Fig. 3.23. In the North Pacific, subsurface temperatures at depths of 200–400 m increase by more than 1°C in the northern region of the subtropical gyre and equatorial region, while temperatures in the subtropical gyre decrease. Notably, the temperature in low-latitude areas of the South Pacific exhibits a significant increase, which appears to contribute to the warming observed in the equatorial region.

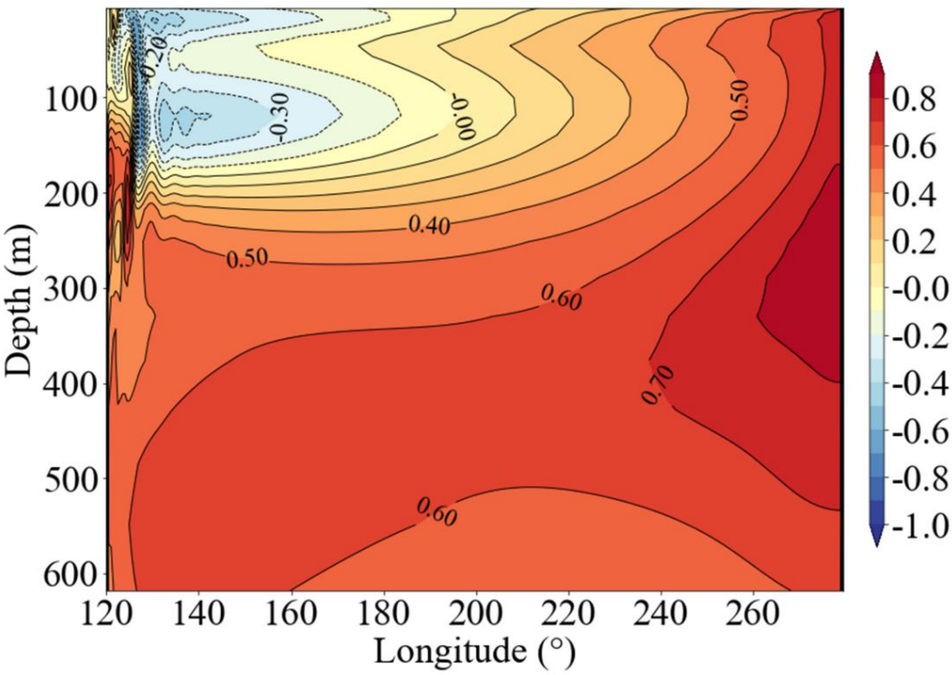

Fig. 3.22 Thermal structure anomaly along the equatorial plane between the experiment III and experiment I.

The color shade and contour lines show the difference of the potential temperature between experiment III and experiment I.

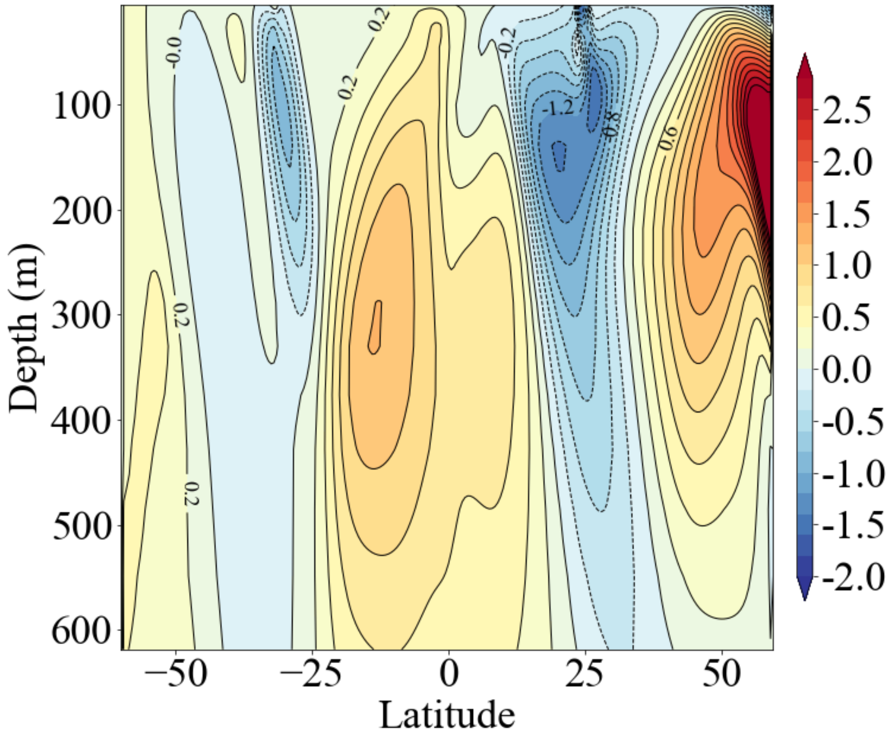

Fig. 3.23 Thermal structure anomaly along the 240°E meridional section between the experiment III and experiment I.

The color shade and contour lines show the difference of the potential temperature between experiment III and experiment I.

3.3.3 Variations in SST gradient and equatorial thermocline depth

The mean east-west SST gradient along the equator plays a significant role in shaping tropical and global climate conditions, such as the phenomena like the El Niño-Southern Oscillation. The SST gradient is defined as the difference in SST anomalies between the equatorial eastern Pacific Ocean (5°S–5°N, 180°–80°W) and the equatorial western Pacific Ocean (5°S–5°N, 110°E–180°) (Watanabe et al., 2021). I calculated the mean SST specifically within the region of 5°S–5°N and 120°E–180°, which corresponds to the equatorial western Pacific of the model domain in this study. Notably, the SST gradient along the equator weakens as the FWD increases (Fig. 3.24). This finding suggests that increasing FWD can contribute to a reduction in the east-west SST gradient, which, in turn, can influence large-scale atmospheric and oceanic circulation patterns.

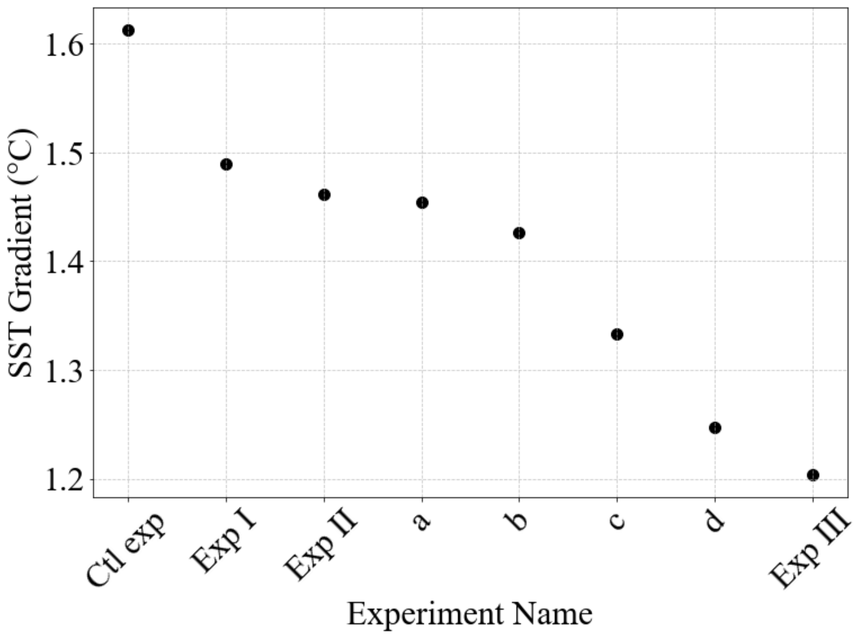

Fig. 3.24 Changes in the equatorial east–west surface temperature gradient.

The experiments of a, b, c, d is forced by 4, 10, 30, 50 m/yr FWD from the CIS collapse. The related results and discussion of Control experiment (Ctl exp) and experiment I, II, III (Exp I, Exp II, and Exp III) are highlighted in this study.

The depth of 20° isotherm is commonly used as the mean depth of thermocline (MDT) in the equatorial Pacific (Chepurin et al., 2005; Kessler, 1990; Yang and Wang, 2009), as it lies near the center of the main thermocline. In this study, the MDT is calculated by averaging the depth of the 20°C isotherm along the equator. The MDT is found to deepen as FWD increases (Fig. 3.25), which is consistent with findings from previous study (Fedorov et al., 2004). According to Fedorov et al. (2004), increasing low-salinity water is symmetrically restored to SSS in the high-latitude subtropical gyres of both hemispheres, which leads to a deepening of the equatorial thermocline. Building on this finding, my study advances the understanding of FWD dynamics by introducing an asymmetric treatment of freshwater input without restoring SSS. This treatment, which accounts for evaporation, precipitation, and FWD from surrounding continents, better represents real-world conditions and highlights previously unrecognized hemispheric differences in equatorial thermocline responses. Specifically, as I discussed in the next section, the present study reveals that water transported form the North Pacific likely contributes to the cooling in the upper layers of the equatorial region, while water from the South Pacific plays a significant role in warming the equatorial region subsurface water. These results not only align with existing theories but also provide new insights into the hemispheric contributions to equatorial thermocline dynamics under varying freshwater input conditions.

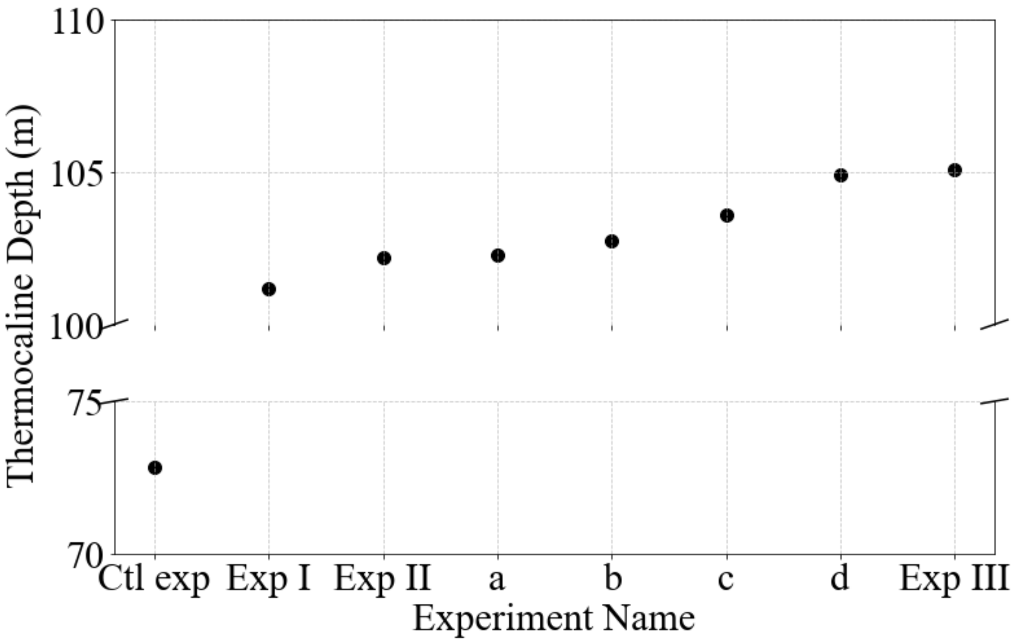

Fig. 3.25 Same as Fig.3.24 but for the changes in the mean depth of the equatorial thermocline as the FWD increases.

3.4 Discussion

3.4.1 Variations in the characteristics along specific isopycnals

Based on the results presented above, water with a σ_θ of 24.5 kg/m^3 is found to lies within the thermocline and upwells in the eastern equatorial Pacific. The isopycnal surface of σ_θ = 24.5 was therefore selected for the control experiment to highlight its various characteristics. The depth distribution of this isopycnal surface varies spatially, which is deep within the subtropical gyres of both hemispheres while shallow in their eastern part, high-latitude boundaries, and the equatorial region (Fig. 3.26). The mixed layer depth is calculated as the depth where the potential density exceeds the surface density by an amount equivalent to cooling the surface water by 0.8 °C ($\Delta\rho = h_{MixCriteria} \times \alpha_{surface}$ with $h_{MixCriteria}$= 0.8; Kara et al., 2000). The isopycnal surface is located within the mixed layer in the northwestern subtropical gyre, suggesting that warm surface water from the western boundary of the subtropical gyre is cooled by the imposed SST as well as by mixing with cold water from the subpolar gyre. This cooling causes the water to subduct into deeper layers and flow on the isopycnal surface, guided by the Montgomery potential (which represents the geostrophic stream function on a density surface). Furthermore, since water primarily flows along isopycnal surfaces, the temperature profile along 240°E on Z-levels (Fig. 3.8) is transformed to an isopycnal representation (Fig. 3.27). In the absence of freshwater forcing, isopycnal depths are predominantly governed by temperature, which remains constant along these levels.

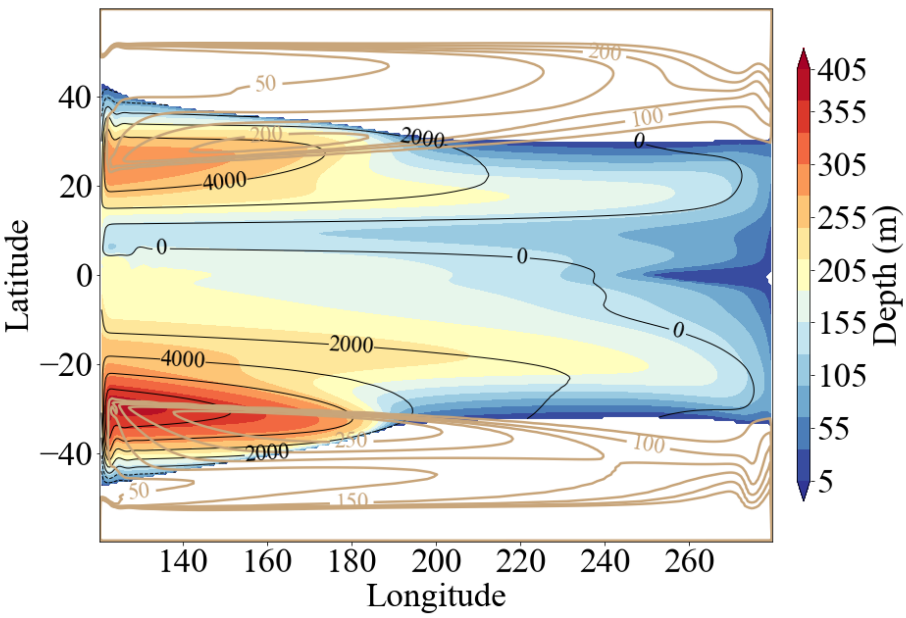

Fig. 3.26 Depth and Montgomery potential distribution along the isopycnal surface (σ_θ = 24.5) and the mixed layer distribution for control experiment.

The color shade shows the depth. Black contour lines represent the Montgomery potential. Bold brown contour lines represent the depth of mixed layer at 50, 100, 150, 200, 250, and 300 m.

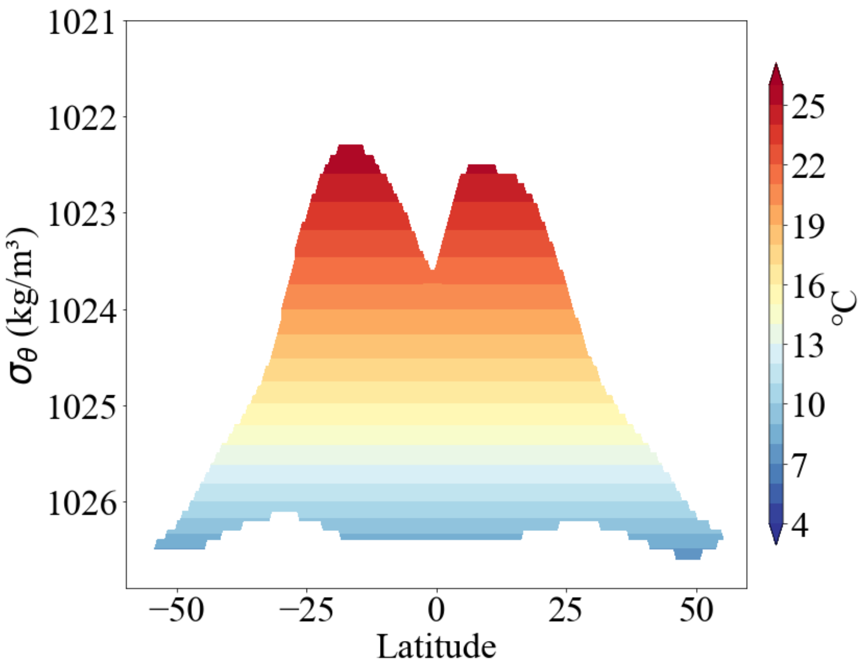

Fig. 3.27 Thermal structure along the 240°E meridional section on isopycnal-levels for control experiment.

The color shade shows the potential temperature for control experiment.

Compared to the control experiment, the South Pacific exhibits a significant intrusion of warm water from the sea surface in the subtropical gyre to the subsurface in the equatorial region along isopycnal surfaces (Fig. 3.28). This process is suggested to be the primary driver of equatorial warming, as shown in Fig. 3.15 of the section 3.3.2.1. In Experiment I, intense evaporation at the sea surface of the South Pacific subtropical gyre increases salinity in this region. As a result, warmer, high-salinity water is transported along the isopycnal surfaces from the South Pacific to the equatorial region. However, water is found to be cooled in the North Pacific, primarily due to the magnitude of E−P (Fig. 3.28). High precipitation across the North Pacific, except in parts of the subtropical gyre, leads to low-salinity water. Subsequently, cold water is transported equatorward from high latitudes along isopycnal surfaces.

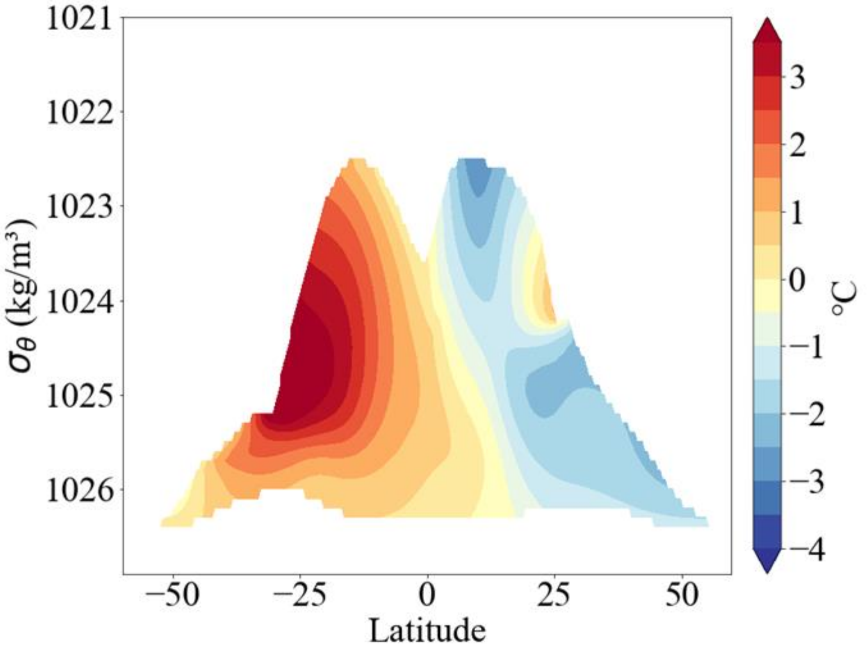

Fig. 3.28 Thermal structure anomaly along the 240°E meridional section on isopycnal-levels between the experiment I and control experiment.

The color shade shows the difference of the potential temperature between the experiment I and control experiment.

Since the cooling and warming effects in Experiment III (Fig. 3.18) are more pronounced than those in Experiment II (Fig. 3.22) in the section 3.3.2.2 and 3.3.2.3, I primarily discuss the possible dynamic mechanisms based on the findings from Experiment III. Under the extreme freshwater input scenario in experiment III, the overall isopycnal surface (σ_θ = 24.5) deepens compared to experiment I, indicating a notable deepening of the equatorial thermocline (Fig. 3.29a, c). Especially, the depth of this isopycnal surface exceeds 200 m across the subtropical gyres and the equatorial region. In the northern subtropical gyre of the North Pacific, isopycnal surface lies in the mixed layer in experiment I. As a result, warm water from the western boundary is able to be cooled due to the imposed SST in this region. The cooled water may subsequently influence the surrounding regions via advection as well as lateral mixing on the isopycnal surface (Fig. 3.29b). While in Experiment III, the isopycnal surface remains below the mixed layer, suggesting that the imposed SST cooling influence is largely suppressed by the isolation effect of the fresh surface water. This mechanism has been discussed by Fedorov et al. (2004). However, the mechanism driving the thermal structure anomaly in experiment III, compared to the case without continental freshwater input (experiment I), differs from that identified in previous studies. In this study, despite the absence of surface heat loss, water originating from the western boundary undergoes significant cooling due to the intrusion of cold water from the subpolar gyre (Fig. 3.29d). As a result, the isopycnal surface in the subpolar and subtropical gyres exhibits substantially lower temperatures than in experiment I (Fig. 3.29b, d). This cooled water is then transported equatorward along the geostrophic flow, contributing to cooling in the equatorial region, particularly in the upper layers of the western equatorial Pacific (Fig. 3.30). Subsequently, the cold water is advected eastward by the equatorial undercurrent, leading to the observed cooling in the upper layers of the equatorial Pacific, as shown above in Fig. 3.22. This cold water transport from the subpolar gyre to the subtropical gyre in the North Pacific is primarily attributed to the advection of substantial low-salinity water from the subpolar gyre, driven by the CIS collapse (Fig. 3.31).

Furthermore, in contrast to Experiment I, Experiment III shows that high-temperature water in the subtropical gyre of the South Pacific significantly warms the subsurface layers of the equatorial region (Fig. 3.29b, d; Fig. 3.30). This warmed water is then transported eastward, affecting both the upper and subsurface thermal structure of the eastern equatorial Pacific. To investigate the thermal structure along isopycnal surfaces, the thermal structure anomaly along the 240°E meridional section between Experiments III and I on Z-levels is transformed into an isopycnal representation (Fig. 3.32). Consistent with the findings on Z-levels, temperature increases in the South Pacific contribute to warming in the equatorial region, while temperature decreases in the subtropical gyre of the North Pacific may induce cooling effects in the equatorial region. The thermal structure anomaly between Experiments III and I can be attributed to two key factors: temperature difference on isopycnal-levels and temperature difference by deepening of isopycnal layers, as illustrated in two panels (Fig. 3.33). Due to the advection of low-salinity water caused by the CIS collapse, cooled water is advected along isopycnals in both hemispheres, with a particularly strong effect in the North Pacific, where low-salinity water advection enhances this cooling process. Additionally, changes in water volume appear to induce a deepening of isopycnal surfaces in both hemispheres, which leads to an overall increase in temperature. These combined processes contribute to the observed thermal anomalies in the equatorial region (Fig. 3.34). The South Pacific primarily experiences a temperature increase, suggesting that isopycnal deepening is the dominant factor driving this warming. This warm water then extends into the equatorial region and slightly north of the equator, with largest increase in subsurface layers approximately 300 m. In contrast, the subtropical gyre of the North Pacific undergoes cooling, primarily driven by the advection of cold water along isopycnal surfaces. This overall structure provides a framework for interpreting thermal structure anomaly between Experiments III and I on Z-levels (Fig. 3.32a).

Thus, the extreme FWD resulting from the CIS collapse into the northeastern boundary induces complex effects on the equatorial thermal structure. It leads to cooling in the upper layers of the western equatorial Pacific, while warming in the whole equatorial Pacific.

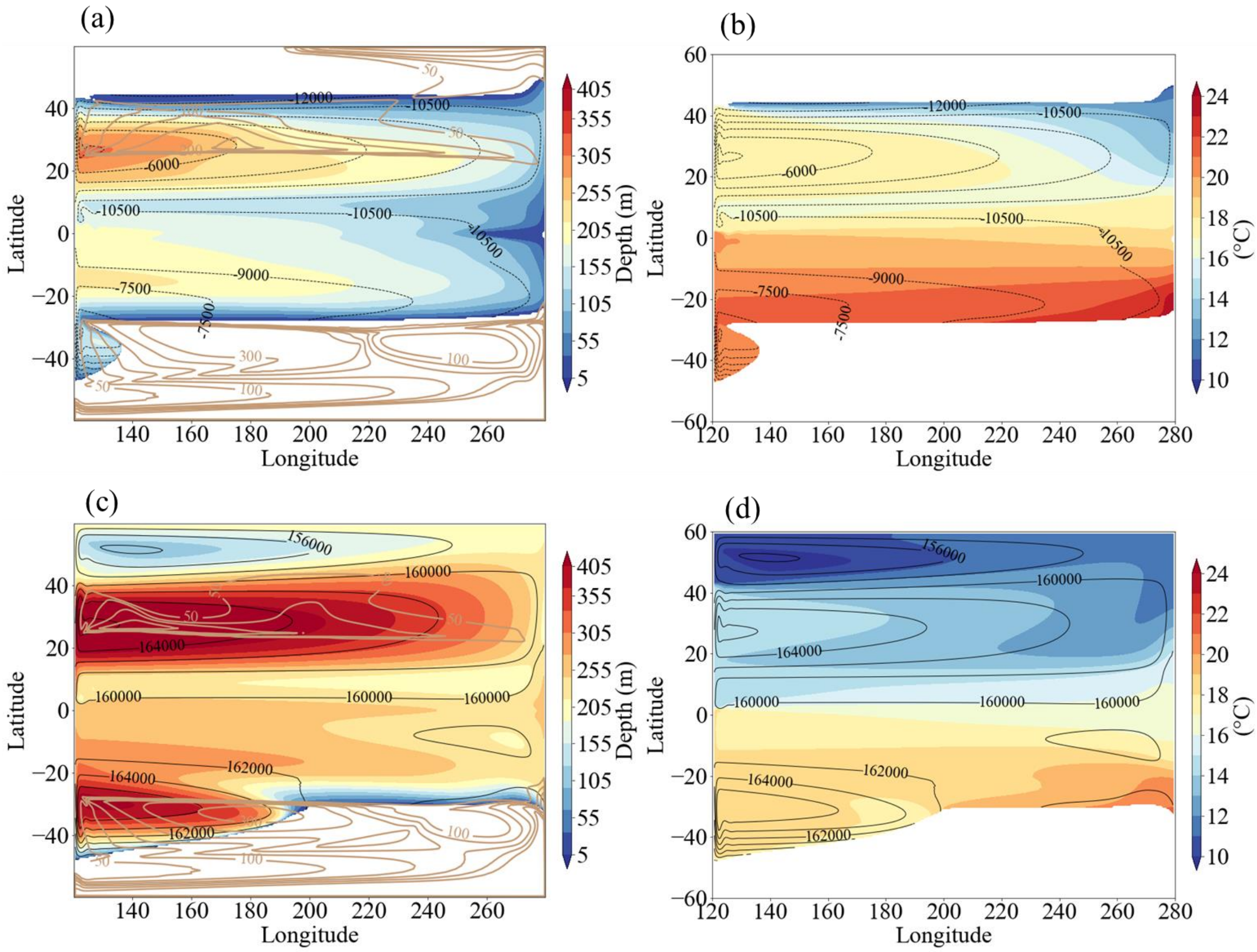

Fig. 3.29 Depth, Montgomery potential, and temperature distribution along the isopycnal surface (σ_θ = 24.5) and the mixed layer distribution for experiment I (a, b) and III (c, d).

For experiment I, (a) The color shade shows the depth. Bold brown contour lines represent the depth of mixed layer at 50, 100, 150, 200, 250, and 300 m. (b) The color shade shows the temperature. For both figures, black contour lines represent the Montgomery potential. (c, d) is same as (a, b), but for experiment III.

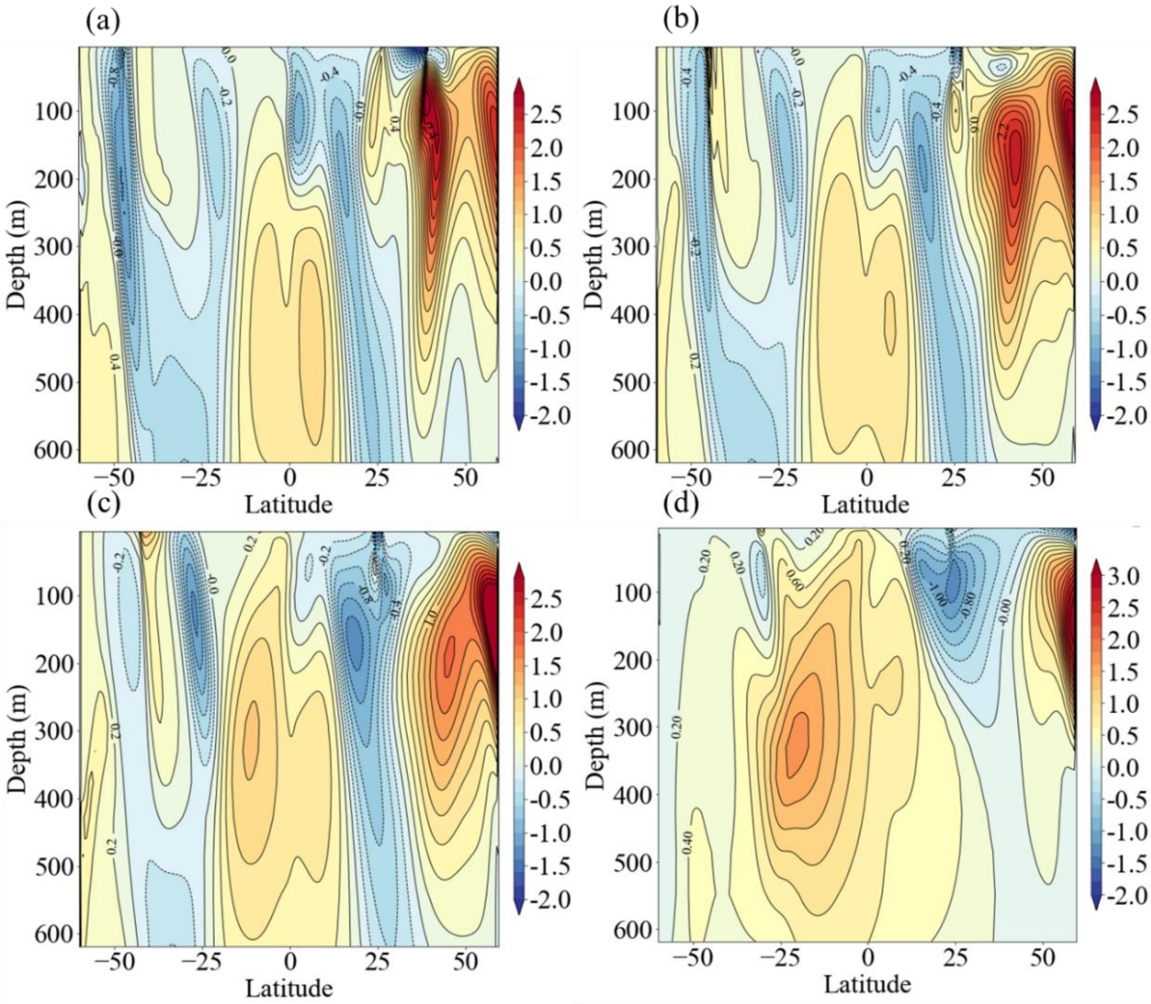

Fig. 3.30 Thermal structure anomaly along meridional section of (a) 150°E, (b) 180°E, (c) 220°E, and (d) 270°E, between the experiment III and I.

The color shade and contour lines show the difference of the potential temperature between experiment III and experiment I.

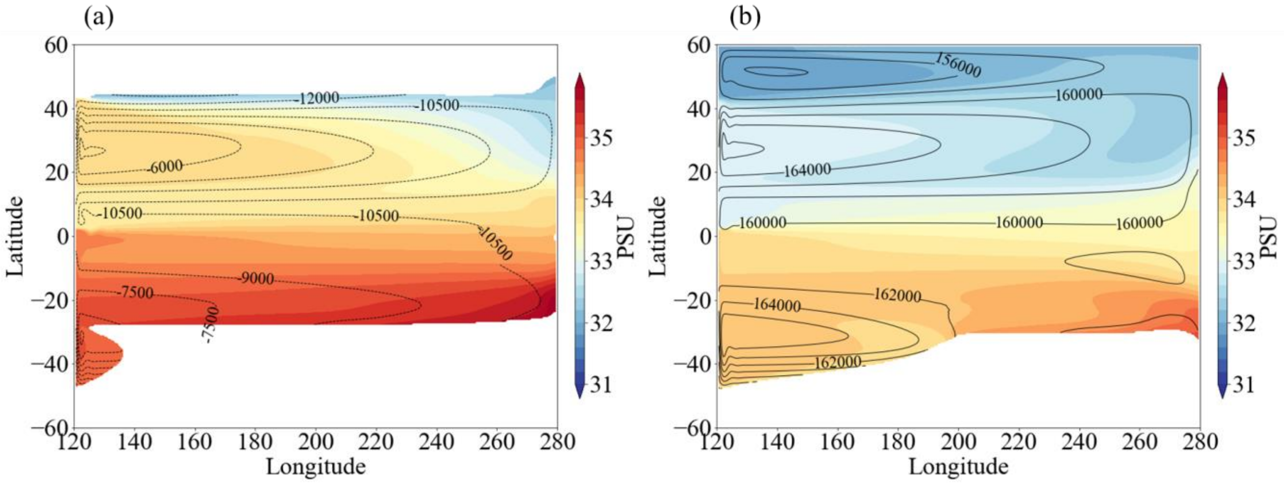

Fig. 3.31 Salinity distribution and Montgomery potential along the isopycnal surface (σ_θ = 24.5) for experiment I (a) and III (b).

The color shade shows the salinity. Black contour lines represent the Montgomery potential.

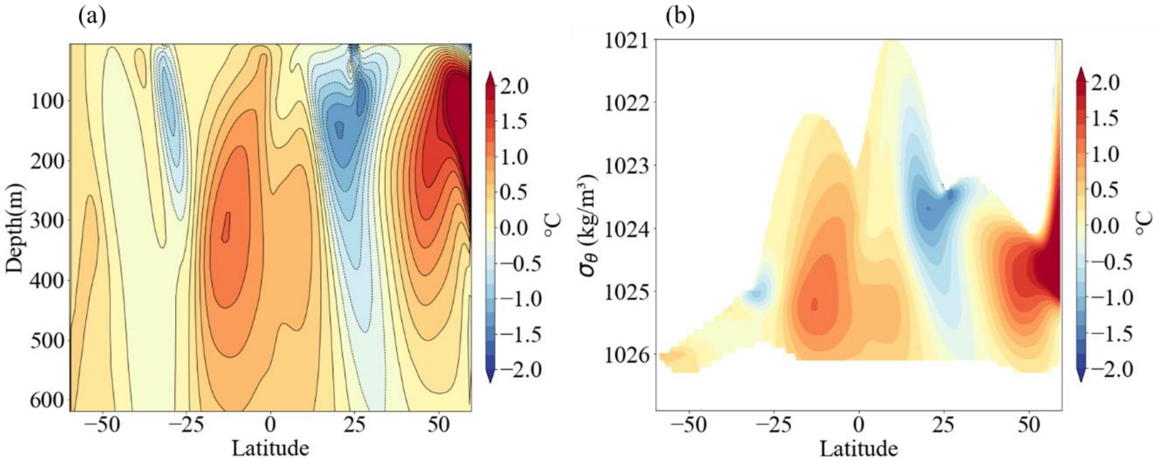

Fig. 3.32 Thermal structure anomaly along the 240°E meridional section between the experiment III and I on Z-levels (a) and isopycnal-levels (b).

The color shade shows the difference of the potential temperature between the experiment III and I.

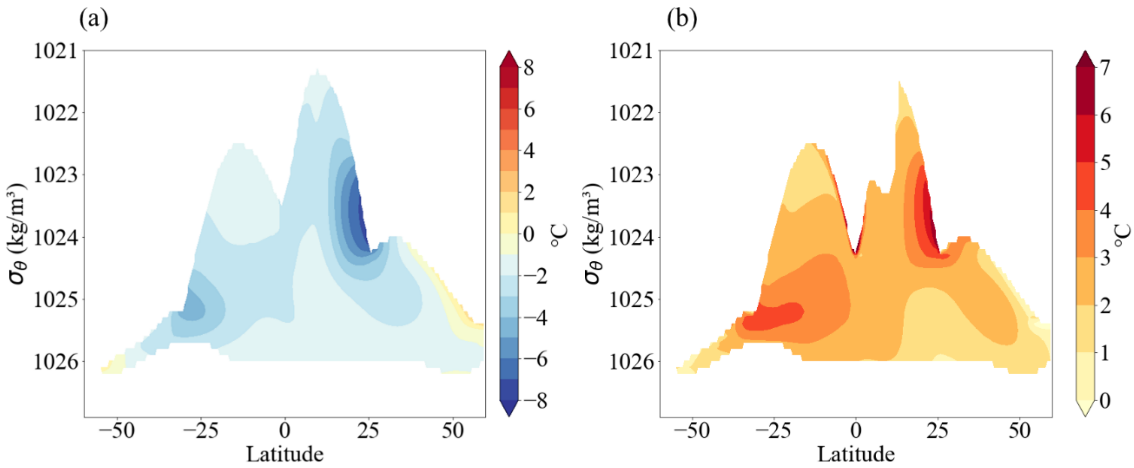

Fig. 3.33 Thermal structure anomaly along the 240°E meridional section on isopycnal-levels (a) and by isopycnals deepening (b).

The color shade shows the difference of the potential temperature between the experiment III and I.

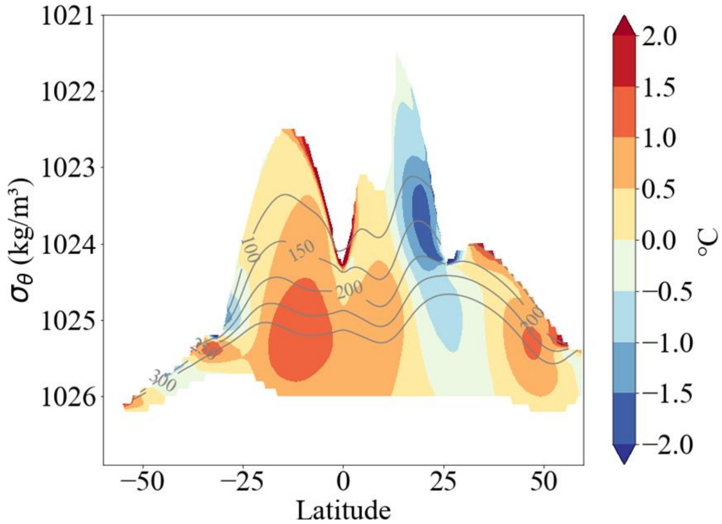

Fig. 3.34 Integration of the two components in Fig. 3.33.

The color shade shows the difference of the potential temperature between the experiment III and I. The contour lines show the average depth of experiment III and I.

3.4.2 Particle tracking for pathway diagnostics

Particle trajectories with depth provide insight into horizontal pathways and vertical movement of water masses. As for the experiment I, the backward trajectory of a sampled particle released in (38°N, 203°E), at the base of the mixed layer, indicates that low-salinity water affected by high precipitation in ITCZ flows toward the northern subtropical region (Fig. 3.35a). The forward trajectory of the sampled particle, which departures from (38°N, 203°E) at the bottom of the mixed layer, indicates that the low-salinity water is advected from northern subtropical gyre to the subtropical gyre and equatorial region (Fig. 3.35b). This low-salinity water advection leads to cooled water intrusion from northern subtropical gyre to the equatorial region (especially, at a depth of approximately 100 m−150 m). Finally, it upwells at the eastern equatorial Pacific, influencing the thermal structure of the equatorial region.

Furthermore, another particle is released in (25°N, 245°E), at the bottom of the mixed layer, for experiment I (Fig. 3.36a, b). The backward and forward trajectories show consistent results and underlying mechanisms with those in Fig. 3.35. However, the particle trajectory in the experiment III indicates an important difference compared to that of the experiment I, such that cold water can be directly transported from the subpolar gyre to the subtropical gyre via Ekman transport (Fig. 3.36a, c), although the particle is released at the same position (25°N, 245°E) as in experiment I. Subsequently, the cold water significantly cools the upper layers (approximately 150 m) of the western equator (Fig. 3.36d).

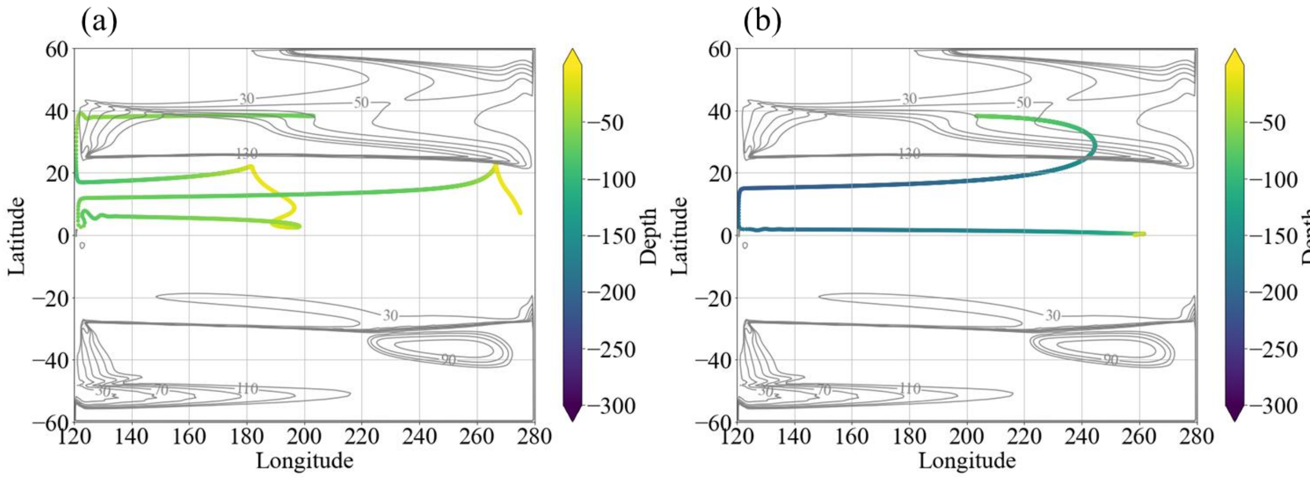

Fig. 3.35 Backward (a) and forward (b) particle trajectories as well as mixed layer distribution for experiment I.

The color represents the depth of the sampled water particle, which departures from (38°N, 203°E) at the bottom of the mixed layer. Light grey contour lines represent the depth of mixed layer at 30, 50, 70, 90, 110, and 130 m.

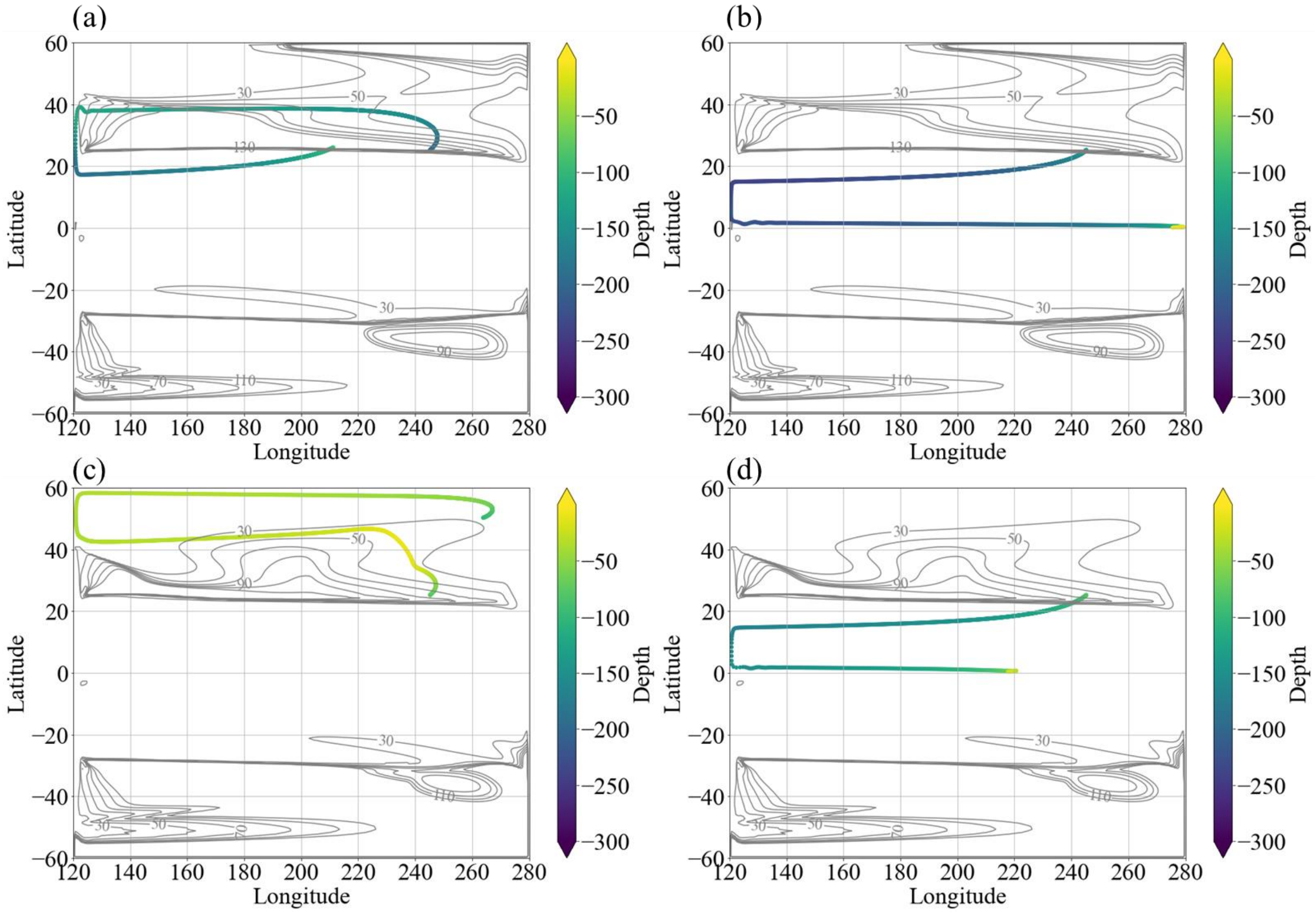

Fig. 3.36 Same as Fig. 3.35, but (a, b) is backward and forward trajectories for experiment I and (c, d) is for experiment III.

The sampled particle is released in (25°N, 245°E), at the bottom of the mixed layer.

A forward particle tracking analysis for experiment III as shown in Fig. 3.37 indicates that particles released from positions (38°N,125°E), (36°N,125°E), (34°N,125°E), (38°N,127°E), (36°N,127°E), (34°N,127°E) at a depth of 125 m in the northwestern subtropical gyre are consistently transported below the mixed layer by Kuroshio waters. This is consistent with the finding of Fedorov et al. (2004), which suggest that warm water is shielded from atmospheric cooling by a surface layer of low-salinity water, thereby contributing to the warming of equatorial subsurface waters. Additionally, some particles remain circulating in the subsurface layers of the subtropical gyre. However, as warm water flows from the northern subtropical gyre toward the equator along the western boundary, it undergoes significant cooling while passing through the colder northern and eastern regions, as discussed in section 3.4.1. This highlights the critical role of water transported from the subpolar gyre of the North Pacific in cooling the thermal structure of the western equatorial Pacific, a process that has not been revealed in previous studies.

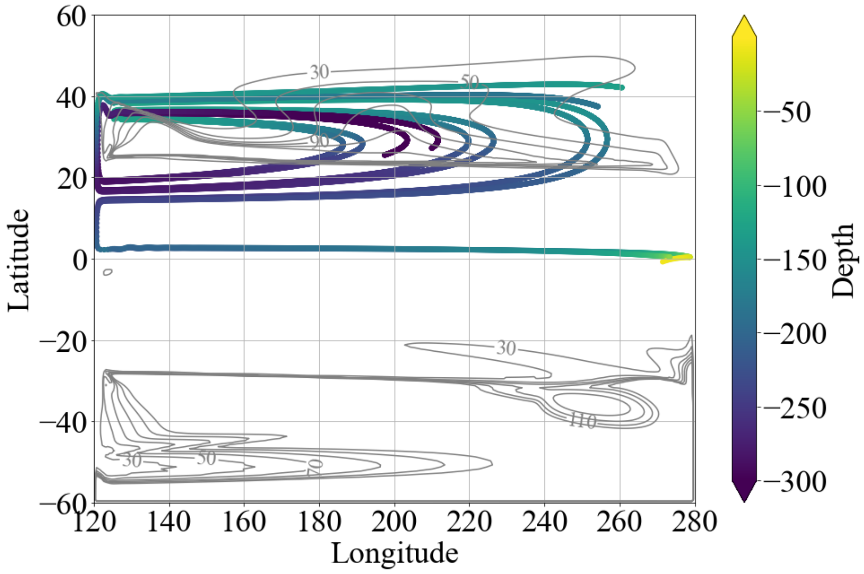

Fig. 3.37 Forward particle trajectories in the North Pacific for the experiment III.

The color represents the depth of sampled water particles, which departure from (38°N,125°E), (36°N,125°E), (34°N,125°E), (38°N,127°E), (36°N,127°E), (34°N,127°E) at the depth of 125 m. Light grey contour lines represent the depth of mixed layer at 30, 50, 70, 90, 110, and 130 m.

The forward particle tracking analysis for Experiment III (Fig. 3.38) reveals that particles released near the base of the mixed layer in the South Pacific subduct rapidly into deeper layers. These particles are then transported along geostrophic flows toward the equator, carrying warm water from the subtropical gyre. Some of this warm water reaches the western equatorial Pacific, while a portion is directly transported to the eastern equatorial Pacific. Additionally, part of the water advected from the western equatorial region eventually upwells in the east. This transport process leads to a temperature increase in the subsurface layers of the equatorial Pacific, highlighting the significant role of South Pacific subtropical water in warming the equatorial thermal structure.

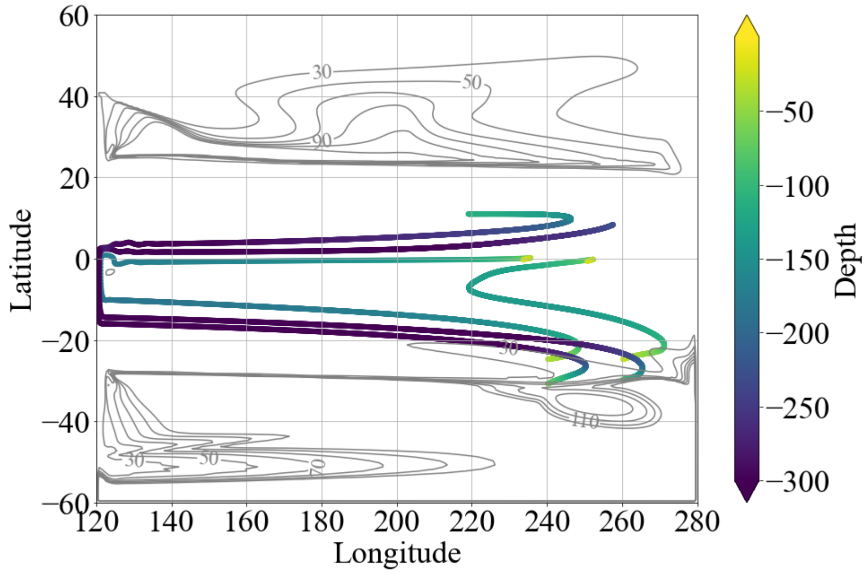

Fig. 3.38 Same as Fig. 3.37, but for sampled particles released at the South Pacific. The sampled water particles departure from (25°S, 240°E), (25°S, 260°E), (31°S, 240°E), and (30°S, 260°E) at the bottom of the mixed layer in Experiment III.

3.5 Conclusions

Using numerical experiments based on the MITgcm, this study investigates the changes in temperature, salinity, and density distributions over various FWD scenarios, offering insights into the mechanisms linking the freshwater input in the subpolar gyre to equatorial thermocline dynamics.

- The control experiment without freshwater confirms that warm water in the subtropical gyres is cooled and subducts into the subsurface. This cooled water flowing along the isopycnal surface reaches the equator and upwells at the eastern equatorial Pacific. The upwelling of this cooled water contributes to an east-west slope of thermocline and supports the formation of the cold tongue, a critical feature for equatorial heat exchange and global climate feedbacks.

- The experiment I indicates that E−P significantly affects SSS and surface density distributions. SSS of the subtropical gyre in the southern hemisphere increases caused by positive E−P. This salinity increase affects subsurface thermal structures through subduction, resulting in a warming at depths of 200–400 m in the equatorial Pacific. In contrast, in the northern hemisphere, SSS of the subpolar gyre exhibits a significant decrease, resulting in cooling effects in the subtropical gyre.
- Incorporating boundary FWD along the northern subpolar gyre in experiment II intensified salinity anomalies and enhanced the southward transport of low-salinity water. This leads to a more pronounced subsurface warming and slight cooling of the upper layers in the equatorial Pacific.
- Experiment III indicates that an extreme FWD scenario driven by the CIS collapse into the northeast Pacific induces substantial changes in oceanic dynamics across both hemispheres. In the North Pacific, the subpolar gyre becomes dominated by low-salinity water, which is transported southward into the subtropical gyre. Corresponding to the salinity redistribution, cold water is significantly transported from the subpolar gyre to the subtropical gyre along the isopycnal surfaces. These processes contribute to a cooling effect in the upper layers of the western equatorial Pacific. However, the South Pacific exhibits low salinity and high temperature in the subtropical gyre, due to the deepening of isopycnal levels. This warm water is transported equatorward, providing warming effects on the equatorial thermocline,

mainly at depths below 200 m of the western equatorial Pacific and across the shallower eastern equatorial region.

Under increasing FWD, the east-west SST gradient along the equator weakened, associated with the deepening of the equatorial thermocline. This SST gradient and the depth of equatorial thermocline are the critical drivers of equatorial Pacific climate phenomena, such as the El Niño. The findings suggest that enhanced FWD from high latitudes can influence the thermal structure along the equator, potentially altering regional and global atmospheric circulation patterns.

3.6 Appendix

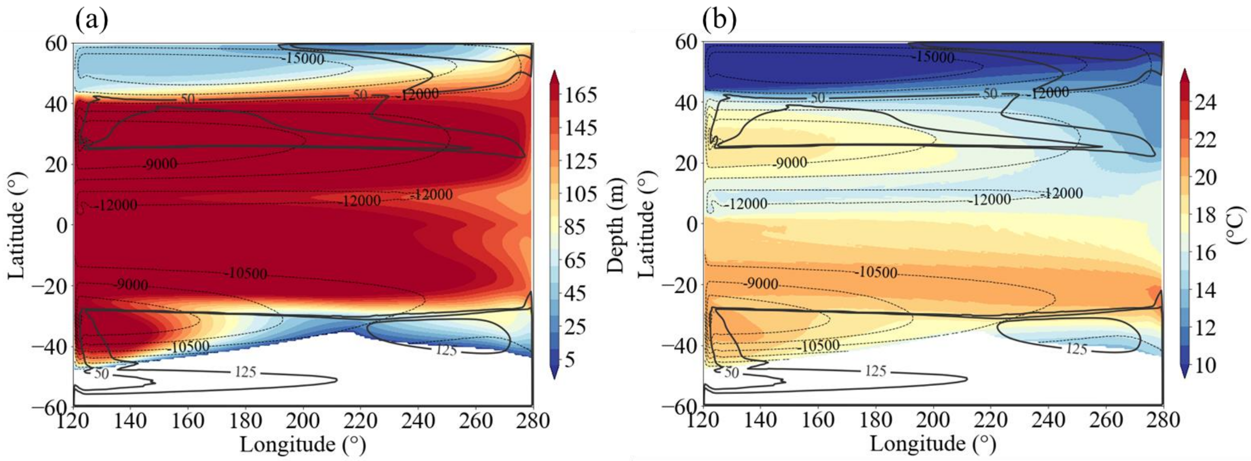

Fig. A3.1 (a) Depth distribution and (b) temperature along the isopycnal surface (σ_θ = 25.5; shaded) for experiment I, respectively. Black contour lines represent the Montgomery potential. Bold dark grey contour lines represent the depth of mixed layer at 50 and 125 m.

Chapter 4 General conclusions

This study provides a comprehensive investigation into the freshwater discharge from the Alaska region, termed Alaska discharge, in basin scales, and its cascading impacts on oceanic processes. The research is divided into two parts: the first focuses on accurately estimating the Alaska discharge and its effects on the Alaskan Stream, while the second explores how freshwater discharge from the Alaska region into the subpolar gyre affects the equatorial thermocline. In the second part, I also explore the effects of an extreme FWD from the CIS collapse into the northeast Pacific on the subtropical and equatorial thermocline.

As the schematic shows (Fig. 4.1), in the first part, the Alaska discharge for 1982–2022 is estimated using the Soil and Water Assessment Tool (SWAT), with modifications to account for melting processes. The results indicate an annual average discharge of 14,396 ± 819 $m^3 \cdot s^{-1}$, with meltwater contributing approximately 53%. The discharge exhibits strong seasonal variation, peaking in June due to snow and ice melting, and maintaining baseflow levels in winter. The interannual variation correlates significantly with SSS anomalies in the Alaskan Stream, suggesting that Alaska discharge influences salinity dynamics in this upstream component of the North Pacific salt pathway. The decadal variations in Alaska discharge show a correlation with the NPGO index, highlighting the role of atmospheric phenomena NPO in driving long-term discharge variability. These findings demonstrate that freshwater discharge from Alaska is not only a critical component of local hydrology but also significantly impacts SSS anomalies, which may propagate downstream and influence ocean circulation in the North Pacific sector.

The second part of this study uses numerical experiments with the MITgcm to explore the effects of freshwater discharge from the subpolar gyre on the equatorial thermocline. The control experiment, without freshwater forcing, shows that warm water in the subtropical gyres is cooled and subducted into the subsurface, flowing along isopycnal surfaces toward the equator and upwelling in the eastern equatorial Pacific. This process supports the east-west slope of the thermocline and the formation of the cold tongue, which plays a critical role in equatorial heat exchange and climate feedbacks. Under freshwater forcing scenarios, including those driven by E−P and boundary freshwater discharge, significant changes in salinity and temperature are observed. Freshening in the subpolar gyres intensifies salinity anomalies, which propagate downstream to the subtropical gyre of the North Pacific, leading to cooling effects at the equator. In contrast, in the South Pacific, high evaporation in the subtropical gyre significantly influences subsurface thermal structures, resulting in warming mainly at depths of 200–400 m in the equatorial Pacific. In extreme freshwater scenarios, caused by the collapse of the CIS, the subpolar gyre in the North Pacific becomes dominated by low-salinity water, which is transported southward into the subtropical gyre. This redistribution of salinity in the North Pacific enhances the cooling of upper layers in the western equatorial Pacific. In contrast, warming effects dominate in the equatorial thermocline driven mainly by water from the South Pacific. This warming is attributed to the deepening of isopycnal levels, which leads to the equatorward transport of warm, low-salinity water. The study further reveals that increased freshwater input weakens the east-west SST gradient and deepens the equatorial thermocline, creating an El Niño-like state. These findings suggest that freshwater discharge from high latitudes of the subpolar gyre can significantly influence equatorial thermocline dynamics and, consequently, the regional and global climate systems.

In summary, this study provides an accurate estimation of the Alaska discharge and highlights its role in driving salinity anomalies in the Alaskan Stream. Furthermore, it uncovers the cascading impacts of freshwater fluxes from the subpolar gyre on the equatorial thermocline, offering critical insights into the connections between high-latitude processes, ocean circulation, and equatorial climate variability.

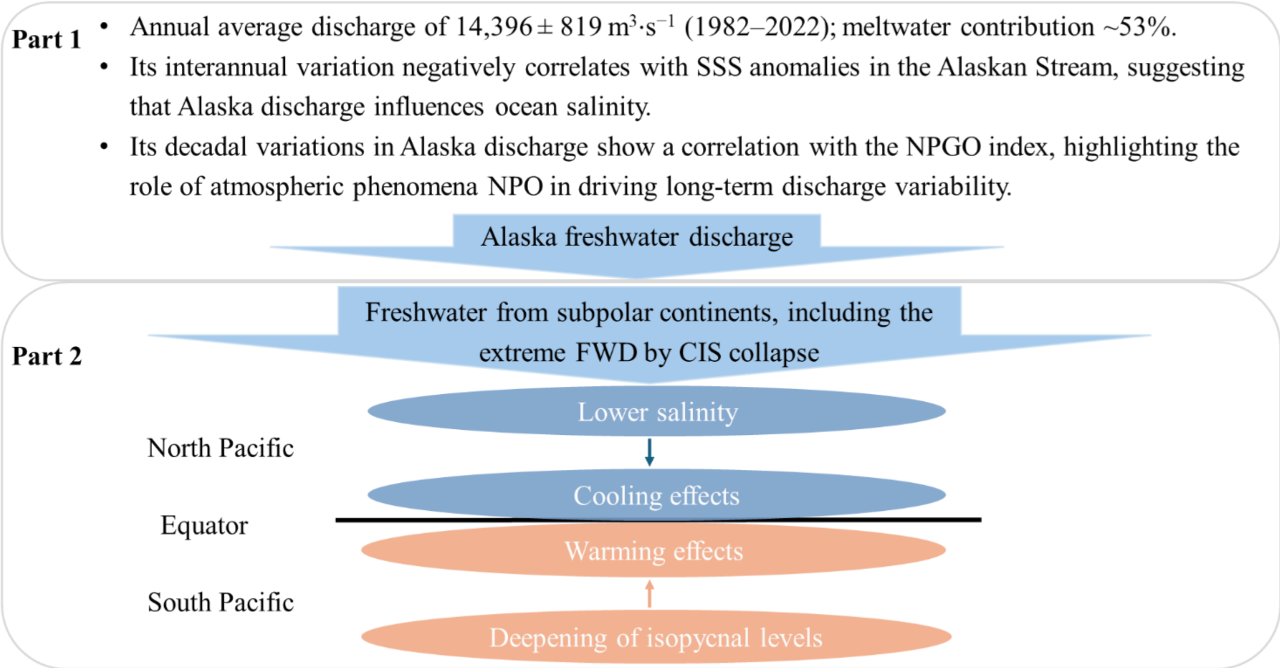

Fig. 4.1 Schematic of thesis main structure.

Reference

Abbaspour, K.C., Yang, J., Maximov, I., Siber, R., Bogner, K., Mieleitner, J., Zobrist, J., Srinivasan, R., 2007. Modelling hydrology and water quality in the pre-alpine/alpine Thur watershed using SWAT. Journal of Hydrology 333, 413–430. https://doi.org/10.1016/j.jhydrol.2006.09.014

Ahmed, M.I., Stadnyk, T., Pietroniro, A., Awoye, H., Bajracharya, A., Mai, J., Tolson, B.A., Shen, H., Craig, J.R., Gervais, M., Sagan, K., Wruth, S., Koenig, K., Lilhare, R., Déry, S.J., Pokorny, S., Venema, H., Muhammad, A., Taheri, M., 2023. Learning from hydrological models' challenges: A case study from the Nelson basin model intercomparison project. Journal of Hydrology 623, 129820. https://doi.org/10.1016/j.jhydrol.2023.129820

Allen, R.G., Jensen, M.E., Wright, J.L., Burman, R.D., 1989. Operational Estimates of Reference Evapotranspiration. Agronomy Journal 81, 650–662. https://doi.org/10.2134/agronj1989.00021962008100040019x

Andrianaki, M., Shrestha, J., Kobierska, F., Nikolaidis, N.P., Bernasconi, S.M., 2019. Assessment of SWAT spatial and temporal transferability for a high-altitude glacierized catchment. Hydrology and Earth System Sciences 23, 3219–3232. https://doi.org/10.5194/hess-23-3219-2019

Anees, M.T., Abdullah, K., Nawawi, M.N.M., Ab Rahman, N.N.N., Piah, Abd.R.Mt., Zakaria, N.A., Syakir, M.I., Mohd. Omar, A.K., 2016. Numerical modeling techniques for flood analysis. Journal of African Earth Sciences 124, 478–486. https://doi.org/10.1016/j.jafrearsci.2016.10.001

Arnold, J.G., Srinivasan, R., Muttiah, R.S., Williams, J.R., 1998. Large Area Hydrologic Modeling and Assessment Part I: Model Development1. JAWRA Journal of the American Water Resources Association 34, 73–89. https://doi.org/10.1111/j.1752-1688.1998.tb05961.x

Ballinger, T.J., Bhatt, U.S., Bieniek, P.A., Brettschneider, B., Lader, R.T., Littell, J.S., Thoman, R.L., Waigl, C.F., Walsh, J.E., Webster, M.A., 2023. Alaska Terrestrial and Marine Climate Trends, 1957–2021. Journal of Climate 36, 4375–4391. https://doi.org/10.1175/JCLI-D-22-0434.1

Bárdossy, A., 2007. Calibration of hydrological model parameters for ungauged catchments. Hydrology and Earth System Sciences 11, 703–710. https://doi.org/10.5194/hess-11-703-2007

Beamer, J.P., Hill, D.F., Arendt, A., Liston, G.E., 2016. High-resolution modeling of coastal freshwater discharge and glacier mass balance in the Gulf of Alaska watershed. Water Resources Research 52, 3888–3909. https://doi.org/10.1002/2015WR018457

Beck, H.E., Zimmermann, N.E., McVicar, T.R., Vergopolan, N., Berg, A., Wood, E.F., 2018. Present and future Köppen-Geiger climate classification maps at 1-km resolution. Sci Data 5, 180214. https://doi.org/10.1038/sdata.2018.214

Bieniek, P.A., Bhatt, U.S., Thoman, R.L., Angeloff, H., Partain, J., Papineau, J., Fritsch, F., Holloway, E., Walsh, J.E., Daly, C., Shulski, M., Hufford, G., Hill, D.F., Calos, S., Gens, R., 2012. Climate Divisions for Alaska Based on Objective Methods. Journal of Applied Meteorology and Climatology 51, 1276–1289. https://doi.org/10.1175/JAMC-D-11-0168.1

Biswas, T., Walterman, M., Maus, P., Megown, K.A., Healey, S.P., Brewer, K., 2012. Assessment of land use change in the coterminous United States and Alaska for global assessment of forest loss conducted by the food and agricultural organization of the United Nations. In: Morin, Randall S.; Liknes, Greg C., comps. Moving from status to trends: Forest Inventory and Analysis (FIA) symposium 2012; 2012 December 4-6; Baltimore, MD. Gen. Tech. Rep. NRS-P-105. Newtown Square, PA: U.S. Department of Agriculture, Forest Service, Northern Research Station. [CD-ROM]: 37-45. 37–45.
Chepurin, G.A., Carton, J.A., Dee, D., 2005. Forecast Model Bias Correction in Ocean Data Assimilation. https://doi.org/10.1175/MWR2920.1
Cloern, J.E., Alpine, A.E., Cole, B.E., Wong, R.L.J., Arthur, J.F., Ball, M.D., 1983. River discharge controls phytoplankton dynamics in the northern San Francisco Bay estuary. Estuarine, Coastal and Shelf Science 16, 415–429. https://doi.org/10.1016/0272-7714(83)90103-8
Cogley, J.G., Hock, R., Rasmussen, L.A., Arendt, A.A., Bauder, A., Braithwaite, R.J., Jansson, P., Kaser, G., Möller, M., Nicholson, L., Zemp, M., 2011. Glossary of glacier mass balance and related terms. IHP-VII Technical Documents in Hydrology 86. https://doi.org/10.5167/uzh-53475
Commission for Environmental Cooperation (CEC). 2020., n.d. “2015 Land Cover of North America at 30 Meters”. Canada Centre for Remote Sensing (CCRS)/Canada Centre for Mapping and Earth Observation (CCMEO), Natural Resources Canada (NRCan), U.S. Geological Survey (USGS), Comisión Nacional para el Conocimiento y Uso de la Biodiversidad (CONABIO), Comisión Nacional Forestal (CONAFOR), Instituto Nacional de Estadística y Geografía (INEGI). Ed. 2.0, Raster digital data [30-m]. [WWW Document]. Commission for Environmental Cooperation. URL http://www.cec.org/nalcms
D’Agnese, F., Faunt, C., Turner, A., 1996. Using remote sensing and GIS techniques to estimate discharge and recharge fluxes for the Death Valley regional groundwater flow system, USA.
Dai, A., Trenberth, K.E., 2002. Estimates of Freshwater Discharge from Continents: Latitudinal and Seasonal Variations. Journal of Hydrometeorology 3, 660–687. https://doi.org/10.1175/1525-7541(2002)003<0660:EOFDFC>2.0.CO;2
Di Lorenzo, E., Fiechter, J., Schneider, N., Bracco, A., Miller, A.J., Franks, P.J.S., Bograd, S.J., Moore, A.M., Thomas, A.C., Crawford, W., Peña, A., Hermann, A.J., 2009. Nutrient and salinity decadal variations in the central and eastern North Pacific. Geophysical Research Letters 36. https://doi.org/10.1029/2009GL038261
Di Lorenzo, E., Schneider, N., Cobb, K.M., Franks, P.J.S., Chhak, K., Miller, A.J., McWilliams, J.C., Bograd, S.J., Arango, H., Curchitser, E., Powell, T.M., Rivière, P., 2008. North Pacific Gyre Oscillation links ocean climate and ecosystem change. Geophysical Research Letters 35. https://doi.org/10.1029/2007GL032838
Dobriyal, P., Badola, R., Tuboi, C., Hussain, S.A., 2017. A review of methods for monitoring streamflow for sustainable water resource management. Appl Water Sci 7, 2617–2628. https://doi.org/10.1007/s13201-016-0488-y
Durack, P.J., 2015. Ocean Salinity and the Global Water Cycle. Oceanography 28, 20–31.

FAO-UNESCO Soil Map of the World 1:5000000, 1974. Prepared by the Food and Agriculture Organization of the United Nations,. Unesco, Paris.
Fedorov, A.V., Pacanowski, R.C., Philander, S.G., Boccaletti, G., 2004. The Effect of Salinity on the Wind-Driven Circulation and the Thermal Structure of the Upper Ocean.
Fiedler, P.C., 2010. Comparison of objective descriptions of the thermocline. Limnology and Oceanography: Methods 8, 313–325. https://doi.org/10.4319/lom.2010.8.313
Fontaine, T., Cruickshank, T., Arnold, J., Hotchkiss, R., 2002. Development of a Snowfall-Snowmelt Routine for Mountainous Terrain for the Soil Water Assessment Tool (SWAT). Journal of Hydrology 262, 209–223. https://doi.org/10.1016/S0022-1694(02)00029-X
Fujisaki, A., Mitsudera, H., Wang, J., Wakatsuchi, M., 2014. How does the Amur River discharge flow over the northwestern continental shelf in the Sea of Okhotsk? Progress in Oceanography, Biogeochemical and physical processes in the Sea of Okhotsk and the linkages to the Pacific Ocean 126, 8–20. https://doi.org/10.1016/j.pocean.2014.04.028
Gleason, C.J., Durand, M.T., 2020. Remote Sensing of River Discharge: A Review and a Framing for the Discipline. Remote Sensing 12, 1107. https://doi.org/10.3390/rs12071107
Grusson, Y., Sun, X., Gascoin, S., Sauvage, S., Raghavan, S., Anctil, F., Sáchez-Pérez, J.-M., 2015. Assessing the capability of the SWAT model to simulate snow, snow melt and streamflow dynamics over an alpine watershed. Journal of Hydrology 531, 574–588. https://doi.org/10.1016/j.jhydrol.2015.10.070
Hill, D.F., Bruhis, N., Calos, S.E., Arendt, A., Beamer, J., 2015. Spatial and temporal variability of freshwater discharge into the Gulf of Alaska. Journal of Geophysical Research: Oceans 120, 634–646. https://doi.org/10.1002/2014JC010395
Huang, R.X., Pedlosky, J., 2000. Climate Variability of the Equatorial Thermocline Inferred from a Two-Moving-Layer Model of the Ventilated Thermocline.
Itoh, M., Ohshima, K.I., Wakatsuchi, M., 2003. Distribution and formation of Okhotsk Sea Intermediate Water: An analysis of isopycnal climatological data. Journal of Geophysical Research: Oceans 108. https://doi.org/10.1029/2002JC001590
J. G. Arnold, D. N. Moriasi, P. W. Gassman, K. C. Abbaspour, M. J. White, R. Srinivasan, C. Santhi, R. D. Harmel, A. van Griensven, M. W. Van Liew, N. Kannan, M. K. Jha, 2012. SWAT: Model Use, Calibration, and Validation. Transactions of the ASABE 55, 1491–1508. https://doi.org/10.13031/2013.42256
Jarosz, E., Wang, D., Wijesekera, H., Scott Pegau, W., Moum, J.N., 2017. Flow variability within the Alaska Coastal Current in winter. Journal of Geophysical Research: Oceans 122, 3884–3906. https://doi.org/10.1002/2016JC012102
Jimmy R. Williams, 1969. Flood Routing With Variable Travel Time or Variable Storage Coefficients. Transactions of the ASAE 12, 0100–0103. https://doi.org/10.13031/2013.38772
Kara, A.B., Rochford, P.A., Hurlburt, H.E., 2000. Mixed layer depth variability and barrier layer formation over the North Pacific Ocean. Journal of Geophysical Research: Oceans 105, 16783–16801. https://doi.org/10.1029/2000JC900071

Kendall, M.G., 1948. Rank Correlation Methods. C. Griffin.
Kessler, W.S., 1990. Observations of long Rossby waves in the northern tropical Pacific. Journal of Geophysical Research: Oceans 95, 5183–5217. https://doi.org/10.1029/JC095iC04p05183
Kottek, M., Grieser, J., Beck, C., Rudolf, B., Rubel, F., 2006. World Map of the Köppen-Geiger climate classification updated. metz 15, 259–263. https://doi.org/10.1127/0941-2948/2006/0130
Kunkel, K.E., Stevens, L.E., Stevens, S.E., Sun, L., Janssen, E., Wuebbles, D., Hilberg, S.D., Timlin, M.S., Stoecker, L., Westcott, N., Dobson, J.G., 2013. Regional Climate Trends and Scenarios for the U.S. National Climate Assessment Part 3. Climate of the Midwest U.S. NOAA Technical Report NESDIS 142-3.
Lader, R., Bhatt, U.S., Walsh, J.E., Rupp, T.S., Bieniek, P.A., 2016. Two-Meter Temperature and Precipitation from Atmospheric Reanalysis Evaluated for Alaska. https://doi.org/10.1175/JAMC-D-15-0162.1
Lehmann, A., Myrberg, K., Post, P., Chubarenko, I., Dailidiene, I., Hinrichsen, H.-H., Hüssy, K., Liblik, T., Meier, H.E.M., Lips, U., Bukanova, T., 2022. Salinity dynamics of the Baltic Sea. Earth System Dynamics 13, 373–392. https://doi.org/10.5194/esd-13-373-2022
Linkin, M.E., Nigam, S., 2008. The North Pacific Oscillation–West Pacific Teleconnection Pattern: Mature-Phase Structure and Winter Impacts. Journal of Climate 21, 1979–1997. https://doi.org/10.1175/2007JCLI2048.1
Lu, P., McCreary, J.P., Klinger, B.A., 1998. Meridional Circulation Cells and the Source Waters of the Pacific Equatorial Undercurrent.
Mann, H.B., 1945. Nonparametric Tests Against Trend. Econometrica 13, 245–259. https://doi.org/10.2307/1907187
Marshall, J., Adcroft, A., Hill, C., Perelman, L., Heisey, C., 1997. A finite-volume, incompressible Navier Stokes model for studies of the ocean on parallel computers. Journal of Geophysical Research: Oceans 102, 5753–5766. https://doi.org/10.1029/96JC02775
Masotti, I., Aparicio-Rizzo, P., Yevenes, M.A., Garreaud, R., Belmar, L., Farías, L., 2018. The Influence of River Discharge on Nutrient Export and Phytoplankton Biomass Off the Central Chile Coast (33°–37°S): Seasonal Cycle and Interannual Variability. Frontiers in Marine Science 5.
Maxwell, R.M., Putti, M., Meyerhoff, S., Delfs, J.-O., Ferguson, I.M., Ivanov, V., Kim, J., Kolditz, O., Kollet, S.J., Kumar, M., Lopez, S., Niu, J., Paniconi, C., Park, Y.-J., Phanikumar, M.S., Shen, C., Sudicky, E.A., Sulis, M., 2014. Surface-subsurface model intercomparison: A first set of benchmark results to diagnose integrated hydrology and feedbacks. Water Resources Research 50, 1531–1549. https://doi.org/10.1002/2013WR013725
Mengistu, A.G., van Rensburg, L.D., Woyessa, Y.E., 2019. Techniques for calibration and validation of SWAT model in data scarce arid and semi-arid catchments in South Africa. Journal of Hydrology: Regional Studies 25, 100621. https://doi.org/10.1016/j.ejrh.2019.100621
Menounos, B., Goehring, B.M., Osborn, G., Margold, M., Ward, B., Bond, J., Clarke, G.K.C., Clague, J.J., Lakeman, T., Koch, J., Caffee, M.W., Gosse, J., Stroeven, A.P., Seguinot, J., Heyman, J., 2017. Cordilleran Ice Sheet mass loss preceded

climate reversals near the Pleistocene Termination. Science 358, 781–784. https://doi.org/10.1126/science.aan3001
Mernild, S.H., Lipscomb, W.H., Bahr, D.B., Radić, V., Zemp, M., 2013. Global glacier changes: a revised assessment of committed mass losses and sampling uncertainties. The Cryosphere 7, 1565–1577. https://doi.org/10.5194/tc-7-1565-2013
Moges, D.M., Virro, H., Kmoch, A., Cibin, R., Rohith, A.N., Martínez-Salvador, A., Conesa-García, C., Uuemaa, E., 2023. How does the choice of DEMs affect catchment hydrological modeling? Science of The Total Environment 892, 164627. https://doi.org/10.1016/j.scitotenv.2023.164627
Montanarella, L., Pennock, D., McKenzie, N., Alavipanah, S.K., Alegre, J., Alshankiti, A., Arrouays, D., Aulakh, M., Badraoui, M., Baptista, I., Black, H., Camps Arbestain, M., Chude, V., Elsheikh, E., Espinosa-Victoria, D., Hempel, J., Henríquez, C., Hong, S.-Y., Krasilnikov, P., Zhang, G.-L., 2015. The Status of the World's Soil Resources (Technical Summary).
Monteith, J.L., 1965. Evaporation and environment. Symposia of the Society for Experimental Biology 19, 205–234.
Moriasi, D., Arnold, J., Van Liew, M., Bingner, R., Harmel, R.D., Veith, T., 2007. Model Evaluation Guidelines for Systematic Quantification of Accuracy in Watershed Simulations. Transactions of the ASABE 50. https://doi.org/10.13031/2013.23153
Nakatsuka, T., Toda, M., Kawamura, K., Wakatsuchi, M., 2004. Dissolved and particulate organic carbon in the Sea of Okhotsk: Transport from continental shelf to ocean interior. Journal of Geophysical Research: Oceans 109. https://doi.org/10.1029/2003JC001909
NASA/METI/AIST/Japan Spacesystems And U.S./Japan ASTER Science Team, n.d. ASTER Global Digital Elevation Model V003, 2019, doi:10.5067/ASTER/ASTGTM.003. https://doi.org/10.5067/ASTER/ASTGTM.003
Neal, E.G., Hood, E., Smikrud, K., 2010. Contribution of glacier runoff to freshwater discharge into the Gulf of Alaska. Geophysical Research Letters 37. https://doi.org/10.1029/2010GL042385
Neitsch, S., Arnold, J., Kinry, J.R., Williams, J.R., 2011. Soil and water assessment tool theoretical documentation. Version.
Neupane, R.P., Adamowski, J.F., White, J.D., Kumar, S., 2017. Future streamflow simulation in a snow-dominated Rocky Mountain headwater catchment. Hydrology Research 49, 1172–1190. https://doi.org/10.2166/nh.2017.024
Nishioka, J., Nakatsuka, T., Watanabe, Y.W., Yasuda, I., Kuma, K., Ogawa, H., Ebuchi, N., Scherbinin, A., Volkov, Y.N., Shiraiwa, T., Wakatsuchi, M., 2013. Intensive mixing along an island chain controls oceanic biogeochemical cycles. Global Biogeochemical Cycles 27, 920–929. https://doi.org/10.1002/gbc.20088
Nonaka, M., McCreary, J.P., Xie, S.-P., 2006. Influence of Midlatitude Winds on the Stratification of the Equatorial Thermocline. https://doi.org/10.1175/JPO2845.1
Ohmura, A., Boettcher, M., 2022. On the Shift of Glacier Equilibrium Line Altitude (ELA) under the Changing Climate. Water 14, 2821. https://doi.org/10.3390/w14182821

Omani, N., Srinivasan, R., Karthikeyan, R., Smith, P.K., 2017a. Hydrological Modeling of Highly Glacierized Basins (Andes, Alps, and Central Asia). Water 9, 111. https://doi.org/10.3390/w9020111

Omani, N., Srinivasan, R., Smith, P.K., Karthikeyan, R., 2017b. Glacier mass balance simulation using SWAT distributed snow algorithm. Hydrological Sciences Journal 62, 546–560. https://doi.org/10.1080/02626667.2016.1162907

Potapov, P., Turubanova, S., Hansen, M.C., Tyukavina, A., Zalles, V., Khan, A., Song, X.-P., Pickens, A., Shen, Q., Cortez, J., 2022. Global maps of cropland extent and change show accelerated cropland expansion in the twenty-first century. Nat Food 3, 19–28. https://doi.org/10.1038/s43016-021-00429-z

Rae, J.W.B., Gray, W.R., Wills, R.C.J., Eisenman, I., Fitzhugh, B., Fotheringham, M., Littley, E.F.M., Rafter, P.A., Rees-Owen, R., Ridgwell, A., Taylor, B., Burke, A., 2020. Overturning circulation, nutrient limitation, and warming in the Glacial North Pacific. Science Advances 6, eabd1654. https://doi.org/10.1126/sciadv.abd1654

Rahmstorf, S., 2003. Thermohaline circulation: The current climate. Nature 421, 699–699. https://doi.org/10.1038/421699a

RGI, n.d. Consortium, 2017. Randolph Glacier Inventory - A Dataset of Global Glacier Outlines, Version 6. [Indicate subset used]. Boulder, Colorado USA. NSIDC: National Snow and Ice Data Center. doi: https://doi.org/10.7265/4m1f-gd79.

Rogers, J.C., 1981. The North Pacific Oscillation. Journal of Climatology 1, 39–57. https://doi.org/10.1002/joc.3370010106

Royer, T., Finney, B., 2020. An Oceanographic Perspective on Early Human Migrations to the Americas. Oceanog 33. https://doi.org/10.5670/oceanog.2020.102

Royer, T.C., Grosch, C.E., Mysak, L.A., 2001. Interdecadal variability of Northeast Pacific coastal freshwater and its implications on biological productivity. Progress in Oceanography, Pacific climate variability and marine ecosystem impacts 49, 95–111. https://doi.org/10.1016/S0079-6611(01)00017-9

Saha, S., Moorthi, S., Pan, H.-L., Wu, X., Wang, Jiande, Nadiga, S., Tripp, P., Kistler, R., Woollen, J., Behringer, D., Liu, H., Stokes, D., Grumbine, R., Gayno, G., Wang, Jun, Hou, Y.-T., Chuang, H., Juang, H.-M.H., Sela, J., Iredell, M., Treadon, R., Kleist, D., Delst, P.V., Keyser, D., Derber, J., Ek, M., Meng, J., Wei, H., Yang, R., Lord, S., Dool, H. van den, Kumar, A., Wang, W., Long, C., Chelliah, M., Xue, Y., Huang, B., Schemm, J.-K., Ebisuzaki, W., Lin, R., Xie, P., Chen, M., Zhou, S., Higgins, W., Zou, C.-Z., Liu, Q., Chen, Y., Han, Y., Cucurull, L., Reynolds, R.W., Rutledge, G., Goldberg, M., 2010. The NCEP Climate Forecast System Reanalysis. https://doi.org/10.1175/2010BAMS3001.1

Saha, S., Moorthi, S., Wu, X., Wang, J., Nadiga, S., Tripp, P., Behringer, D., Hou, Y.-T., Chuang, H., Iredell, M., Ek, M., Meng, J., Yang, R., Mendez, M.P., Dool, H. van den, Zhang, Q., Wang, W., Chen, M., Becker, E., 2014. The NCEP Climate Forecast System Version 2. https://doi.org/10.1175/JCLI-D-12-00823.1

SCS (Soil Conservation Service), 1972. National Engineering Handbook, Section 4: Hydrology, DC: Soil Conservation Service, US Department of Agriculture. The Service.

Seidov, D., Haupt, B.J., 2005. How to run a minimalist's global ocean conveyor. Geophysical Research Letters 32. https://doi.org/10.1029/2005GL022559

Sen, P.K., 1968. Estimates of the Regression Coefficient Based on Kendall's Tau. Journal of the American Statistical Association 63, 1379–1389. https://doi.org/10.1080/01621459.1968.10480934
Shi, M., Shiraiwa, T., 2023. Estimating future streamflow under climate and land use change conditions in northeastern Hokkaido, Japan. Journal of Hydrology: Regional Studies 50, 101555. https://doi.org/10.1016/j.ejrh.2023.101555
Shi, M., Shiraiwa, T., Mitsudera, H., Muravyev, Y., 2021. Estimation of freshwater discharge from the Kamchatka Peninsula to its surrounding oceans. Journal of Hydrology: Regional Studies 36, 100836. https://doi.org/10.1016/j.ejrh.2021.100836
Sloan, P., Moore, I., Coltharp, G., Eigel, J., 1983. Modeling Surface and Subsurface Stormflow on Steeply-Sloping Forested Watersheds. KWRRI Research Reports. https://doi.org/10.13023/kwrri.rr.142
Stabeno, P.J., Reed, R.K., 1991. Recent lagrangian measurements along the Alaskan stream. Deep Sea Research Part A. Oceanographic Research Papers 38, 289–296. https://doi.org/10.1016/0198-0149(91)90069-R
Syed, T.H., Famiglietti, J.S., Chambers, D.P., Willis, J.K., Hilburn, K., 2010. Satellite-based global-ocean mass balance estimates of interannual variability and emerging trends in continental freshwater discharge. Proceedings of the National Academy of Sciences 107, 17916–17921. https://doi.org/10.1073/pnas.1003292107
Todini, E., 2007. Hydrological catchment modelling: past, present and future. Hydrology and Earth System Sciences 11, 468–482. https://doi.org/10.5194/hess-11-468-2007
Trenberth, K.E., Smith, L., Qian, T., Dai, A., Fasullo, J., 2007. Estimates of the Global Water Budget and Its Annual Cycle Using Observational and Model Data. Journal of Hydrometeorology 8, 758–769. https://doi.org/10.1175/JHM600.1
Uehara, H., Kruts, A.A., Mitsudera, H., Nakamura, T., Volkov, Y.N., Wakatsuchi, M., 2014. Remotely propagating salinity anomaly varies the source of North Pacific ventilation. Progress in Oceanography, Biogeochemical and physical processes in the Sea of Okhotsk and the linkages to the Pacific Ocean 126, 80–97. https://doi.org/10.1016/j.pocean.2014.04.016
Ujiié, Y., Asahi, H., Sagawa, T., Bassinot, F., 2016. Evolution of the North Pacific Subtropical Gyre during the past 190 kyr through the interaction of the Kuroshio Current with the surface and intermediate waters. Paleoceanography 31, 1498–1513. https://doi.org/10.1002/2015PA002914
Vallis, G., 2003. Mean and Eddy Dynamics of the Main Thermocline. https://doi.org/10.1007/978-94-010-0074-1_10
Walczak, M.H., Mix, A.C., Cowan, E.A., Fallon, S., Fifield, L.K., Alder, J.R., Du, J., Haley, B., Hobern, T., Padman, J., Praetorius, S.K., Schmittner, A., Stoner, J.S., Zellers, S.D., 2020. Phasing of millennial-scale climate variability in the Pacific and Atlantic Oceans. Science 370, 716–720. https://doi.org/10.1126/science.aba7096
Wang, J., Jin, M., Musgrave, D.L., Ikeda, M., 2004. A hydrological digital elevation model for freshwater discharge into the Gulf of Alaska. Journal of Geophysical Research: Oceans 109. https://doi.org/10.1029/2002JC001430

Watanabe, M., Dufresne, J.-L., Kosaka, Y., Mauritsen, T., Tatebe, H., 2021. Enhanced warming constrained by past trends in equatorial Pacific sea surface temperature gradient. Nat. Clim. Chang. 11, 33–37. https://doi.org/10.1038/s41558-020-00933-3
Weingartner, T.J., Danielson, S.L., Royer, T.C., 2005. Freshwater variability and predictability in the Alaska Coastal Current. Deep Sea Research Part II: Topical Studies in Oceanography, U.S. GLOBEC Biological and Physical Studies of Plankton, Fish and Higher Trophic Level Production, Distribution, and Variability in the Northeast Pacific 52, 169–191. https://doi.org/10.1016/j.dsr2.2004.09.030
Wendler, G., Galloway, K., Stuefer, M., 2016. On the climate and climate change of Sitka, Southeast Alaska. Theor Appl Climatol 126, 27–34. https://doi.org/10.1007/s00704-015-1542-7
Wetz, M.S., Hutchinson, E.A., Lunetta, R.S., Paerl, H.W., Christopher Taylor, J., 2011. Severe droughts reduce estuarine primary productivity with cascading effects on higher trophic levels. Limnology and Oceanography 56, 627–638. https://doi.org/10.4319/lo.2011.56.2.0627
Whitney, F.A., Bograd, S.J., Ono, T., 2013. Nutrient enrichment of the subarctic Pacific Ocean pycnocline. Geophysical Research Letters 40, 2200–2205. https://doi.org/10.1002/grl.50439
Winkler, K., Fuchs, R., Rounsevell, M., Herold, M., 2021. Global land use changes are four times greater than previously estimated. Nat Commun 12, 2501. https://doi.org/10.1038/s41467-021-22702-2
Xin, P., Shi, M., Mitsudera, H., Shiraiwa, T., 2024. Estimation of Freshwater Discharge from the Gulf of Alaska Drainage Basins. Water 16. https://doi.org/10.3390/w16182690
Xu, K., Huang, R.X., Wang, W., Zhu, C., Lu, R., 2017. Thermocline Fluctuations in the Equatorial Pacific Related to the Two Types of El Niño Events. J. Climate 30, 6611–6627. https://doi.org/10.1175/JCLI-D-16-0291.1
Yang, H., Wang, F., 2009. Revisiting the Thermocline Depth in the Equatorial Pacific. https://doi.org/10.1175/2009JCLI2836.1
Zaimes, G., Nichols, M., Green, D., Crimmins, M., 2007. Understanding Arizona's Riparian Areas.
Zhang, L., Wu, L., 2012. Can Oceanic Freshwater Flux Amplify Global Warming? https://doi.org/10.1175/JCLI-D-11-00172.1
Zhang, Y., Zheng, X., Kong, D., Yan, H., Liu, Z., 2021. Enhanced North Pacific subtropical gyre circulation during the late Holocene. Nat Commun 12, 5957. https://doi.org/10.1038/s41467-021-26218-7

Acknowledgement

I would like to express my deepest gratitude to my supervisor, Prof. Humio Mitsudera, for his invaluable guidance, unwavering support, and continuous encouragement throughout my time at Hokkaido University. His profound expertise, dedication to academia, and kind patience have been instrumental in fostering my passion for research.

I am sincerely grateful to Dr. Shi Muqing, who provided me with invaluable advice and assistance extended beyond hydrological modeling to include practical insights and experiences in research. I express sincere thanks to Prof. Takayuki Shiraiwa, for his expertise and guidance in hydrology and glaciology. I am also grateful to Dr. Takuro Matsuta, for his critical support with oceanic modeling and his insightful knowledge of oceanography. I would also like to thank Dr. Yuan Nan for her helpful assistance in oceanographic studies, as well as Dr. Wang Yefan for his kind support and invaluable experiences in research. I extend my appreciation to all the members of the Pan-Okhotsk group at the Institute of Low Temperature Science, Hokkaido University, for their supportive environment that made my time there enjoyable and productive.

I am deeply thankful to my family for their unwavering belief in me and their constant encouragement, which sustained me through the challenges of my academic life. I would also like to thank my friends for their encouragement and companionship, which made me feel that I was never alone.

Finally, this work was supported by Grants-in-Aid for Scientific Research, the Japan Society for the Promotion of Science (JSPS KAKENHI), No.21H01154, and the Japan Science and Technology Agency Support for Pioneering Research Initiated by the Next Generation (JST SPRING), Grant Number JPMJSP 2119.